Characterizing Deep Convective Cloud Properties and their Energetic Impacts in
Satellite Observations

By

Juliet A. PILEWSKIE

A dissertation submitted in partial fulfillment of
the requirements for the degree of

Doctor of Philosophy
(Atmospheric and Oceanic Sciences)

at the
UNIVERSITY OF WISCONSIN-MADISON
2023

Date of Final Oral Examination: 11/06/2023

The dissertation is approved by the following members of the Final Oral Committee:
  Tristan L'Ecuyer, Professor, Atmospheric and Oceanic Sciences
  Stephanie Henderson, Assistant Professor, Atmospheric and Oceanic Sciences
  Angela Rowe, Assistant Professor, Atmospheric and Oceanic Sciences
  Andrew Heidinger, Adjunct Associate Professor, NOAA
  Samuel Stechmann, Professor, Mathematics

Abstract

Characterizing Deep Convective Cloud Properties and their Energetic Impacts in Satellite Observations

by Juliet A. PILEWSKIE

Because atmospheric deep convection plays an important role in influencing Earth's global energy budget, it is increasingly important to consider how deep convective cloud and energetic properties might change due to a changing climate. Deep convective vertical intensity may increase in regions that are becoming increasingly moist in response to warming sea surface temperatures, which could alter precipitation, anvil cloud development, and their radiative response. The focus of this work, therefore, is to document the relationships between these properties applied to our present-day understanding of how convection fundamentally contributes to the Earth's energy budget: by 1) vertically transporting energy and mass to the upper troposphere, 2) balancing clear-sky radiative cooling through latent heating, and 3) modulating the top-of-atmospheric radiative energy budget.

The processes influencing how convective updraft strength relates to cloud and precipitation development occur on the convective cloud scale and smaller, so it is necessary to document such characteristics on these scales. We begin by providing a near-global perspective of convection using a database of "convective objects" generated from ten years of A-Train measurements. By leveraging CloudSat's ability to distinguish convective cores, we define a proxy for a convective core vertical intensity based on the height

of the attenuating radar signal. Over the tropics, these observations support previous insights from a precipitation perspective on where storms are the most intense. Motivated by wanting to understand deep convective contributions to lateral energy transport, we next document how the intensity and frequency of deep convective cores that reach the tropopause (hot towers) relate to anvil cloud and precipitation productivity within the tropics. It is found that the largest amount of mass within the upper troposphere supplied by hot towers is not geographically where the most precipitation and largest anvil extents occur. Motivated by convection's influence on the top-of-atmospheric radiative energy budget, we analyze how convective core depth and anvil structure influence their cloud radiative effects. We find that the most vertically intense systems more often contribute a warming at the top of the atmosphere compared to weaker systems, which holds across different regions in the tropics. Finally, we explore how these relationships are sensitive to large-scale environmental conditions to provide benchmark relationships for modeling studies assessing high cloud feedbacks in a changing climate.

"Think left and think right and think low and think high. Oh, the thinks you can think up if only you try!"

Dr. Seuss

Acknowledgements

I have heard from a few people now that the key to "success" within a profession is to surround yourself with good people. I did not realize just how important this sentiment was until I personally experienced it throughout this PhD journey. From my mentors, to new collaborators, to my family and friends; I am endlessly grateful to have had such immense support. Before I continue personally thanking those in my life, I want to acknowledge that this research has been supported by the NASA Science Mission Directorate through the Future Investigators in NASA Earth and Space Science and Technology program (Award no. 80NSSC20K1651) and the NASA Jet Propulsion Laboratory (CloudSat Grant no. G-39690-1).

I would like to acknowledge my advisor, Tristan L'Ecuyer, for his mentorship. He always presented himself with support, positivity, and patience, which spurred my excitement to do research after each meeting. His positivity was equally met with a willingness to challenge me to think critically and independently. In part because of his mentorship style, I have become quite an independent, yet confident researcher who maintains a healthy level of skepticism. Through Tristan's collaborative efforts, I had the incredible opportunity to conduct research and attend a workshop in France last summer, for which I am endlessly grateful.

I would like to thank my PhD committee members: Angela Rowe, Stephanie Henderson, Andy Heidinger, and Sam Steckmann. They offered clear guidance at each meeting and helped me focus my research questions. I particularly want to thank Angela Rowe and her graduate student, Ben Rodenkirch, with whom I have begun collaborating. It has been an exciting process learning about this topic from a field campaign point of view, and I am excited to continue learning from the Rowe group. I also want to thank Larissa Back and Ángel Adames-Corraliza who have both been pivotal in helping deepen my understanding in tropical meteorology. I would like to acknowledge both Jon Martin and Ankur Desai who have acted as mentors over the years. Each professor has always led

with passion for the science as well as a willingness to listen and offer sage advice when I needed it most. I would like to thank Dave Henderson who has also given me advice and scientific recommendations. If it weren't for him recommending that I study storms on the cloud object scale, I do not know where I would have gone with my dissertation.

Next, I would like to thank all of my collaborators. Hanii Takahashi, who has been so encouraging from the beginning, and who gave me thorough notes for each slide of my dissertation defense presentation. I am very excited to be co-organizing a workshop with her. Graeme Stephens, who provided me with the idea and project of revisiting an old study exploring *hot towers*. He believes in my potential, which has instilled me with confidence (unbeknownst to him). I am forever grateful towards Dominique Bouniol who hosted my stay in Toulouse. Between running errands with me, to inviting me to dinner with her family, to sitting down and brainstorming project ideas well into the evening, I developed a deep professional and personal bond with her that I hope continues to develop. I would like to thank Pierre Kirstetter, Chloé Radice, Thomas Fiolleau, Hélène Brogniez, and Johnny Luo who were collaborators at the atmospheric water cycle workshop in Paris. It was through them and this experience where I truly tapped into my scientific identity and potential. I would also like to extend my thanks to Kyle Obremski, Anita Rapp, Savannah Elkins, Bowen Pan, Aryeh Drager, and Sue van den Heever who have also been great to work with.

I would like to thank the AOS staff: Pete Pokrandt, Christi Balas Levenson, Carolyn Lipke, Dee VanRuyven. I am grateful for all of Pete's help with solving past computer issues and inquiries, particularly during Covid when we were having to work virtually. Christi, Carolyn, and Dee have been so helpful with literally guiding my PhD completion. Without their logistical knowledge, this process would have taken quite a deal longer. I also want to thank the AOS community broadly: specifically the L'Ecuyer group, as well as the graduate student body, and the department as a whole. It has been such a supportive environment that enables students to flourish.

On a more personal note, I have several friends to thank within the AOS department. Julia Shates, I am so lucky to have begun graduate school with you. We were like sisters going through the program constantly confiding in one another. I hope that it continues throughout our careers. Bailey Murphy, you always met a problem with a solution and challenged my perspective. You are a forever friend and confidant. Maria Madsen, you have a calming and supportive presence and are deeply empathetic. I am so grateful to have gravitated towards you. And I am deeply grateful for so many more friendships along the way: James Anheuser, Victor Mayta, Susi Wiesner, Zoë Brooke Zibton, Vijit Maithel, Miguel Bernardez, John Young, Tim Schmit, Sreenath Paleri, Andrew Dzambo, Anne Sledd, Elin McIlhattan, Poush Ghosh, and Cameron Bertossa. Each of you have impacted my PhD journey in such beautiful ways and am so excited to see where you all go. I would also like to extend my thanks to all of my friends in the broader Madison community and beyond. You have kept me grounded and helped me fulfill a life and identity outside of academics.

Lastly, I thank my family. To my supportive pops, I do not think there are quite the words to express how deeply grateful I am for you. You have supported and encouraged me at each life step, and I feel such love deeply. You have also challenged me and offered me advice over the years, and sometimes it was at times when I was not always open to it. Part of life is recognizing when advice is applicable, and I have often found that your messages do not resonate until well after you've said them. Not only did I actualize the "just get it done" mentality–which you mentioned to me several years ago–just this past year, it became my mantra as I finished my PhD. To my caring mother, who is always so positive and willing to lend an empathetic ear. You are wonderful at balancing my emotions and offering alternate perspectives when I begin worrying. And Monica, I am so proud to call you my sister. I see so many similarities between us, yet we are so different. Thank you for being the constant in my life, the lifeline that has no bounds or limits. My beautiful family is not complete without our goofy dog, Dave. I've appreciated your snuggles over the years.

Contents

List of Figures

List of Tables

Chapter 1

Introduction

Tropical atmospheric deep convection has been studied extensively because it is integral to the Earth's global energy budget, helps drive local and large-scale atmospheric circulations, and also supplies significant amount of rainfall in the tropics that is necessary for sustaining human life. However, as atmospheric CO_2 concentrations are increasing due to human activity, extreme weather is becoming more apparent across the globe, as discussed in the Intergovernmental Panel Climate Change (IPCC) Sixth Assessment (AR6) Synthesis Report (IPCC, 2023). Figure 1.1 shows that some regions across the globe are already experiencing heat extremes and droughts (i.e. a *lack of* storm activity), while others are experiencing heavier precipitation in response to climate change. The changing climate has a direct effect on food and water security, and other such public health and economic impacts. Because of heat extremes and weather hazards, such as the likelihood that major (Cat 3-5) tropical cyclone activity is increasing, peoples' lives are

increasingly at stake (IPCC, 2023). Climate model projections are showing that convective system behavior is expected to continue to alter in response to surface warming (e.g. Cheng et al., 2022; Diffenbaugh et al., 2013; Singh and O'Gorman, 2015). It is, therefore, worth understanding present-day convective cloud, precipitation, and radiative response characteristics to inform how convection contributes to the Earth's energy budget and its interactions with the surrounding environment.

Physics states that convection occurs where there exists an imbalance in energy within a fluid, whereby energy is transferred from an area in an energy surplus to an area in an energy deficit. In meteorological terms, atmospheric convection occurs when there is a difference in temperature gradients, or lapse rates, between air masses. For the sake of this dissertation, we will primarily be focused on convection within the tropics because of the role that tropical atmospheric deep convection has in influencing Earth's energy budget and large-scale circulations.

Observation- and model-based theories suggest that there are three primary ways in which tropical atmospheric deep convection contributes to the Earth's energy budget on the large-scale, through 1) vertically redistributing boundary layer, moisture-filled air to the upper troposphere (Riehl and Malkus, 1958; Riehl and Simpson, 1979), 2) balancing radiative cooling through precipitation that releases latent heat (Manabe and Wetherald, 1967), and 3) altering the radiative energy budget at all levels in the atmosphere according to fundamental radiative transfer processes (Manabe and Strickler, 1964; Manabe and Wetherald, 1967). The following describes each process in more detail:
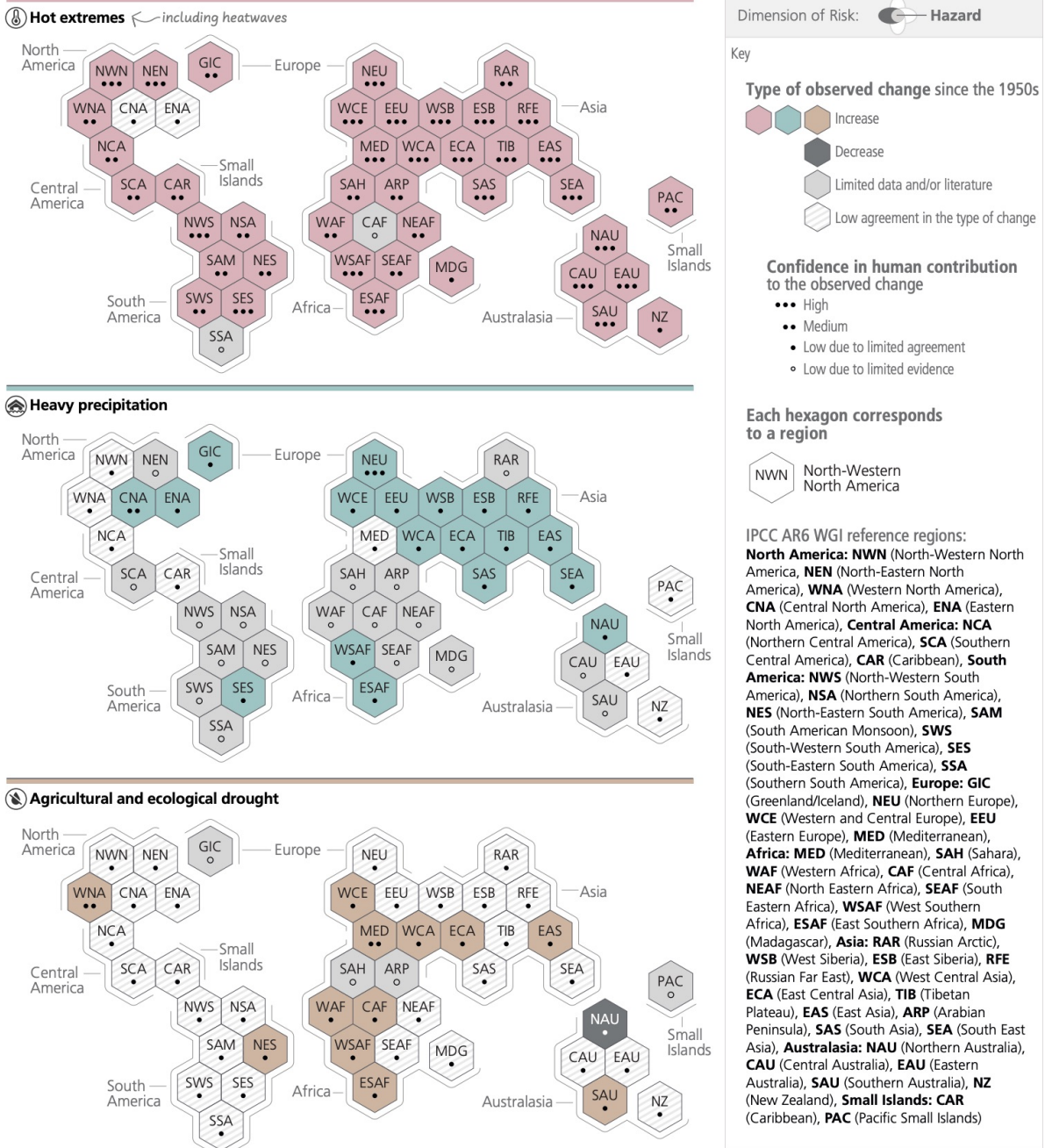
Figure 1.1: Courtesy of IPCC (2023)

1. Riehl and Malkus (1958) and Riehl and Simpson (1979) (hereafter, RM58 and RS79, respectively) argued that most of the energy within the ascending branch of the Hadley Cell positioned near the equator is in the form of latent energy released through condensation. They reasoned that a minimum in moist static energy (MSE) at 500 hPa is a signature of some mechanism that could allow for upper-tropospheric MSE to be the same value as surface MSE. It was concluded that individual updrafts transport boundary layer air to the upper troposphere that not only balances radiative cooling, but also supplies a surplus of energy to be transported to higher latitudes that are in an energy deficit. These updrafts became known as hot towers and are primarily responsible for converting latent energy to potential energy (a combination of dry static energy and enthalpy) through vertical transport. Through mass continuity, compensating downdrafts in between updraft regions complete the picture; thus, convective systems became understood to drive much of the energy and moisture redistribution within and out of the tropics (RM58; RM79).

2. In 1967, Manabe and Wetherald (1967) conducted simple modeling experiments and found that under radiative equilibrium (i.e. no convection present) with fixed relative humidity, the atmospheric temperature decreases rapidly to 240 K just above the surface due to Earth's thermal emission. However, under "radiative-convective equilibrium" (RCE), atmospheric temperature was found to decrease at a steadier rate as altitude increased. This is due to the latent heat release associated

with condensation. It was found that radiative-convective equilibrium holds globally as a first-order approximation.

3. Three years prior, Manabe and Strickler (1964) used a simple radiative-convective equilibrium model to show that high cirrus clouds heat the surface by an amount that corresponds to their height and emissivity. The same study that popularized RCE found that as cloud amount increases, Earth's equilibrium temperature decreases (Manabe and Wetherald, 1967). They concluded that clouds absorb Earth's outgoing infrared radiation. Because temperatures are colder at higher altitudes in the atmosphere, higher cloud tops emit at lower temperatures. This leads to a decrease in OLR as well as an enhanced LW radiation back down to the Earth's surface. However, they did not understand that albedo and emissivity are related, so they neglected to alter the albedo (i.e. its ability to reflect incoming solar or SW radiation) of the cloud as it increased in thickness (i.e. changing its emissivity). It was thus concluded that the thickest cirrus clouds contribute the most warming. However, Stephens and Webster (1981) showed that as the liquid water path (LWP) or ice water path (IWP) increased for high clouds, (i.e. increased optical depth) the change in equilibrium surface temperature decreased. It was therefore updated that thin cirrus clouds contribute the most warming and not thicker cirrus.

Both thermodynamic and radiative processes associated with convective cloud clusters' formation and evolution are sufficiently strong enough to alter vertical profiles of heating

within the atmosphere (Houze Jr., 1982). These processes can influence large-scale circulations in the tropics, and Houze Jr. (1982) further noted that the impacts vary over the lifetime of a convective system. As was mentioned previously, both radiation and surface fluxes from heat and water vapor can destabilize the atmosphere, which initiates moist convection that acts as a stabilizing mechanism. The initiation or cumulus stage is defined by a warm buoyant plume rising, mixing laterally with the environment, and forming a cloud that is optically thick and reflects some incoming SW radiation but is relatively small across spatial scales.

As it begins to rain, a downward drag force induced by rain drops instigates a vigorous downdraft circulation that is evident in the mature stage. The downdraft region is responsible for the heaviest rainfall within the system. As the top of the cloud reaches the level of neutral buoyancy which is sometimes at the tropopause, clouds spread into cirriform anvil in which stratiform precipitation often forms Houze (1997); Schumacher and Houze (2003). At this stage there is significant cloud cover in both the horizontal and vertical direction. Updrafts can be continuously generated and decease throughout the duration of the system; however, the anvil from prior updrafts is maintained for much longer than the lifetime of a single updraft. The differences in lifecycles between updrafts and anvils make it challenging to quantify the anvil productivity of any given deep convective core. Furthermore, entrainment, or mixing with the surrounding atmosphere, impacts anvil development. During the dissipating stage, cloud droplets no longer grow, so precipitation stops. Vertical air motions also weaken and die, while the upper level clouds remain emitting and absorbing radiation. Upper clouds thin out and break up, which reduces

the SW cloud forcing and enhances LW forcing (Houze Jr., 1982). The decay stage is often sustained on longer timescales than the duration of the active convective system.

Deep convective systems within the atmosphere span anywhere from 10 km, such as isolated updrafts, to thousands of kilometers, such as Mesoscale Convective Complexes (MCCs) that contain multiple Mesoscale Convective Systems (MCSs), each of which having active updraft precipitating regions (e.g. Maddox, 1980; Mapes and Houze, 1993; Yuan and Houze, 2010). On the time scale of a convective system, which is anywhere from hours to multiple days, diabatic effects from precipitation and cloud radiative heating contribute to maintaining or weakening convection. These energetic impacts not only influence how convection spatially organizes, or aggregates, but are also responsible for generating eddies that transfer energy and moisture, thus inducing circulations and heating the local surroundings.

How an ensemble of convective systems spatially organize and how long they are maintained is most important when considering climate impacts. Throughout their lifecycle, convective systems alter the spatiotemporal patterns of radiative heating and cooling at the top-of-atmosphere, which impacts the large-scale atmospheric circulation (Randall et al., 1989; Slingo and Slingo, 1988, 1991). Altogether, it is generally accepted that deep convective clouds contribute a near-neutral top-of-atmosphere radiative effect due to their ability to both significantly reduce outgoing thermal radiation while reflecting incoming shortwave radiative fluxes (Hartmann et al., 1992; Kiehl and Ramanathan, 1990; Ockert-Bell and Hartmann, 1992; Rossow and Zhang, 1995; Zhang et al., 1995). It is

also possible that convective systems' near-neutral impact is a result of integrating their radiative effects over the course of their lifetimes Hartmann and Berry (2017).

However, as the climate changes, changes in large-scale circulation are expected to alter convective cloud formation and their radiative responses, thus generating a feedback (Bony et al., 2015; Li et al., 2014; Sherwood et al., 2014). Climate models make predictions of climate warming by measuring the "equilibrium climate sensitivity" (ECS), which is the equilibrium change in the globally averaged near-surface temperature in response to a doubling of the concentration of atmospheric CO_2. According to the IPCC AR6, the climate sensitivity is in the *likely* range of 2.5 K to 4.0 K, but *very likely* between 2.0 K and 5.0 K (Forster et al., 2021). Climate warming is expected to influence the distribution of precipitation changes, with the wettest latitudes getting enhanced precipitation while driest latitudes may get a decrease in precipitation (Allen and Ingram, 2002; Held and Soden, 2006; Mitchell, 1987). Additionally, atmospheric general circulation models (GCMs) are showing that precipitation extremes become more frequent with enhanced atmospheric CO_2 concentrations (Gordon et al., 1992).

Following work summarized in the IPCC Fifth Assessment Report (AR5), observations had suggested that the climate sensitivity was near the lower end of the 3 K temperature range and that models might have also been underestimating precipitation changes (Mauritsen and Stevens, 2015). These discrepancies had pointed to the possibility that climate models were missing key feedbacks and that the processes that drive cloud-circulation interactions were poorly represented (Bony et al., 2015; Dessler, 2013; Mauritsen and

Table 7.9 | Assessed sign and confidence level of cloud feedbacks in different regimes in AR5 and AR6. For some cloud regimes, the feedback was not assessed in AR5, indicated by N/A.

Feedback	AR5	AR6
High-cloud altitude feedback	Positive (*high confidence*)	Positive (*high confidence*)
Tropical high-cloud amount feedback	N/A	Negative (*low confidence*)
Subtropical marine low-cloud feedback	N/A (*low confidence*)	Positive (*high confidence*)
Land cloud feedback	N/A	Positive (*low confidence*)
Mid-latitude cloud amount feedback	Positive (*medium confidence*)	Positive (*medium confidence*)
Extratropical cloud optical depth feedback	N/A	Small negative (*medium confidence*)
Arctic cloud feedback	Small positive (*very low confidence*)	Small positive (*low confidence*)
Net cloud feedback	Positive (*medium confidence*)	Positive (*high confidence*)

FIGURE 1.2: Courtesy of Forster et al. (2021)

Stevens, 2015). A major source of uncertainty contributing to the large spread was how convective and boundary-layer processes are represented in climate models (Bony et al., 2015). Additionally, cloud microphysical processes make it difficult to simulate convective response to varying large-scale dynamics. Since the IPCC AR5, there has been improvements on how cloud feedbacks are quantified, in part by calculating cloud feedbacks by region to capture unique interactions between clouds and the environment within each region, weighting the feedback by the fractional coverage of each cloud type, and finally summing to give the global feedback (Sherwood et al., 2020).

It has long been discussed how anvil clouds might alter in response to a warming climate. Ramanathan and Collins (1991) used observations during the 1987 El Niño and proposed the "Thermostat Hypothesis" that argued that enhanced sea surface temperatures could increase cirrus cloud formation to reflect enough solar radiation to offset LW cloud radiative forcing and prevent sea surface temperatures from rising above 305 K (Ramanathan and Collins, 1991). Alternatively, Lindzen et al. (2001) proposed that the Earth's atmosphere can act as an adaptive infrared iris (i.e., the "adaptive iris effect"), which opens

and closes, like that of an eye, in order to control outgoing longwave radiation. The adaptive iris effect was supported by suggesting that cirrus detrainment from cumulus convection might decrease with increasing SSTs if the precipitation efficiency, defined as the fraction of cloud condensate that reaches the surface as precipitation (Narsey et al., 2019), within cumulus towers increases significantly with increasing SSTs (Lindzen et al., 2001).

More recently, it has been suggested through studying cloud-resolving model output that the atmosphere will increasingly stabilize with surface warming, which could reduce the anvil cloud amount (Bony et al., 2016). This hypothesis is an update to the "adaptive iris" effect and is known as the "stability iris" effect. Despite the update, there still exists low confidence in what is known as the tropical high cloud amount feedback (see Figure 1.2), meaning that it is not well captured in models how the amount of convective cloud might vary in response to changes in the large-scale dynamic and thermodynamic environment with climate (Forster et al., 2021). This in part could be attributed to not adequately capturing whether it is the cloud extent, cloud optical depth (i.e. thickness), or both extent and thickness that are changing with climate. These discrepancies are important to discern as these cloud changes directly influence the top-of-atmosphere cloud radiative response.

Therefore, understanding how deep convective clouds and their resulting energetic responses behave in the present-day climate is crucial to provide benchmarks for diagnosing high cloud changes in a warming climate. Leveraging the extensive sampling provided

by A-Train and geostationary satellite platforms, this work examines the relationships between deep convective cloud vertical and horizontal properties, precipitation, and radiative impacts. Chapter 2 introduces an object-identification algorithm to produce a database of "convective objects" from multiple sensors within the A-Train. A brief history and overview of how object identification works is provided. How convective cores are identified and how their vertical intensity is characterized using satellite radar is also addressed. Additionally, we provide a list of the stored variables that relate to convective systems' energetic contributions.

Chapters 3 through 5 discuss three separate analysis that have been supported by the Future Investigators in NASA Earth and Space Science and Technology (FINESST) graduate student research award. The three specific aims that we had outlined in the FINESST project proposal were:

1. **Documenting Global Characteristics of Convective Organization**: Contribute a multi-year global convective object database of variables that documents convective macroscopic characteristics, associated environmental conditions, precipitation rates, and radiative effects.

2. **Precipitation and Radiative Impacts of Convection**: Quantify the coupled hydrologic and energetic impacts of convection based on its macro-characteristics in varying environments.

3. **Supplying Life-cycle Context to Observed Convection**: Assess how convective characteristics, their energetic impacts, and their role in the local and large-scale environment evolve over the convective life-cycle.

Chapter 3 addresses the first aim by providing a global perspective of atmospheric convection through A-Train observations. Specifically, we discuss the frequency of convection at 0130 and 1330 local solar time (LST), as well as where the most vertically intense systems occur, where there is the most rainfall, and where systems are the largest. The bulk of this work is motivated by the paper by Zipser et al. (2006) that uses Tropical Rainfall Measuring Mission (TRMM) Precipitation Radar (PR) observations to document where the most intense storms are located via precipitation proxies. This chapter has been published to the Journal of Geophysical Research: Atmospheres under the title *The Global Nature of Early-Afternoon and Late-Night Convection Through the Eyes of the A-Train.*

Chapter 4 also addresses the first aim of the FINESST propopsal. It is motivated by the Riehl and Malkus (1958) and Riehl and Simpson (1979) Hot Tower Hypothesis to provide an update on how many hot towers, or deep convective cores that overshoot the tropopause, occur at any given time. It leverages the A-Train's ability to capture deep convective cores at nearly a 1 km resolution over the full tropics. In addition to the A-Train convective object database cloud properties, 11 micron infrared brightness temperatures from geostationary satellite observations, rain rates from Integrated Multi-satellitE Retrievals for GPM (IMERG), and top-of-atmosphere longwave radiative fluxes from the Clouds and the Earth's Radiant Energy System (CERES) instruments, provide a

multi-satellite perspective to estimate the frequency and mass flux of convective cores, and how they relate to precipitation and high cloud productivity. Capturing these properties is particularly important because they relate to the transport of energy and moisture within and outside of the tropics. This analysis is the focus of a paper to be submitted to Survey of Geophysics by the beginning of November 2023 and is titled *A multi-satellite perspective on "hot tower" characteristics in the equatorial trough zone.*

The focus of Chapter 5 is to address the FINESST proposal's second aim by analyzing how the deep convective core intensity and cloud thickness vary with one another, and assessing the LW, SW, and net cloud radiative responses at the top of the atmosphere. For this work, A-Train-observed convective objects between 2006-2016 over the tropical ocean are distinguished and characterized based on whether they are unicellular or multi-cellular to provide an idea for how cloud properties and their radiative responses differ on multiple scales, which are signatures of physical processes that behave on different scales. We also document how cloud properties and their radiative effects vary between populations of convective systems sorted by their vertical intensity to provide a bench-mark that could be useful for modeling studies assessing cloud and radiative responses of convective systems. This paper, titled *Observational Evidence towards a Weakened Cooling Top-of-Atmosphere Net Cloud Radiative Effect Associated with the Most Intense Convective Systems*, is in its final stages of the internal review process and will likely be submitted for publication in December 2023. Documenting how these relationship vary in differing large-scale environments is ongoing and will be submitted as a follow-on

paper. A subsection explaining this preliminary work is provided under *Future Projects* in Chapter 6.

We conclude in Chapter 6 with a synthesis of the three chapters as well as preliminary analyses that are currently underway. The precipitation part of the second aim and the third aim from the FINESST proposal are not fully addressed in the main analysis chapters. However, preliminary work has been done on these topics and are the subjects of subsections under *Future Projects*.

Chapter 2

An A-Train Convective Object Database

2.1 Preface

Identifying contiguous cloud objects in satellite observations has been an effective tool when using active remote sensing data (e.g. Bacmeister and Stephens, 2011; Igel et al., 2014; Sauter et al., 2019; Xu et al., 2019, 2016, 2005). Cloud objects are a contiguous region of pixels that satisfy a cloudiness threshold, such as a minimum reflectivity value in the case of satellite radar-based cloud objects (Bacmeister and Stephens, 2011; Igel

---

[1]Material in this chapter is an updated version of the Data and Methods section in: Pilewskie, J. A., & L'Ecuyer, T. S. (2022). The global nature of early-afternoon and late-night convection through the eyes of the A-Train. *Journal of Geophysical Research: Atmospheres*, 127, e2022JD036438.

et al., 2014). Examples of their utility include understanding how different environments influence convective cloud characteristics, and how these characteristics evolve over the cloud lifetime in order to connect observations to model-based theories of aggregation (e.g. Igel et al., 2014; Igel and van den Heever, 2015a; Xu et al., 2019, 2016, 2005). Active sensors, such as those on TRMM, GPM, CloudSat, and CALIPSO, offer added benefit for identifying cloud objects and quantifying storm intensity by assigning vertical structure to each cloud object (Bacmeister and Stephens, 2011; Nesbitt et al., 2000; Zipser et al., 2006). The vertical characteristics of cloud objects can be matched with other features, such as cloud top heights and anvil width, to create a three-dimensional description of the cloud object (e.g. Deng et al., 2016; Igel et al., 2014) at various life stages (Hu et al., 2021). Such measurements supply information on the vertical distribution of liquid and ice particles to distinguish updraft regions, precipitating and non-precipitating anvil, and detrained cirrus.

We employ a new convective cloud-object identification approach based on the combination of measurements from several instruments in the A-Train to create a global database of COs. Variables that relate to updraft intensity, cloud top height, horizontal extent of anvil regions, precipitation yield, radiative effects, and associated environmental conditions are calculated from co-located observations and included in the database. Outlined below are the data sets used as well as the methods for identifying convective objects.

2.2   A-Train Instruments

Convective objects are identified based on high-resolution vertical profiles of radar reflectivity supplied by CloudSat's 94 GHz Cloud Profiling Radar (CPR). From 2006-2018, CloudSat orbited at 705 km as part of the A-Train constellation, which travels in a sun-synchronous orbit passing the equator at approximately 1:30 am (nighttime) and 1:30 pm (daytime) local time (LT) (L'Ecuyer and Jiang, 2010; Stephens et al., 2002, 2008). The CPR is the first spaceborne millimeter wavelength radar and captures finer scale cloud features and convective storm properties than has previously been possible (Stephens et al., 2008). It is a nadir-looking radar measuring the power backscattered by cloud and precipitation droplets as a function of distance from the radar. CPR has an antenna size of 1.85 m and a pulse width of 3.3 μs, resulting in a 1.4 km cross-track resolution and a vertical resolution of 480 m that is over-sampled to 240 m. The integration time along the nadir track is 0.16 s, which provides a 1.8 km along track resolution. CPR outputs vertical structures of reflectivities with a minimal detection of about -30 dBZ, a dynamic range of 70 dB and calibration accuracy of 1.5 dB (Stephens et al., 2002; Tanelli et al., 2008). CloudSat data is stored in granules that can be obtained from the CloudSat Data Processing Center. One granule represents measurements retrieved between two successive nighttime equatorial crossings. Using backscattering from cloud droplet particles to deduce where clouds exist, the 2B-GEOPROF CloudSat product supplies cloud masks and radar reflectivities (Marchand et al., 2008).

The Cloud-Aerosol Lidar and Infrared Pathfinder Satellite Observation, or CALIPSO,

provides insight into the role that clouds and atmospheric aerosols play in regulating Earth's weather, climate, and air quality. The active sensor on board CALIPSO is the Cloud-Aerosol Lidar with Orthogonal Polarization, or CALIOP, which is a two-wavelength polarization-sensitive lidar measuring backscatter. Combining measurements from CALIOP with information from passive infrared and visible imagers (Imaging Infrared Radiometer, IIR and Wide Field Camera, WFC) allows high resolution vertical structure and properties of thin clouds and aerosols to be derived. The 2B-CLDCLASS-LIDAR product combines CloudSat and CALIPSO measurements to capture complete profiles of convective clouds, including thin cirrus clouds that CloudSat alone cannot detect (Sassen et al., 2008). Estimates of the radiative effects of convective systems are calculated for each CO from estimates of broadband fluxes stored in the 2B-FLXHR-lidar data product described in detail in Henderson et al. (2013). These estimates are derived using retrieved cloud properties from CloudSat, CALIPSO, and the Moderate Resolution Imaging Spectroradiometer (MODIS) in a broadband radiative transfer model (Henderson et al., 2013; L'Ecuyer et al., 2008). Root-mean-square differences in monthly-mean 2.5-degree SW and LW fluxes are 13.8 W m^{-2} and 5.9 W m^{-2} relative to CERES, respectively (Matus and L'Ecuyer, 2017).

The Advanced Microwave Scanning Radiometer, or AMSR-E, is a twelve-channel, six-frequency, passive microwave radiometer on board Aqua—the lead satellite in the A-Train constellation. AMSR-E measures brightness temperatures, and vertically and horizontally polarized measurements are acquired at all channels. Its spatial resolution varies from 5.4 km at 89.0 GHz to 56 km at 6.9 GHz, with a 1445 km swath and sampling interval

of 10 km for 5-36 GHz and 5 km for 89 GHz. AMSR-E measurements are used to retrieve precipitation rate, cloud water, water vapor, sea surface temperature and winds, and a variety of cryosphere-related variables (e.g. Kummerow et al., 2001; Markus and Cavalieri, 2000). Rainfall rate uncertainties depend on numerous factors including the environment and the Bayesian retrieval framework itself but range from 40-80% in most cases (Berg et al., 2006; L'Ecuyer and Stephens, 2002). AMSR-E finished operations in December 2011. Launched in May 2012, the Japan Aerospace Exploration Agency (JAXA) Global Change Observation Mission 1st - Water "SHIZUKU" (GCOM-W1) satellite carries AMSR2, which is the follow-on to AMSR-E. AMSR2 orbital specs and measurements remain consistent with that of AMSR-E, but each channel has a slightly higher spatial resolution. AMSR-E/AMSR2 Unified L2B Global Swath Ocean Produces and Global Swath Surface Precipitation data products are maintained at their native resolution of 5.4 km and are oversampled to match the CloudSat field of view to produce AMSRE-AUX and AMSR2-AUX data sets (Burzynski and Partain, 2022; Kummerow et al., 2021a,b, 2020).

2.3 Identifying Convection

While the presence of liquid precipitation leads to substantial attenuation of CloudSat reflectivity profiles that limits rainfall intensity retrievals (Battaglia et al., 2008), the path-integrated attenuation (PIA) provides a powerful signal for discriminating rainfall and drizzle from non-precipitating clouds (Haynes et al., 2009). Furthermore, the height at which reflectivity decays towards the surface through attenuation establishes a unique

method for identifying convective cores in CloudSat observations. This is the premise behind the convective core detection in CloudSat's 2C-PRECIP-COLUMN algorithm (hereafter, 2CPC).

2CPC identifies precipitation using a combination of PIA derived from the strength of the observed surface return and multiple scattering-corrected reflectivities (Haynes et al., 2009). It infers convection by searching for attenuation decay in the ice-phase region above the melting layer. The method, illustrated in Figure 2.1b, is a W-band analogue to identifying bright band signatures in conventional precipitation radar observations (e.g. Steiner et al., 1995). In this case, however, the feature of interest is the inflection point in the reflectivity profile caused by attenuation from significant quantities of liquid or partially-frozen raindrops, super-cooled liquid cloud droplets, or large, heavily rimed ice particles (see Figure 2.1b). For simplicity, the level where this signal occurs in each CloudSat profile is labeled the 'rain top height' (RTH) in 2CPC since it is not possible to distinguish the precise source of the strong attenuation observed below it. This level forms the basis for identifying the presence of convective updrafts at the 1.4×1.8 km CPR resolution. Since strong updrafts loft liquid, partially-melted hydrometeors, graupel, and hail above the freezing level, we define a convective profile (blue curve) as one in which the estimated RTH exceeds the freezing level by at least two CloudSat vertical range bins, or 480 m. Such profiles are generally associated with large along-track reflectivity gradients at altitudes just above the freezing level. Stratiform precipitation is characterized by RTH near or slightly below the freezing level (green curve) and often exhibits a brightband-like feature, although this feature is due to attenuation as opposed to enhanced reflectivity

from large melting ice particles (Sassen et al., 2007). Raining pixels with cloud and RTH below the freezing level constitute warm rain.

CloudSat's precipitating profile classification qualitatively agrees with brightband and convective features in Ku-band reflectivity profiles. Figure 2.1a shows cross-sections from nearly coincident observations of a convective rain system from CloudSat CPR and TRMM PR. The cross-sections directly contrast perspectives from these two satellite radars at their native resolutions. A convective core is evident on the left side of the PR cross-section where reflectivities of 40 dBZ are observed at heights of up to 10 km. The CPR presents RTHs between 8 and 12 km in several profiles, which suggests that the intensity of updrafts varies considerably across the convective region. On the right side of Figure 2.1a, both radars detect stratiform rain with the largest TRMM reflectivities at the melting layer and CloudSat predicting rain top heights at the freezing level. Between the two TRMM PR rain systems, the CPR detects lighter stratiform rain that may fall just below the 17 dBZ sensitivity of the PR but would likely be observed by the current GPM DPR.

We use the term 'convective core' to describe the elevated attenuation signature shown in Figure 2.1b and as the proxy for convective regions in COs. It is very likely that this signature derives from nearby updrafts, but no explicit vertical motion measurement is available to formally verify this. Nevertheless, this proxy has several unique strengths for the present study. Unlike infrared (IR) methods that are based entirely on cloud top signatures—whether static, such as identifying overshooting tops (e.g. Bedka et al., 2010),

or dynamic that involve computing changes in cloud top temperature (e.g. Fiolleau and Roca, 2013; Takahashi and Luo, 2014)—CloudSat observations penetrate into the cloud to observe the vertical structure of precipitating hydrometeors within it. Passive microwave methods are more sensitive to precipitating hydrometeors than IR but often link ice scattering signatures to the presence of convection over fields of view that are too large to resolve convective cores. The active CPR radar yields a more direct measurement of precipitation vertical structure than passive microwave methods because CPR can penetrate into the cloud to resolve the height where liquid water is likely present within the column, and it does so at two orders of magnitude finer spatial resolution (by area). While the most direct and complete measurements for identifying areas of strong convection from space derive from the Ku-band radar reflectivities collected by the TRMM and GPM missions, the Ku-band radar field of view is nearly 7 times larger than of CloudSat (18.5 km^2 vs. 2.7 km^2). Thus, while no satellite observing instrument is capable of perfectly isolating updraft regions on sub-kilometer scales (e.g. Giangrande et al., 2013; Wang et al., 2020; Yang et al., 2016), CloudSat does perform better than TRMM and GPM (Li and Schumacher, 2011). W-band also has the distinct advantage over Ku-band at detecting weak precipitation. CloudSat, therefore, offers some advantages over TRMM and GPM in terms of resolution and sensitivity to convective motions while sacrificing the ability to retrieve rainfall intensity near the surface. We work around this major limitation by coupling AMSR-E and AMSR2 rainfall estimates to CloudSat convective cores.
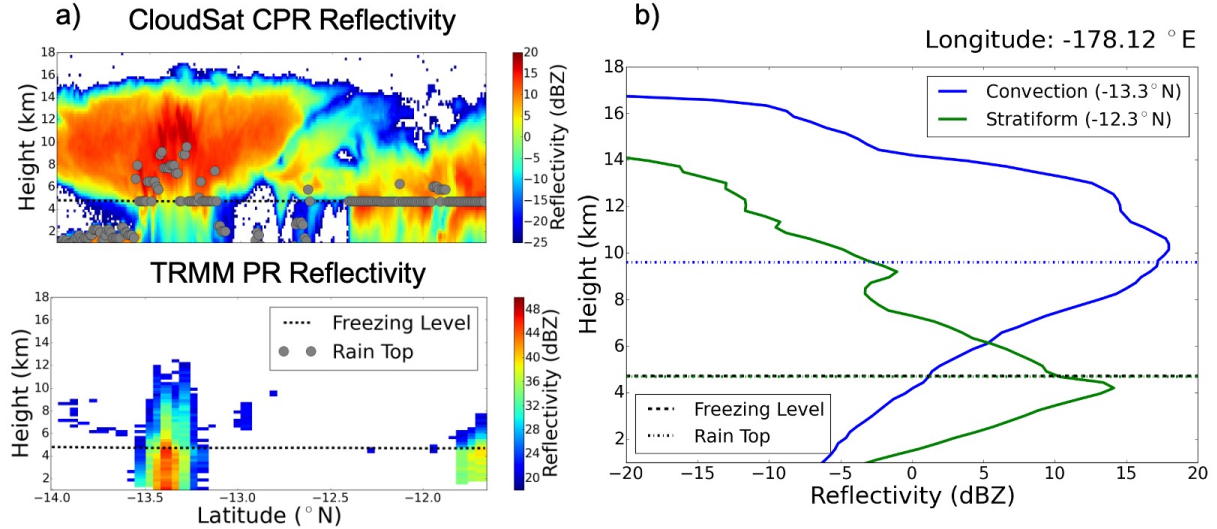
FIGURE 2.1: The distinct signatures of convective and stratiform rainfall in CloudSat observations. Left: Reflectivity profiles from a precipitation scene observed by both CloudSat and the Tropical Rainfall Measuring Mission (TRMM) Precipitation Radar (PR) acquired 3 minutes apart. The local freezing level is plotted in black on both cross-sections. Grey dots indicate rain top height inferred from the inflection point in each CloudSat reflectivity profile. Right: CPR reflectivity profiles for a stratiform (green) and a convective (blue) precipitation profile extracted from this cross-section. Dot-dashed lines indicate rain top height while the black dashed line indicates the local freezing level.

2.3.1 Defining Convective Objects

Deep convective systems are generally characterized as having one or multiple strong up-draft regions, or convective cores, that produce convective rain. Surrounding the convective cores are often extended stratiform precipitating regions and horizontally-spreading non-precipitating anvil clouds associated with the mature stage of convective storms. With this convective characteristic framework, we identify convective objects using the 2CPC convective core identification method described above for all CloudSat CPR observations obtained between the full 11-year period that CloudSat was in orbit. There are occasional gaps in the data during these four years during periods when CALIPSO

data is missing, but these gaps are generally short and only amount to 0.4% of the days covered by the analysis period. The object-identification approach couples the precipitation flags from 2CPC to reflectivities from 2B-GEOPROF and cloud top heights stored in 2B-CLDCLASS-LIDAR, and consists of the following key steps:

1. The 2B-GEOPROF cloud mask is used to mask reflectivity values along a CloudSat granule that are considered clear-sky, ground clutter, and regions flagged as multi-layer clouds (Z not valid if Z < -28 dBZ, Z < 50 dBZ, or cloud mask < 2 or = 5).

2. Convective cores along a CloudSat overpass are identified by pixels (1.4 km × 1.8 km at nadir) labeled as *convective precipitation* in the 2CPC "Conv_strat_flag".

3. CALIPSO-detected cloud are filled with fake Z values (Z = -30 dBZ) between cloud top and cloud base heights from 2B-CLDCLASS-LIDAR along CloudSat overpass to account for thin anvil or detrained cirrus that CloudSat cannot detect. If cloud base height of highest cloud is higher than the cloud top height in the layer below then it is deemed as multi-layer. The cloud layer below the highest cloud is then filled.

4. The skimage Python function from scikit-image for image processing (van der Walt et al., 2014) is used to detect all connecting pixels in 2D space along the CloudSat overpass. Each unique "cloud object" is assigned a label. The vertically lowest unmasked value within the atmospheric column of the first pixel of a convective core becomes the "convective object label".

5. The boundaries of the CO are defined by identifying either gaps in the along-track cloud field or sharp gradients of cloud top height. It follows that the surrounding pixels have the same label as the convective core label and that the pixel has a three-pixel CTH gradient (center finite difference between pixels 1 and 3 applied to pixel 2) less than or equal to 1 km if it is at least two pixels away from the convective core (this pertains to objects that contain an overshooting top in the convective core region, in which case its CTH is likely substantially higher than the surrounding cloudy pixels).

6. COs less than 5 pixels in length (corresponding to a diameter of 9 km) are not counted to avoid including very small systems or cases where CloudSat and CALIPSO only intersected a small part of the CO. COs that are greater than 5000 pixels long are also not included given the likelihood that they might not be organized under the same environments and/or are capturing extensive sheets of thin cirrus.

7. The size and number of distinct convective cores are calculated and stored for each CO, and each object is labeled as either single-core or multi-core. Any cores that are separated by only one non-convective pixel (1.8 km) are merged and considered the same core to account for limitations in the effective resolution of the CloudSat CPR due to sidelobes. This method provides an upper limit to the convective core size and a lower limit to the number of convective cores in each CO.

8. Multi-layer clouds are included in each CO, and flags identifying their location are included.

To avoid oversimplifying the physical interpretation of A-Train-observed convective characteristics, we use the term *convective object* (CO). Reflectivity profiles of two COs in Figure 2.2 demonstrate the algorithm's ability to identify COs over a large range of horizontal scales. Figure 2.2a shows a single-core system with an approximate diameter of 33 km. CloudSat likely captured this CO during its initiation phase given its strong updraft region, denoted by the +15 dBZ reflectivity values extending above 15 km in the atmosphere, and minimal anvil extent. The radar signal is attenuated as high as 10 km in the atmosphere in the convective core region.

Figure 2.2b shows a massive multi-core system with 16 cores that extends over 2800 km in diameter. This CO is likely in its peak maturity given the +15 dBZ values at a moderate (5-10 km) height in the atmosphere and the large anvil extent. Given the criteria outlined above, overlying thin anvil that is detected only by CALIPSO is considered part of the CO and is portrayed by the area shaded in with fake -30 dBZ values in Figure 2.2b. This sensitivity to thin anvil is a strength for assessing the true radiative effects of the entire CO whether or not the anvil is dynamically coupled to the system. Figure 2.2b also represents a case in which the CO may be cut off at the equator, since CloudSat granules start and end at the equator. In such cases, the complete CO is reconstructed by identifying the accompanying CO in the previous or subsequent overpass if found. Only 0.3% of the database is found to have COs split at the equator. CloudSat can also pass through the center of a tropical cyclone (Luo et al., 2008b) and although much more rare, passing through an eye that is clear of clouds will also result in the cyclone being split into paired convective objects.
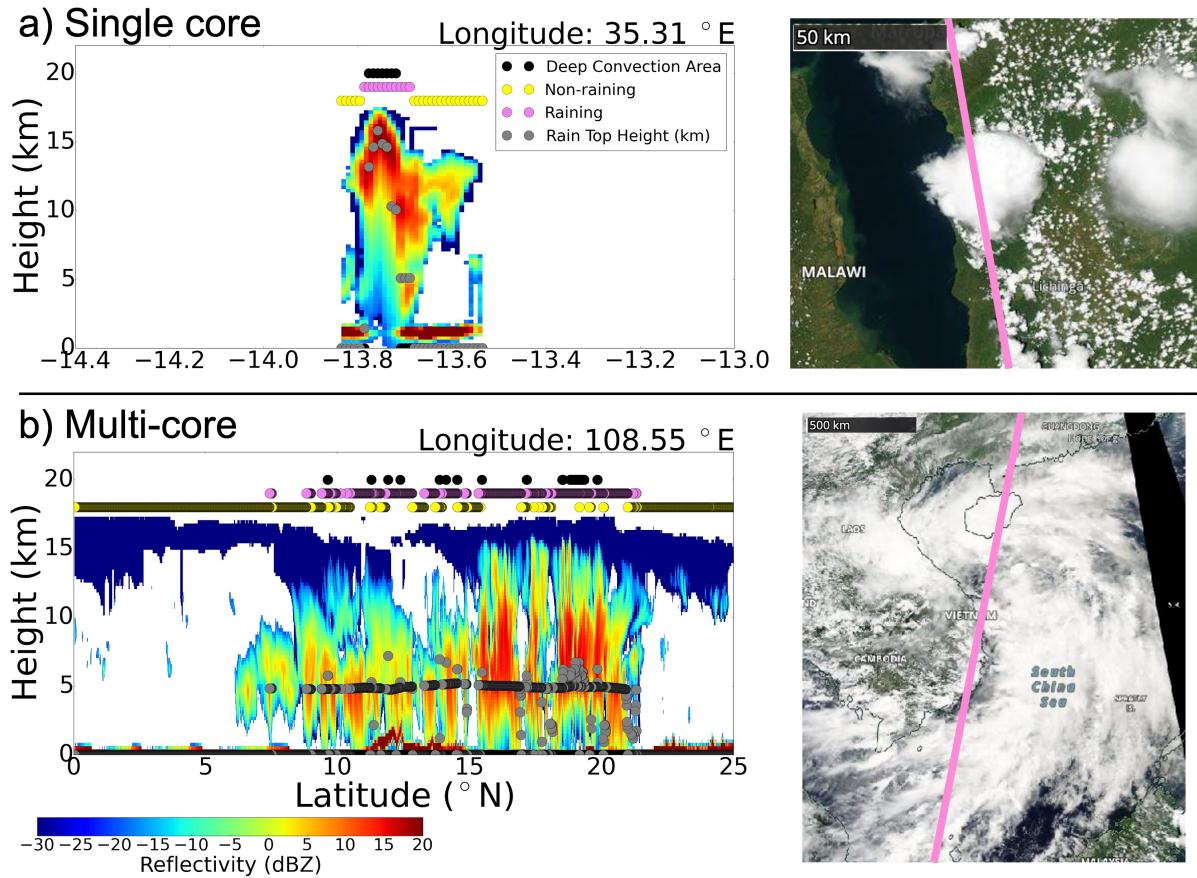
FIGURE 2.2: (Left) Vertical CPR reflectivity profiles of (a) single-core and (b) multi-core COs. CO properties highlighted by the colored circles: Black dots indicate convective areas, pink dots delineate raining profiles, yellow dots indicate non-raining cloud, and grey dots show the 2CPC rain top height. Cloud top heights and bases detected by CALIPSO and stored in 2B-CLOUDCLASS-LIDAR are given fake reflectivity values of -30 dBZ and are shaded in as dark blue. (Right) MODIS corrected reflectances of each CO event taken from NASA Worldview with the CloudSat flyover overlaid in pink.

2.3.2   Convective Core Center of Gravity

The convective updraft region is responsible for transporting energy and moisture to the upper levels, as well as generating precipitation. The amount of ice detrained and latent heat released in a convective object depend on the size, number, and intensity of updrafts within it (e.g. Deng et al., 2016; Mace et al., 2006; Yuan and Houze, 2010; Yuan et al., 2011). The vertical velocity of a convective updraft defines its intensity (LeMone and

Zipser, 1980), but there are currently no direct global measurements of vertical velocity in convective systems. Studies using combined geostationary satellite and radar observations have collocated IR cloud top temperatures (CTTs) with a radar-based proxy for vertical development to infer intensity (e.g. Liu et al., 2007; Luo et al., 2009, 2008b; Masunaga et al., 2005, and others). For example, Liu et al. (2007) used TRMM PR +20 dBZ height, or echo-top height (ETH), as an estimate for vertical intensity as it corresponds to the height at which precipitation-sized particles are located. They found that the coldest cloud tops most frequently occur over the tropical West Pacific Ocean, yet clouds with ETH above 10 km more frequently occur over tropical land, highlighting the complex relationships between cloud top height and this particular precipitation-based proxy for intensity (Liu et al., 2007).

The CloudSat CPR is able to detect the -28 dBZ cloud ETH of convective storms in addition to providing proxies for precipitation ETH using 0 dBZ and 10 dBZ reflectivities (Haynes and Stephens, 2007; Stephens and Wood, 2007). By measuring the distance between CTH and ETH, multiple studies have classified different types of penetrating convection (e.g. Luo et al., 2008a, 2009, 2008b) and showed that distances correlate with the level of neutral buoyancy within the storm system to argue for CloudSat's abilities in estimating storm vertical intensity (Takahashi and Luo, 2014; Takahashi et al., 2017). Thus, W-band radar measurements carry information about vertical intensity through both the height of precipitation-sized particles as a proxy for the updraft velocity, as well as the vertical extent of cloud tops. To capture this information in a single scalar variable, we adopt the cloud Center of Gravity (CoG). CoG is defined as the height at which the

mean reflectivity-weighted mass of the cloud is located in the reflectivity column, which depends strongly on the vertical distribution of hydrometeors in the atmosphere (Koren et al., 2009; Storer et al., 2014). For a given CloudSat pixel, CoG is defined directly from observed CPR reflectivities as:

$$CoG = \frac{\Sigma_i Z_i H_i}{\Sigma_i Z_i} \qquad (2.1)$$

where Z_i is the reflectivity and H_i is the height from the surface to the ith radar range bin in the profile. The vertical extent of the largest hydrometeors provides an excellent indicator of updraft strength since stronger vertical motion transports more mass to higher altitudes. This increases reflectivities aloft and decreases reflectivity at lower levels due to attenuation leading to higher CoG. Thus the higher the CoG, the more intense the convective core. To avoid contamination from ground clutter, we mask reflectivity values greater than 15 dBZ below the freezing level when calculating the convective core CoG. We intentionally avoid applying attenuation corrections to the observed reflectivity profiles to avoid introducing uncertainties related to drop size distribution assumptions required to relate reflectivity to attenuation, and to capture the additional link between updraft strength and attenuation noted above. The CoG is not, therefore, the true center of mass of the convective core but rather a robust proxy of intensity derived directly from unadjusted CloudSat observations. To limit the analysis to truly convective scenes, we only retain COs where the freezing level is greater than 2 km and the difference between the mean convective core CoG and the freezing level—hereafter referred to as the relative CoG (rCoG)—is greater than 1 km. The use of rCoG in the analyses that follow avoids aliasing variations in CoG due to the decrease in climatological freezing level as latitude

increases.

2.3.3   Variables stored in the Convective Object Database

Variables characterizing convective vertical intensity, size, precipitation, radiative fluxes and effects, liquid and ice content, and environmental conditions are calculated and stored from supplementary A-Train observations and reanalyses for each CO. Table 2.1 provides a list of most of the variables and which satellite or instrument supplied the variable measurements. Note that some of the variables are not available for the full 11-year time period. The full database is planned to be published and hosted on the CloudSat Data Portal Center (`https://www.cloudsat.cira.colostate.edu/`) by spring of 2024.

TABLE 2.1: List of variables in convective object database.

Name	Satellite or Instrument	Time period
Latitude & Longitude of CO	CloudSat	2006-2017
CO Length	CloudSat	2006-2017
Number of Convective Cores	CloudSat	2006-2017
Length of Convective Cores	CloudSat	2006-2017
Cloud Top & Base Heights	CALIPSO	2006-2017
Convective Fraction over raining area	CloudSat	2006-2017
Convective fraction over full CO	CloudSat	2006-2017
Rain Fraction	CloudSat	2006-2017
Non-convective Fraction	CloudSat	2006-2017
Non-raining Fraction	CloudSat	2006-2017
Z-weighted Core CoG	CloudSat	2006-2017
Core Rain Top Height	CloudSat	2006-2017
Fraction of Heights > 0 and 10 dBZ	CloudSat	2006-2017
Mean Height of $Z > 0$ and 10 dBZ for Core	CloudSat	2006-2017
Column- and Volume-Integrated Z	CloudSat	2006-2017
Hydrometeor and near-surface PIA	CloudSat	2006-2017
Fraction Total Attenuation	CloudSat	2006-2017
LW and SW fluxes	CloudSat/CALIPSO	2006-2017
LW and SW COD-weighted Mean CoG	CloudSat/CALIPSO	2006-2017
Integrated LW and SW COD	CloudSat/CALIPSO	2006-2017
Fraction of Anvil with COD < 1, $1 < 3$, and > 3	CloudSat/CALIPSO	2006-2017
Lidar-detected Convection	CALIPSO	2006-2017
CALIPSO-Only Regions	CALIPSO	2006-2017
Column-Integrated Ice Water Path	CloudSat	2006-2017
Column-Integrated Snow Water Path	CloudSat	2006-2017
Rain Rates	CloudSat & AMSR-E/AMSR2	2006-2017
Mean Column Water Vapor	AMSR-E/AMSR2	2006-2017
Mean Cloud Liquid Water Path	AMSR-E/AMSR2	2006-2017
94 GHz Brightness Temperatures	CloudSat	2006-2017
11-micron Brightness Temperatures	MODIS	2006-2017
LW, SW, and Net CRE	CloudSat/CALIPSO	2006-2017
Fraction of NET CRE > 1 and < -1	CloudSat/CALIPSO	2006-2017
LW and SW Radiative Fluxes	CloudSat/CALIPSO	2006-2017
Cloud Impact Parameters	CloudSat/CALIPSO	2006-2017
Instantaneous Mean SST	MERRA	2006-2010
Instantaneous Mean CAPE	MERRA	2006-2010
Instantaneous Mean 500 hPa Vertical Motion	MERRA	2006-2010
Monthly Mean MERRA2 500 hPa Vertical Motion	MERRA2	2006-2017
Monthly Mean MERRA2 SST	MERRA2	2006-2017
Vertical Wind Shear Magnitude (multiple levels)	ECMWF	2006-2017
Vertical Wind Shear Direction (multiple levels)	ECMWF	2006-2017
Aerosol Optical Depth	MODIS	2006-2017
Aerosol Index (AI)	MODIS	2006-2017

Chapter 3

The Global Nature of Early-Afternoon and Late-Night Convection Through the Eyes of the A-Train

---

[1]Material in this chapter is nearly identical to: Pilewskie, J. A., & L'Ecuyer, T. S. (2022). The global nature of early-afternoon and late-night convection through the eyes of the A-Train. *Journal of Geophysical Research: Atmospheres*, 127, e2022JD036438.

3.1 Introduction

Deep convection plays an integral role in Earth's energy balance through the release of latent heat to the surroundings from water vapor condensing into cloud droplets and precipitation, and via their influence on both longwave (LW) and shortwave (SW) radiation (L'Ecuyer et al., 2015; Manabe and Strickler, 1964; Manabe and Wetherald, 1967; Trenberth et al., 2009). The relative magnitude of these competing radiative effects depend strongly on convective cloud properties such as height, horizontal extent, thickness, and frequency of occurrence (Stephens, 2005). As a result, changes to these properties in a warming climate determine the sign of high cloud feedbacks, or whether the net cloud radiative response contributes additional warming or cooling on the Earth's energy budget (Hartmann and Michelsen, 2002; Lindzen et al., 2001; Ramanathan and Collins, 1991). There is, therefore, a close connection between atmospheric deep convection and the Earth's energy budget and water cycle since global precipitation is balanced by atmospheric radiative cooling (Stephens and Ellis, 2008), which is largely influenced by the vertical distribution of clouds (Stephens et al., 1994). Thus, while documenting the rainfall produced by convection is essential (Simpson et al., 1988), coincident observations of the macrophysical characteristics and spatial organization of convection can help resolve how the energy budget and water cycles are coupled, which addresses a key issue in adequately modeling high cloud feedbacks (Bony et al., 2015; Sherwood et al., 2014; Stephens, 2005).

Ground-based radar observations have provided plenty of insight on convective storm

structure and precipitation characteristics regionally over decades of field experiments (e.g. Cifelli et al., 2007, 2008; Feng et al., 2015; Houze Jr., 1977; Johnson et al., 1999; Pereira and Rutledge, 2006; Steiner et al., 1995; Stephens and Wood, 2007). Such measurements have also provided context for how mid-latitude storms differ from those in the tropics (e.g. Jensen et al., 2016; Solomon et al., 2016) and how land-based convection differs from that over the oceans (e.g. Liu et al., 2008a; Liu et al., 2007; Nesbitt et al., 2000; Zipser et al., 2006). Yet, ground-based radar observations are constrained to the immediate vicinity of the radar and provide limited insight into storm net radiative effects. Exporting this regional information to global convection, including that over the remote ocean regions, and linking radiative and hydrologic effects requires an alternate perspective that can only be provided from multi-sensor space-based measurements. Satellite remote sensing covers a more extensive region than that of ground radar making it useful for studying convective storm frequency and properties on a global scale (e.g. Hart et al., 2019; Iguchi et al., 2018, 2000; Laing et al., 2011; Liu et al., 2008a; Masunaga et al., 2005; Nesbitt et al., 2000; Zipser et al., 2006). These measurements distinguish the horizontal extent, cold cloud features, and life-cycle of storm systems on a near-global scale (Williams and Houze, 1987). Yet, a major limitation of geostationary satellite observations has been acquiring information about storm structure and precipitation below cloud top. Spaceborne radar such as the precipitation radar (PR) on board the Tropical Rainfall Measurement Mission (TRMM) (Iguchi et al., 2000) and the Dual-frequency Precipitation Radar (DPR) aboard the Global Precipitation Measurement (GPM) (Iguchi et al., 2018; Meneghini et al., 2021) overcome this limitation by penetrating into storms and

capturing their vertical structure of cloud and precipitation features like ground-based radars (Nesbitt et al., 2000).

Several studies developed a three dimensional portrayal of tropical convective systems using data from TRMM PR (Liu and Zipser, 2013; Liu and Zipser, 2008; Liu et al., 2008a; Liu et al., 2007; Masunaga et al., 2005; Rapp et al., 2005; Zipser et al., 2006). The high temporal resolution of TRMM allows it to track convective intensity and precipitation changes diurnally over both land and ocean (e.g. Liu and Zipser, 2008; Nesbitt and Zipser, 2003; Shige et al., 2017). It has been found that the most intense convective systems occur over Amazonia and the Congo Basin (Zipser et al., 2006) and that convection peaks during the afternoon over land suggesting that convection over land is strongly influenced by daytime radiative heating. This result differs over the ocean as there is only a slight ($\sim 10\%$) increase in rainfall amount during the early morning, primarily due to the increase in mesoscale convective systems (MCSs) as opposed to an increase in rainfall intensity (Nesbitt and Zipser, 2003).

However, there remain limitations to understanding the full spectrum of convective system influences on the global energy and water cycles using TRMM measurements. TRMM only samples up to 37°N/S, so the aforementioned studies did not observe storms outside of the tropic and subtropical regions. Its successor, GPM, extended the range to 68°N/S to measure precipitation in the upper latitudes (Hou et al., 2014; Iguchi et al., 2018; Meneghini et al., 2021). Additionally, the PR has a horizontal resolution of 4.3 km, making it sometimes difficult to identify individual convective cores (Zipser et al., 2006).

Furthermore, the limited sensitivity of both the PR and DPR (e.g. Park et al., 2015) do not allow thin anvil and detrained cirrus clouds that are essential for establishing how convection influences energy balance to be detected (Heymsfield et al., 2000; Lebsock et al., 2010; Protopapadaki et al., 2017; Stephens et al., 2004).

Linking the hydrologic and energy budget impacts of convection requires connecting their cloud horizontal and vertical structure to their intensity and precipitation yield (Stephens, 2005). An alternative perspective on global convection that captures the radiative effect of convection can be obtained from millimeter wavelength radar, lidar, and passive sensors aboard the afternoon satellite constellation known as the A-Train (L'Ecuyer and Jiang, 2010). This paper, therefore, presents a comprehensive global data set of convective macrophysical characteristics from A-Train observations to connect the cloud, precipitation, and radiative effects of convection. A number of studies have indicated the value of CloudSat measurements for characterizing the observed horizontal and vertical structures of tropical deep convective systems and how they are influenced by the large-scale environment (e.g. Bacmeister and Stephens, 2011; Igel et al., 2014; Igel and van den Heever, 2015a; Luo et al., 2008a; Yuan and Houze, 2010, 2013; Yuan et al., 2011). Deng et al. (2016) built upon this work by combining CloudSat measurements with highly sensitive data from Cloud-Aerosol Lidar and Infrared Pathfinder Satellite Observation (CALIPSO), also in the A-Train, to detect thin cirrus and investigate deep convective anvil vertical and horizontal structure in differing climatological regions in the tropics. Most notably, they found that supplementing CloudSat measurements with CALIPSO data was necessary for identifying a detrainment layer above 12 km. These

studies suggest that useful insights can be gleaned about the structure and variability of convection despite the A-Train's inability to sample the entire diurnal cycle due to its sun-synchronous orbit. Furthermore, we will demonstrate that the high inclination of the A-Train orbit provides sampling of convection over nearly the entire globe (up to 82°N/S) enabling a global perspective of convection that cannot be obtained with other active sensors.

This paper builds on the aforementioned studies to present a global database of early-afternoon (1:30 pm local solar time; LST) and late-night (1:30 am lST) "convective objects" using an object-identification method from CloudSat and CALIPSO observations. We use a new approach, as introduced in the previous chapter, to identify the location of deep convection by using the two-way attenuation in CloudSat vertical reflectivity profiles. Combining CloudSat reflectivity measurements with CALIPSO lidar backscatter return provide information on CO updraft intensity and horizontal extent. A short discussion on how the CO database for this study is provided in the next section. We conduct a global survey of key convective features: the frequency of occurrence, vertical intensity, horizontal extent, rainfall rates, and cloud radiative effects in Section 3. How these features and their extremes vary with seasons and between day and night are discussed to place results in the context of other satellite-based convection observations. We also highlight three major benefits of using A-Train observations by: 1) distinguishing convective systems at high-latitudes that have previously not been studied for convection, 2) using CloudSat's high vertical resolution to detect individual convective cores for

understanding how single- and multi-core systems relate to cloud and precipitation characteristics, and 3) observing the net cloud radiative effects as a function of the number of convective cores. We conclude with a summary and suggest future analysis pathways in the final section.

3.2 Database Specifications for the Analysis

This study obtains information on convective objects at both 1:30 am/pm LST over the full globe. Because of technical issues with the CloudSat spacecraft in 2011 and CloudSat no longer taking nighttime measurements beginning in 2012, the time period of the current analysis is limited to August 2006 to December 2010. To screen out predominantly stratiform rain systems, we require that at least 2% of the raining area in the CO be classified as convective according to 2CPC to be included in the analysis. This eliminates 8313 COs, or 8.7% of the full database. It is also important to note that COs that meet the above criteria might have 0 mm hr^{-1} rain rates from AMSR-E because AMSR-E is less sensitive than CloudSat meaning that it might not be able to distinguish light rain that CloudSat can observe (Yuan and Houze, 2010). It could also be that the cores distinguished by CloudSat are much smaller than the AMSR-E footprint. Therefore, COs that meet the above criteria but have 0 mm hr^{-1} AMSR-E rain rates are included in the study. Finally, to avoid ambiguity in the location of each CO, their latitude and longitude is assigned based on the location of the convective core that has the largest summed CoG, defined as the mean CoG of a core multiplied by its length.

3.3 A-Train Global Perspective on Convection

3.3.1 Distribution of Convective Objects

CloudSat observes 95,520 convective objects around the globe between August 2006 and December 2010. This large sample provides a first indication of the potential value of a CloudSat-based CO database despite the lack of CPR swath. The distribution of COs is shown in Figure 3.1a. Convective systems are most frequent in the tropics between 15°S to 15°N. Over land, COs are highly concentrated over Amazonia and the Maritime Continent, with a secondary maximum over the Congo Basin. Over ocean, COs are frequently observed in the tropical Indian Ocean, the Pacific Intertropical Convergence Zone (ITCZ), the South Pacific Convergence Zone (SPCZ), and, to a lesser extent, in the Tropical North Atlantic Ocean. The pattern of CO occurrence is consistent with previous studies observing the location of convective systems with TRMM observations (e.g. Liu and Zipser, 2005; Liu and Zipser, 2008; Zipser et al., 2006).

However, while not as frequent as in the tropics, the A-Train detects many COs in the mid- and even high-latitude regions. COs are frequent over the continental United States (U.S.) and over parts of Asia and Europe at around 40°N and in both the northern Alantic and Pacific Ocean storm tracks. There is a high concentration of COs east of the Rocky Mountains and an even more intense convective hotspot over the Tibetan Plateau. Figure 3.1b, which presents the difference in CO probability between the 1:30 am LT and 1:30 pm LT overpasses, indicates that COs more frequently occur in the afternoon than

late at night over both central U.S. and the Tibetan Plateau. This is consistent with ground- and TRMM-based radar observations of convection peaking in the afternoon in these regions (Easterling and Robinson, 1985; Xu and Zipser, 2011).

Figure 3.1b provides a limited glimpse at the day-night variations in CO occurrence. The largest differences are observed in the tropics. Over most tropical land, early afternoon convection occurs more frequently than during the middle of the night consistent with Nesbitt and Zipser (2003). An exception is the weak nocturnal signal east of the Sierra de Córdoba mountain range (65°W and 30°S), which is capturing the rainfall contribution of mesoscale convective systems that initiate at around 2 pm LT and peak in precipitation during late night and early morning (Rasmussen et al., 2016). Tropical oceanic convection is primarily nocturnal, which is especially noticeable over the tropical West Pacific Ocean. Table 3.1 emphasizes the differences in COs occurrence over land and ocean between these two times of day. Annually, there is a much larger discrepancy between early afternoon and late-night CO population over land than over ocean, which could partly be due to the larger diurnal variation of precipitating storm population exhibited over land than over ocean in the tropics detected by the processing TRMM satellite that samples the full diurnal cycle (Liu and Zipser, 2008; Nesbitt and Zipser, 2003). While CloudSat offers very limited diurnal information, these results show that it does qualitatively capture known day-night storm behavior.

The highest probability of mid-latitude COs over land occurs during the Northern Hemisphere summer, as emphasized in the zonal distribution of COs over land in Figure 3.2a.
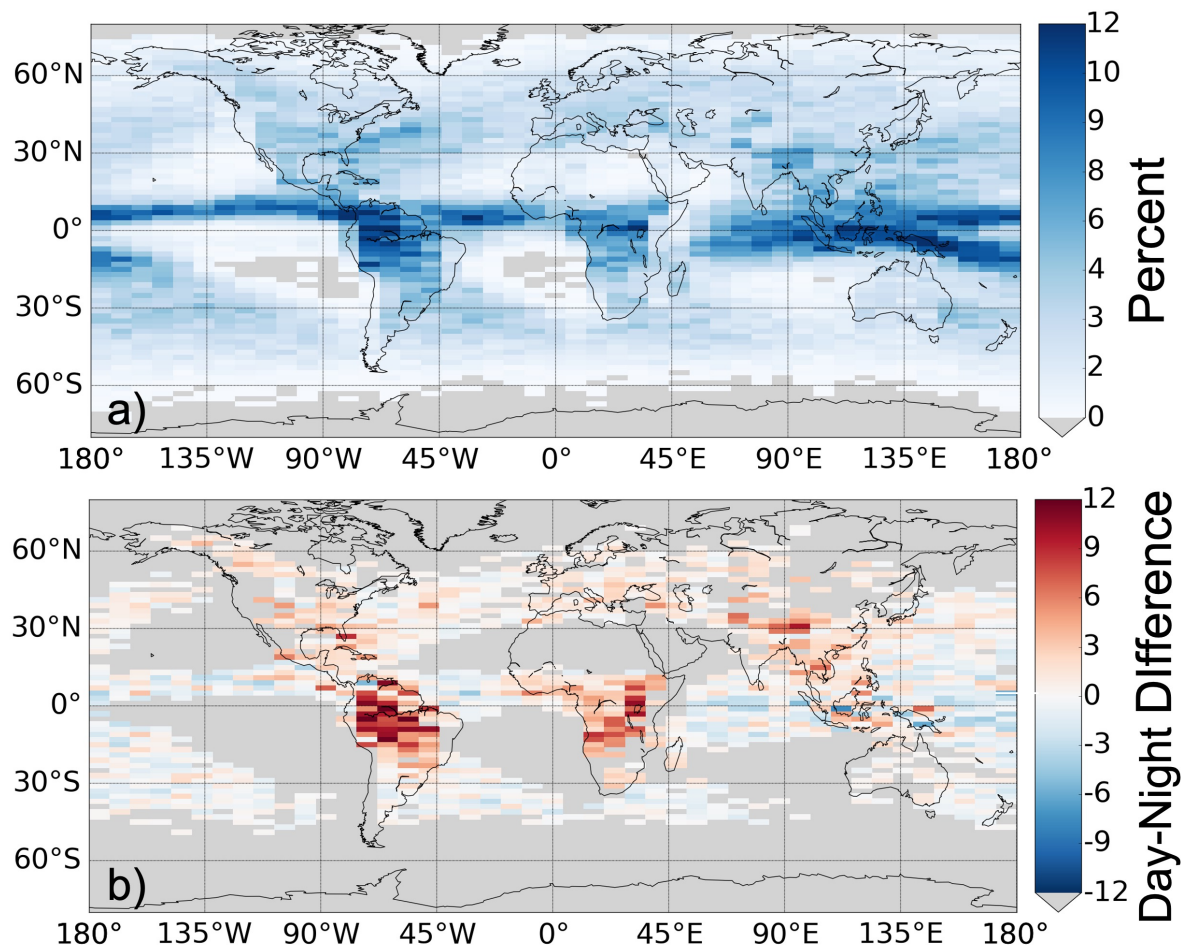
FIGURE 3.1: (a) Percent of CloudSat overpasses that observe at least one CO within each 8° × 2° grid box, and (b) difference in percent occurrence between 1:30 pm (day) and 1:30 am (night) overpasses. Only grid boxes in which at least ten CloudSat COs between August 2006 - December 2010 are plotted

.

When comparing Figures 3.2a and b, Northern Hemisphere convection exhibits a much stronger seasonal cycle than that in the Southern Hemisphere due to the larger land mass. The multi-modal distribution of oceanic COs (Figure 3.2b) is nearly symmetric about the equator, with the highest peak occurring in the Northern Hemisphere ITCZ, and a weaker peak associated with the SPCZ. Convection in the ITCZ exhibits seasonal variability that manifests as both a northward shift and increased CO production during
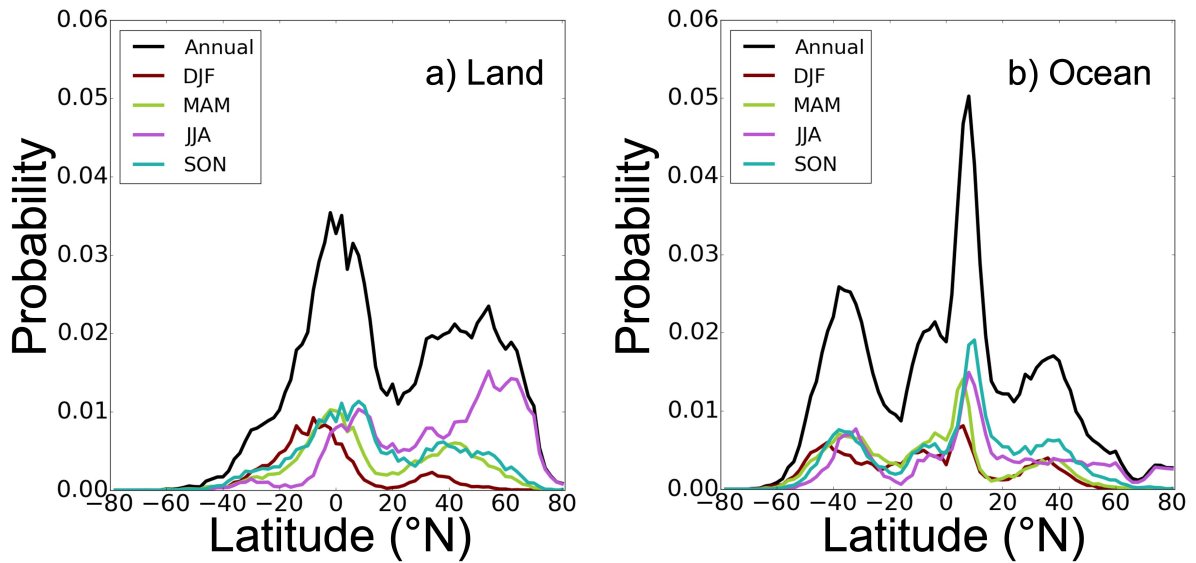
FIGURE 3.2: Probability of observing a CO in a CloudSat overpass in the stated season as a function of latitude over land (left) and ocean (right) between August 2006 - December 2010. DJF = December, January, February ; MAM = March, April, May; JJA = June, July, August; and SON = September, October, November.

TABLE 3.1: Number of convective objects that CloudSat observed between August 2006-December 2010.

	DJF	MAM	JJA	SON	Annual
Land Day	3838	5884	10600	7641	27963
Land Night	2487	3903	6275	4902	17567
Ocean Day	4598	5847	6545	7780	24770
Ocean Night	4779	6045	6743	7653	25220
Total	15702	21679	30163	27976	95520

boreal summer. Meanwhile, COs over the Southern Ocean occur with about the same frequency year-round, which suggests that the seasonal cycle is much weaker.

3.3.2 Convective Characteristics

Global distribution of the intensity, size, and rainfall characteristics of atmospheric deep convection from the twice-daily A-Train observations are shown in Figure 3.3. Vertical intensity is indicated by the mean convective core rCoG of each convective object. The most intense COs are observed in the tropics and land-based convection is substantially stronger than oceanic convection (Figure 3.3a), consistent with previous studies (e.g. Liu and Zipser, 2005; Liu and Zipser, 2008; Zipser et al., 2006). COs in the tropical West African Basin and the Congo Basin are particularly strong with updrafts lifting reflectivity profile center of masses 3-3.5 km above the freezing level, on average. Despite the limited diurnal sampling of the A-Train, CloudSat observes individual COs in this region with rCoGs as high as 9.4 km (or 14.4 km above ground level). COs over the Caribbean islands, central and eastern South America, and Indonesia are slightly weaker than those over the Congo Basin, but frequently quite intense compared to those over the surrounding oceans and mid-latitude land-based convection. Over ocean, COs are strongest off the coast of West Africa and in the tropical North Atlantic Ocean surrounding the Caribbean islands.

The middle row of Figure 3.3 shows the mean and standard deviation of CO size, defined as the length of the CO along the CloudSat ground track. At the times that the A-Train observes convection, COs that are the most intense do not necessarily correspond to where the largest COs occur. Rather, the largest COs, with mean diameters extending up to 2000 km, reside over the Bay of Bengal, Maritime Continent, and the tropical West Pacific Ocean. Deng et al. (2016) also observed 'convective clusters' on the order of

1000 km in diameter over the Maritime Continent and Indian Ocean and classified them as 'super clusters' in which multiple MCSs are connected by merging anvils, defined as mesoscale convective complexes (MCCs; Maddox (1980)).

Figure 3.4 shows that the highest probability of CO occurrence across all sizes are over the Amazon and Maritime Continent, with fewer occurrences over the Congo Basin, tropical Atlantic Ocean, and Bay of Bengal. Small ($<$ 300 km in diameter) COs, which encompass isolated convective cells and MCSs, occur more frequently than bigger COs over west of the Amazon, East Africa, and mid-latitude land and ocean. COs greater than 300 km in diameter are likely signatures of large organized convection, such as tropical cyclones and MCCs, and reside along the ITCZ band over both ocean and land. Almost one-third of the database consists of COs greater than 1000 km in diameter signifying that super cluster systems are rather common (e.g. Deng et al., 2016), particularly over the Maritime Continent, Indian Ocean, West Pacific Ocean, and Central America. While it is appropriate to identify such systems as COs, it is important to recognize that such systems often result from merging thin anvils of multiple convective systems that are not necessarily dynamically connected.

Average precipitation yields, defined as the conditional mean AMSR-E rain rate across each CO, relate more closely with convective intensity than size (Figure 3.3e). COs with the heaviest rainfall are observed over tropical land, particularly the Congo Basin, Amazonia, and East Asia. In the mid-latitudes, the most intense and heaviest rain-producing COs are located over the U.S Great Plains. COs with the lowest mean rain
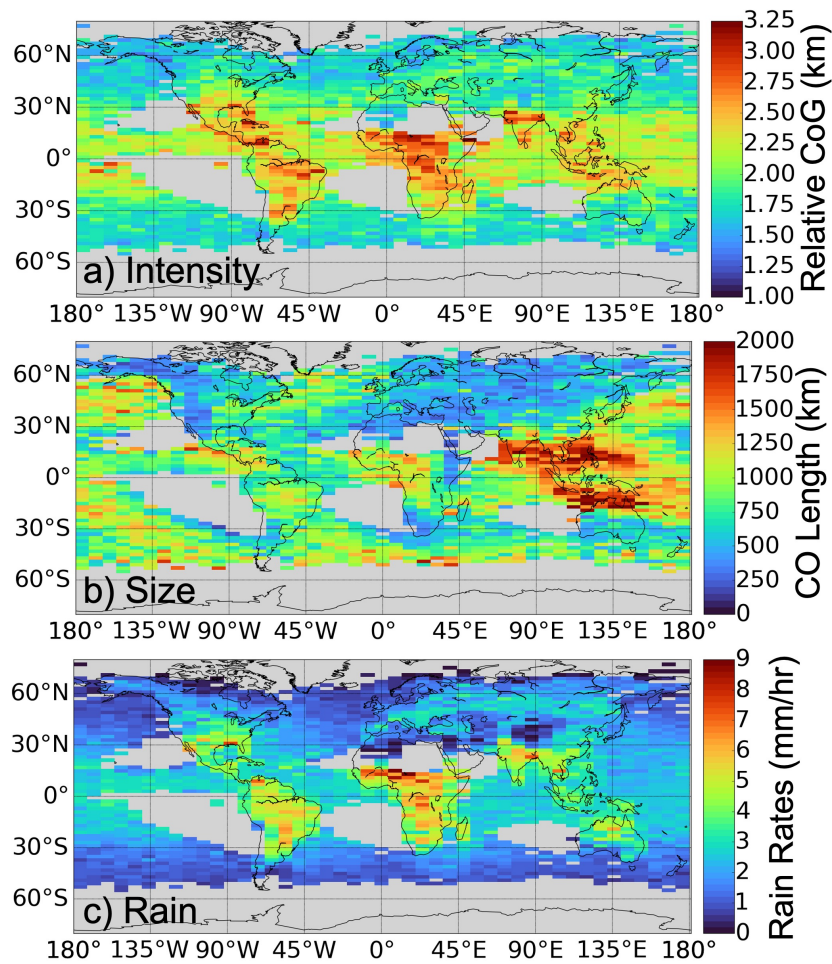
FIGURE 3.3: Mean (left column) and standard deviation (right column) of relative core CoG (top row), CO length along CloudSat overpass (middle row), and rain rates (bottom row) in 8° × 2° grid boxes. Only grid boxes in which at least ten COs were observed are shown.

rates occur over mid- and high-latitude ocean; yet these COs, especially those over the North Atlantic and Pacific Ocean are often mid-latitude cyclones and are larger than land-based COs at the same latitude suggesting that they could still contribute a large amount of total rainfall accumulation at the surface. Hamada et al. (2015) observed that there is a weak link between heavy rainfall and vertically intense convective events, suggesting that it is plausible that the less intense, predominantly stratiform systems may produce the largest surface rainfall accumulations.
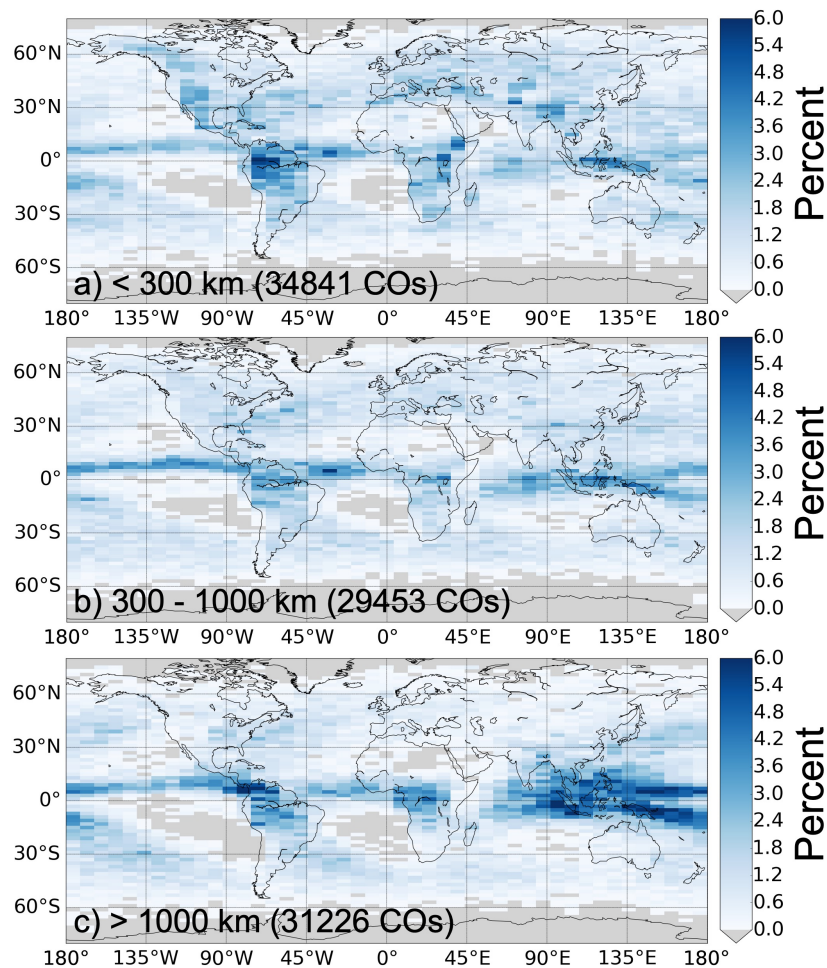
FIGURE 3.4: Percent of COs with lengths (a) less than 300 km, (b) 300-1000 km and (c) greater than 1000 km within each 8° × 2° grid box between August 2006 to December 2010.

Figures 3.3 and 3.4 include both daytime and nighttime overpasses. To provide an indication of the diurnal variation of these convective characteristics, Figure 3.5 shows the discrete probability distributions of tropical CO properties for the 1:30 pm and and 1:30 am overpasses separately. Probability is defined as the number of daytime (or nighttime) land (or ocean) COs within each rCoG, length, or rain rate bin divided by the CO sample size. Note that the land convection includes convection over both inland and coastal regions. Figure 3.5a demonstrates that most of the COs within the tropics have rCoGs

between 1-2 km. This peak is associated with COs less than 50 km in diameter, which includes isolated deep convective systems and potentially cumulus congestus systems that play an important role in forming deep convective systems (Johnson et al., 1999; Luo et al., 2009). More intense rCoGs between 3-7 km are much more likely over land in the early afternoon overpasses than for either ocean or late-night land convection. Daytime oceanic convection is the weakest in A-Train observations while late night convection over land and ocean have similar rCoG distributions that appear slightly stronger than daytime oceanic convection.

Aside from infrequent late night COs over land, the median CO length in the tropics is 20 km (Figure 3.5b). There is no significant distinction in size between early afternoon and late-night oceanic convection but overnight COs over land tend to be much larger than those during the day. COs between 200-700 km in diameter are likely long-lived MCSs that occur with approximately equal frequency over tropical oceans during the day and at night. Over land, however, the A-Train is much more likely to observe smaller developing convection during the early afternoon. On the other hand, early morning convection is predominantly made up of larger mature long-lived systems producing a relatively uniform distribution in CO lengths with a peak at 100 km. COs greater than 1000 km are mature convective complexes primarily observed during the early morning over Central America, the Congo Basin, and Maritime Continent (see Figure 3.3c). The inclusion of thin anvil cloud observed by CALIPSO contributes to the expansiveness of these COs (Deng et al., 2016).
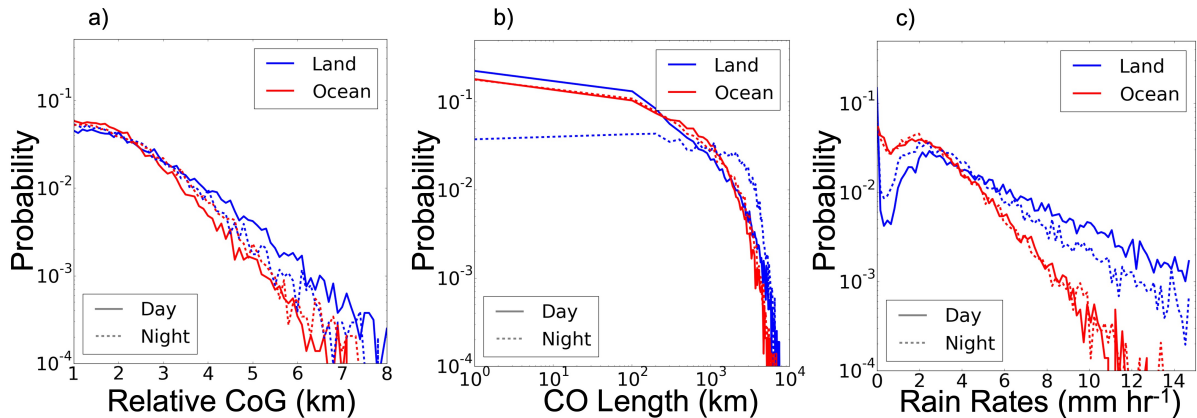
FIGURE 3.5: Discrete probability distributions of mean (a) relative core CoG, (b) CO length along CloudSat overpass, and (c) conditional mean rain rates sorted by day (1:30 pm LT)/night (1:30 am LT) and land/ocean between 30°S and 30°N.

Tropical COs over both land and ocean have median conditional mean rain rates of 3.4 and 2.3 mm h^{-1} respectively. There is a higher likelihood for early afternoon COs over land to have heavy rain rates than late night COs. Oceanic COs have a distinct rainfall mode at 2.5 mm h^{-1} possibly related to deep convective systems. The COs with very light rain rates are likely artifacts caused by rain cells that do not fill the large AMSR-E field of view (FOV). There is little distinction in the 1:30 am and 1:30 pm rain rate distributions for oceanic convection while daytime COs clearly produce more intense rainfall over land (Nesbitt et al., 2000; Zipser et al., 2006).

3.3.3 Top-of-Atmosphere Cloud Radiative Effects of Convection

An important motivation for examining convection in A-Train observations is the fact that it has several sensors capable of measuring not only the macrophysical characteristics of convection, but their radiative responses as well. For example, thin cirrus detected by CALIPSO is included in each CO to provide a more complete depiction of cloud structure

and associated radiative effects. Figure 3.6 shows the spatial distribution of the longwave (LW), shortwave (SW), and net radiative effects of COs observed by the A-Train. To approximate SW cloud radiative effects (CRE) over the full day from twice-daily A-Train measurements, SW fluxes are normalized by the diurnally-averaged insolation following the procedure outlined in Matus and L'Ecuyer (2017) and L'Ecuyer et al. (2019).

On average, a CO enhances the atmospheric greenhouse effect by 77.7 W m^{-2} while increasing reflection by 120.2 W m^{-2} resulting in a net radiative effect of -42.5 W m^{-2} per CO. The radiative effects of individual COs, however, vary widely with location, season, intensity, and size. Figure 3.6a shows that the enhanced greenhouse effect from COs is the greatest over central and southern Africa, U.S Great Plains, western Australia, and upper East Asia. Average COs contribute much less enhanced warming across NH mid-latitude land and ocean and the southern oceans. Likewise, convective clouds over inland Asia and the mid-latitude continental regions generate a large cooling impact by reflecting incoming solar radiation. When combined with their limited LW warming, COs in these regions contribute the largest net cloud radiative cooling. This is a result of the fact that mid-latitude convection predominantly occurs during summer months when solar insolation is strong. Conversely, intense COs over the tropical West Pacific and Congo Basin exert similar impacts on SW and LW radiation resulting in small net CRE. COs produce a subtle enhanced net warming over arid regions of central Africa, upper East Asia, and central Asia where large, thin cirrus anvils accompany brighter precipitation regions (Figure 3.6e). Together, the vertical intensity, spatial scale, rainfall, and radiative characteristics presented in Figures 3.3 and 3.6 illustrate the potential value of A-Train
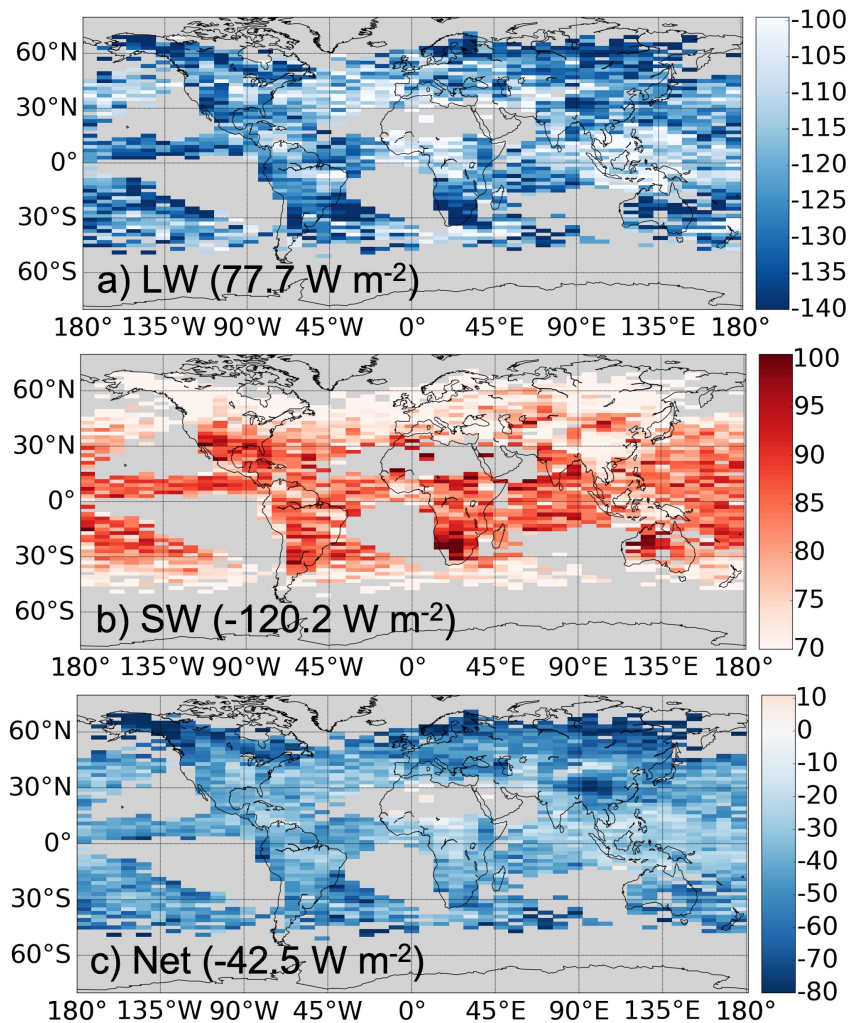
FIGURE 3.6: Mean (left column) and standard deviation (right column) of longwave (LW; top row), shortwave (SW; middle row), and net (bottom row) top of atmosphere (TOA) cloud radiative effect (CRE) of daytime convective objects in 8° × 2° grid boxes. SW fluxes are normalized to diurnal mean solar insolation. Only grid boxes in which at least ten COs were observed are shown.

observations for linking the energy and water cycle impacts of convective systems to their intensity.

3.3.4 Representation of Extreme Convection

Extreme convective systems are deviations from the long-term climatological mean that have tremendous societal impacts and disproportionately influence the energy and water

cycles (Zipser et al., 2006). It is of considerable interest to document the most intense, largest, and heaviest raining storms on a global scale. While the 1:30 am/pm A-Train overpasses do not capture all extreme convection, their detailed observations of convective cloud characteristics on a nearly global scale provide new insights into extreme convective properties. The lefthand side of Figure 3.7 identifies the COs with the 10%, 5%, 1%, and 0.1% highest mean rCoG, largest CO length, and heaviest conditional mean rain rate observed by the A-Train between 2007-2010. Consistent with other studies (e.g. Liu et al., 2008a; Zipser et al., 2006), the most intense convection is concentrated in the tropics but its distribution is far from uniform. Tropical convection over land is more intense than over the ocean with the Congo Basin, Amazonia, Caribbean islands, Southeast Asia and Indonesia containing 41% of the COs in the top 10% of mean rCoG and all but 27 of the 96 COs in the top 0.1%. Intense convection over land extends to the mid-latitudes and, in fact, a few of the top 5% most intense COs are observed as far north as 68°N along the polar circle in Siberia. The most extreme rCoGs over the ocean are primarily observed over the tropical Pacific Ocean between 150°E to 150°W.

Figure 3.7b shows that the top 5% most intense COs in NH spring (March, April, May; MAM), fall (September, October, November; SON), and winter (December, January, February; DJF) reside predominantly in the tropics. For reference, the sample size of COs sorted by extreme convection for each season is given in Table 3.2. There is a slight seasonal shift in intense CO occurrence with the ITCZ as the most intense COs shift southward during DJF compared to COs during any other season. During NH summer (June, July, and August; JJA), however, intense COs are observed in the mid- and

high-latitudes as far north as 68°N. Summertime radiative heating imparts a large diurnal temperature change over land due to its small heat capacity, supporting convection development especially in the afternoon. As a result, the seasonal modulation of convection over land is quite large with a 90° latitude transition between DJF and JJA. This compares to only a 30° latitude range of oceanic convection between these two seasons.

As previously noted, the largest COs do not always coincide with the most intense COs (Figure 3.7c). While the most intense COs occupy the Congo Basin and Amazonia regions, COs are the largest around the equator over Indonesia and the tropical West Pacific consistent with previous studies (Liu et al., 2007). Furthermore, while the most intense COs consistently occur over tropical land and ocean, the largest COs are confined to latitudinal bands just north and south of the equator. Figure 3.7d shows that these bands more generally follow the seasonal cycle of the ITCZ, with the band north of the equator comprising the largest COs during JJA and south of the equator comprising largest COs during DJF.

Since convection exhibits a strong diurnal cycle, especially over land (Nesbitt and Zipser, 2003), it is important to consider how representative these results are relative to the full convective life-cycle. Liu and Zipser (2008) note that storms are at their peak intensity over tropical land between 4 and 6 pm LT, so the A-Train passes over storms during a period in which they are at a relative minimum but building in intensity. Over tropical ocean, convection has a weaker diurnal cycle but exhibits a small peak in intensity in the early morning local time (Liu and Zipser, 2008). Despite not being able to observe

TABLE 3.2: Counts of the 5% most extreme rCoG, CO length, and mean rain rates in COs that CloudSat observed between August 2006 - December 2010.

	DJF	MAM	JJA	SON	Annual
Relative CoG (> 3.9 km)	710	1132	1410	1524	4776
CO Length (> 2999 km)	1373	964	1144	1297	4778
Rain Rates (> 8.0 mm h^{-1})	756	1057	1522	1441	4776

storms at all times of day, including the preferential time of peak intensity over land, the location of the most intense tropical convective systems that the A-Train observes is consistent with previous studies using measurements, such as TRMM, that are able to capture the full diurnal cycle of tropical systems (e.g. Liu and Zipser, 2008; Nesbitt and Zipser, 2003; Zipser et al., 2006, and others). The A-Train is also capable of capturing the large-scale circulation impacts on convective intensity and precipitation associated with seasonal transitions over land and ocean (Figure 3.7). Thus, while the A-Train CO database lacks true diurnal sampling, CloudSat's ability to identify small convective cores and the capability to characterize associated cloud structure and radiative effects on a near-global scale using A-Train instruments, has the potential to reveal new insights on convective impacts on climate (Deng et al., 2016; Igel et al., 2014; Yuan and Houze, 2010; Yuan et al., 2011).
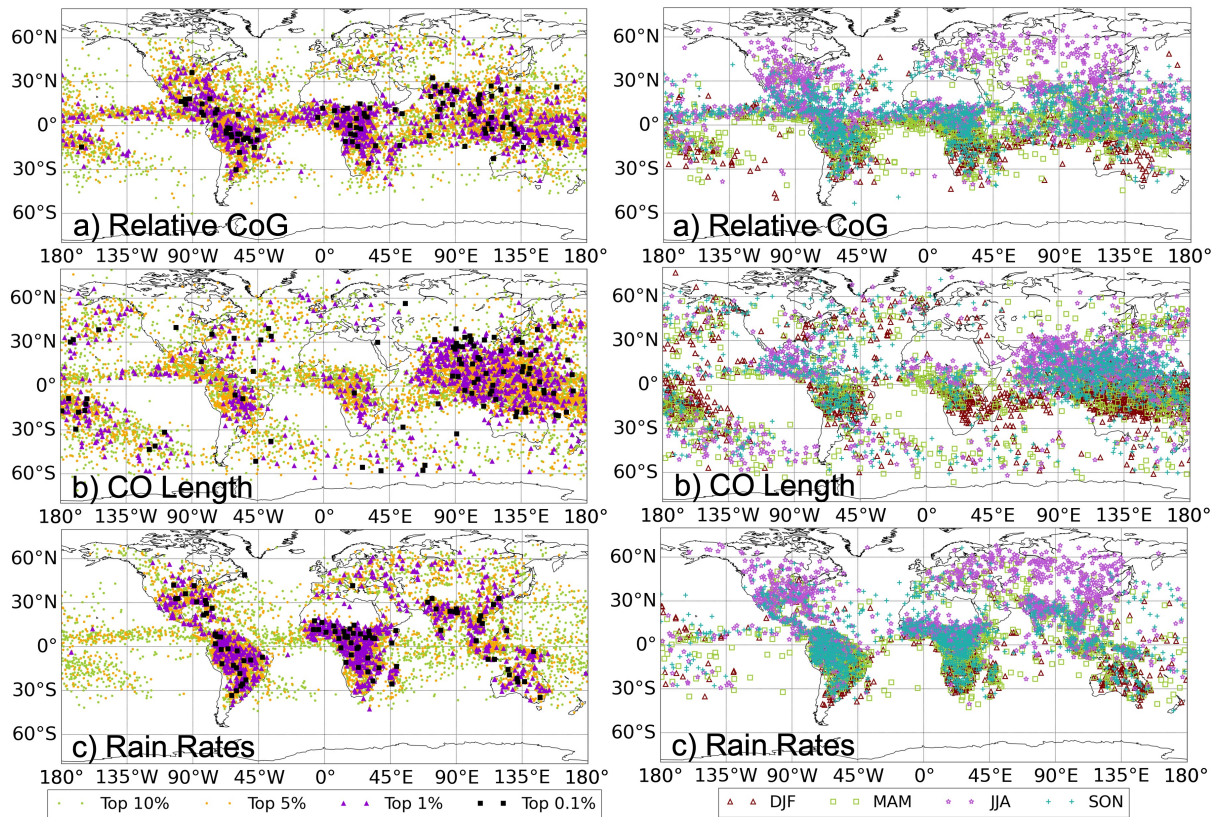
FIGURE 3.7: Top 10%, 5%, 1%, and 0.1% (left column) and seasonal differences for the top 5% (right column) (a-b) most intense convection by mean convective core rCoG, (c-d) largest CO length along CloudSat overpass, and (e-f) heaviest conditional mean rain rates.

3.3.5 Single- and Multi-core Convection

Another potential strength of studying convection using A-Train observations is the ability to identify the minimum number of distinct convective cores in each system, which provides insights into convective dynamics by documenting updraft regions. CloudSat identifies a total of 348,398 embedded cores within the 95,520 COs in the A-Train database. Almost a third of the observed COs are single-core systems (Figure 3.8). However, CloudSat also observes 7,051 COs with at least 10 discernible updraft cores (not shown). One system, observed at approximately 1 pm LT over the North Atlantic Ocean (41°W and

38°N), exhibits 62 distinct convective cores embedded in a large area of stratiform precipitation beneath a connected large overlying cirrus shield. While it is not possible to determine the extent to which these cores were dynamically linked or the result of multiple systems that merged without the addition of time-resolved measurements, this system is a single CO from the satellite perspective. The core properties of this CO is uncharacteristic of COs in the North Atlantic as COs in this region generally have six cores or fewer. In fact, Figure 3.8 shows that COs are more likely ($>50\%$) to have three cores or fewer across the globe. The North Pacific Ocean most frequently exhibits COs with four to six cores. COs with at least seven cores are more frequent than COs with fewer cores over the Bay of Bengal, the Philippines and surrounding ocean, and northern Australia.

A-Train observations provide a pathway for assessing how the updraft regions impact convective structure. For example, CloudSat observations indicate that the mean size of convective cores is 5.97 km. Most convective cores are less than 5 km in diameter for both single-core and multi-core COs, consistent with previous studies (e.g. Giangrande et al., 2013; Wang et al., 2020; Yang et al., 2016), and the top 10% of core diameters are 14.4 km or larger. Figure 3.9 further examines how deep convective macrophysical features vary with the number of cores for both 1:30 pm (day) and 1:30 am (night) overpasses globally. The significance of noted trends are assessed using both a two-tailed t-test and a p-value < 0.05. Figure 3.9a shows that the mean and spread in rCoG is relatively insensitive to the number of cores. This suggests that, on a global scale, there is no direct relationship between intensity and number of cores. On the other hand, mean CO rainfall intensity
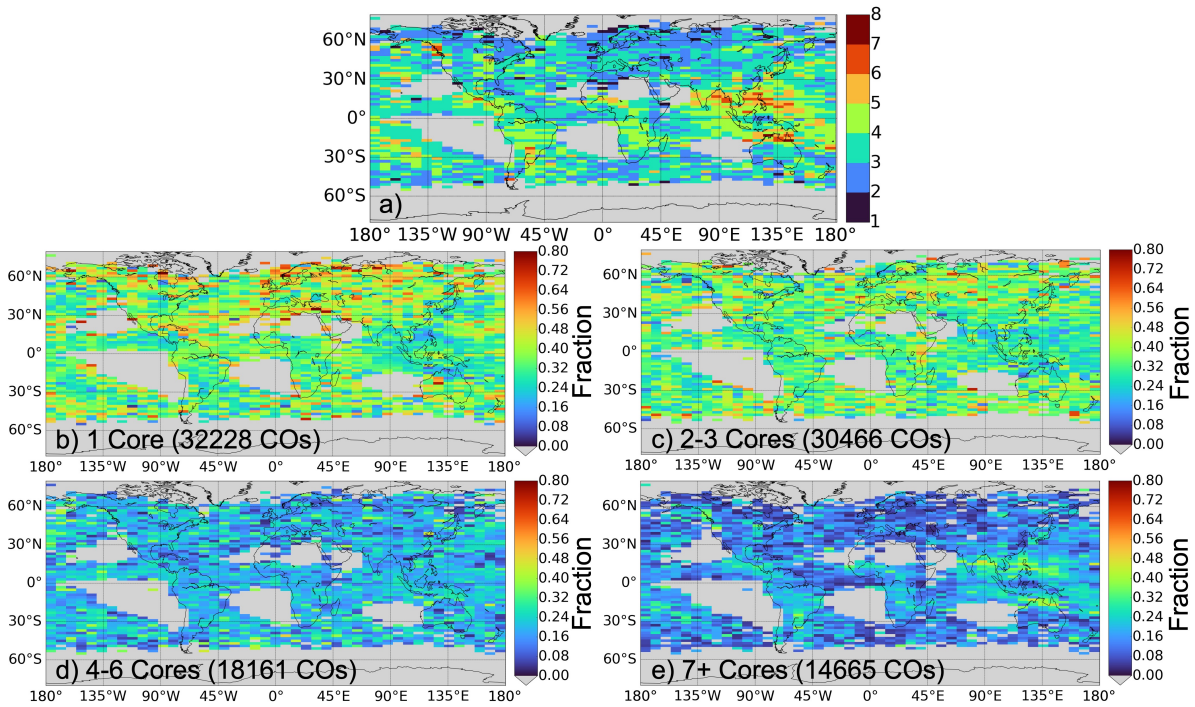
FIGURE 3.8: (a) Mean number of cores and (b-e) fraction of COs with (b) 1, (c) 2-3, (d) 4–6 and (e) 7 or more cores within $8° \times 2°$ grid boxes between August 2006 to December 2010. Only grid boxes in which at least ten COs were observed are shown

increases with increasing number of cores, especially for overnight convection (Figure 3.9b). This may reflect the increased likelihood that single-core systems are developing convection while systems with multiple cores are more likely to be mature convection with higher precipitation intensities (Zhang and Fu, 2018).

CO horizontal extent is more strongly related to the number of cores in each CO, as shown in Figure 3.9c. The mean CO size increases with increasing number of cores, which is consistent with previous findings (e.g. Deng et al., 2016). COs during the late night over-pass are generally larger but also exhibit more variability in size than COs observed in the early afternoon. The variability in CO length for systems containing multiple cores

suggests that multicell CO structure is increasingly complex, as this category can encompass, and is not excluded to, both mature mesoscale convective systems and dissipating plumes with detrained cirrus clouds. Moreover, some multi-core cases may include multiple convective systems that have merged and they may or may not be linked by the same dynamical processes.

Figure 3.9d shows that regardless of the number of cores within a CO, convective fraction, which is the ratio of the convective region to the entire raining region of the CO, is slightly larger in early afternoon than over night. The fraction of the cloud that is convective for COs with multiple cores is less than that of single-core systems owing to the non-convective portion of the cloud growing. Single-core systems that have large convective fractions (>0.5) are likely just initiating without having yet developed anvil, which is noted in Zhang and Fu (2018). Systems being sampled at different storm developmental stages may explain the large spread in the single-core CO convective areas.

The fact that multi-core systems tend to be larger and have more non-convective anvil implies that the radiative effects of COs may depend on the number of convective cores. To test this, A-Train observations are used in Figure 3.10 to relate early afternoon radiative effects to the number of convective cores in a CO—both of which have been difficult to measure on a global scale. This relationship is focused over the tropics so as to avoid the seasonal variability in solar insolation and convective activity at higher latitudes. Again, the significance of noted trends are assessed using both a two-tailed t-test and a p-value < 0.05, and the means are significantly different between all but the last two bins
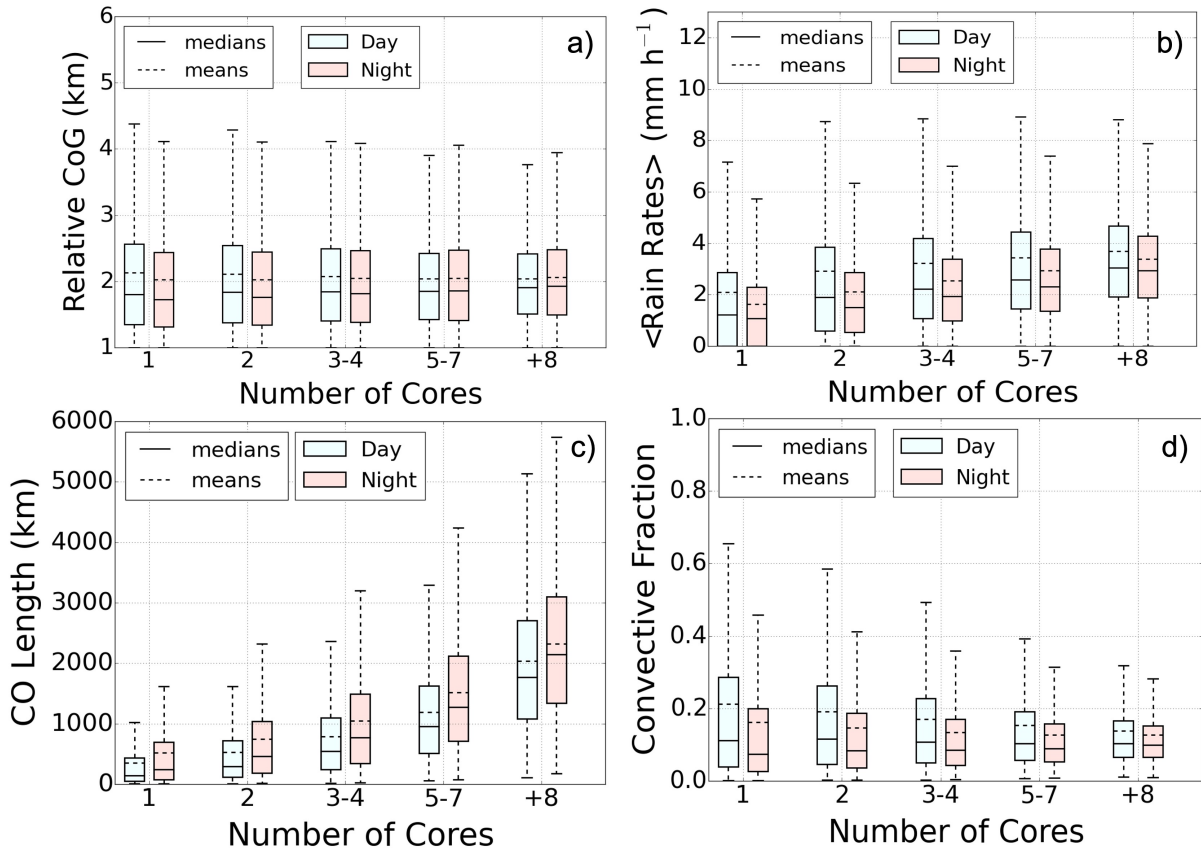
FIGURE 3.9: Box-whisker plots showing (a) rCoG, (b) conditional mean rain rates, (c) CO length and (d) convective fraction for day and night A-Train overpasses sorted by the number of deep convective cores in each system.

(i.e., 5-7 and +8 number of cores). Figure 3.10 shows that over 68% of tropical COs over both land and ocean cool the Earth regardless of the number of cores. Cooling decreases as the number of cores in a CO increases, with single-core systems having the strongest cooling effect. Systems with multiple cores are more expansive and their larger cloud extent associated with non-convective (thin) anvil contributes to LW warming. Single-core systems exhibit the widest range of radiative effects consistent with being sampled at varying life-cycle stages. It is also worth noting that while most COs cool the planet in the early afternoon, there are a subset of COs that warm the climate (also noted in Figure 3.6e) regardless of core count.
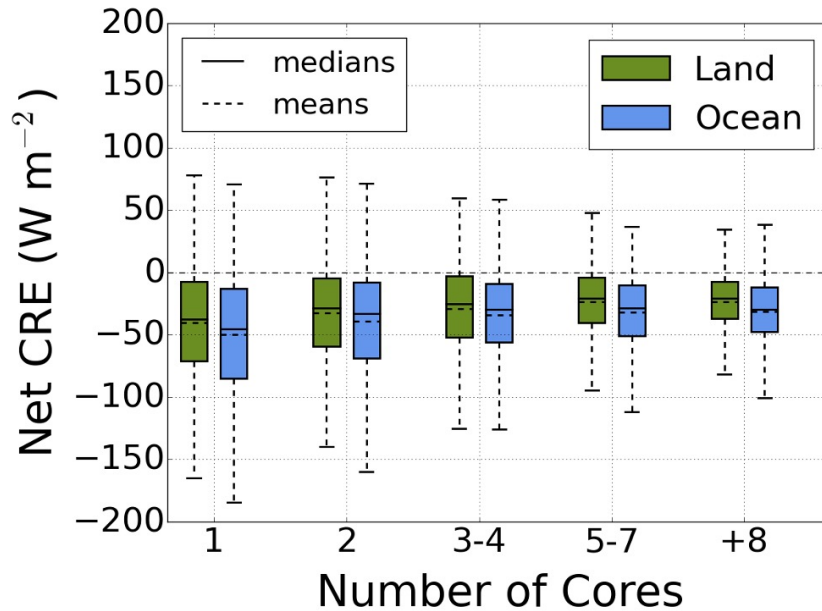
FIGURE 3.10: Box-whisker plot showing daytime (1:30 pm) convective object net CRE over land and ocean between 30°S and 30°N and sorted by the number of deep convective cores in each system.

3.4 Conclusions

A major motivation for exploring convection using A-Train observations is the ability to directly link storm structure, intensity, precipitation characteristics, and radiative effects central to convective cloud feedbacks. Convective objects are observed and characterized by their macrophysical features using four years of combined low-earth orbiting satellite measurements on board the A-Train. By using the attenuation in CloudSat CPR reflectivity profiles, deep convective cores are distinguished from surrounding anvil. The convective core center of gravity relative to the freezing level is used as a measure of vertical intensity as it captures the impact of the updraft in driving large liquid hydrometeors high into the atmosphere. Combining CloudSat measurements with measurements from

other instruments on board the A-Train provides additional information linking storm intensity to structure, precipitation rates, and cloud radiative effects.

Despite not being able to capture the full diurnal cycle or lifetime of convective systems, A-Train convection exhibits characteristics consistent with previous studies. The most intense and heaviest rainfall-producing COs are found over tropical land, particularly over the Amazon, Congo Basin, Latin America, and India, while the most expansive COs exist over the Maritime Continent and surrounding ocean during the two observing time periods. While the convective core CoG and rainfall rate both contribute to defining the updraft intensity of a storm system, the most vertically intense COs occur over both land and ocean while the heaviest rainfall-producing COs are confined to land. Comparing the 1:30 pm and am overpasses shows that the A-Train observes more COs during the early afternoon, particularly over land, than during early morning. When comparing to the diurnal cycle of tropical convection over land, CloudSat's early afternoon flyover captures nearly the minimum in convective activity. Nevertheless, convection over land at this time has a higher percentage of very intense and heavy rainfall-producing COs compared to early-morning land-based convection and oceanic convection at either time of day. The seasonal cycle also strongly influences the location of intense COs and precipitation over land, with frequent COs in the NH's mid- and high-latitudes during boreal summer.

Beyond capturing established characteristics of convection, the high resolution and sensitivity of CPR and CALIOP link convective cloud, precipitation, and radiative properties on a near-global scale. CO size is found to increase with the number of embedded cores

due to an increase in non-convective precipitation and anvil cloud. While COs have a net average cooling impact on the globe, this effect is weaker in COs that have multiple cores owing to this increase in non-convective anvil extent relative to the convective area. In addition, a subset of COs with large cloud to rain areas contribute a net warming of up to 75 W m^{-2}. A particularly striking consequence is that COs exert an average net warming over the arid regions of the Sahel and Gobi Desert. Comparing the size of the convective region to the non-convective anvil might help to explain the radiative response differences between single- and multi-core COs. Yet other factors, such as anvil thickness, vertical intensity, CO life-cycle stage, and environmental conditions, need to be taken into account in order to unpack the large spread in CO radiative response. Determining the factors that govern whether COs have warming or cooling impacts are particularly important when considering convective cloud feedbacks in a warming climate, and is saved for future work.

The narrow swaths and sun-synchronous nature of A-Train observations do introduce limitations for extrapolating CO characteristics to establish the properties of global deep convective storms. For instance, the CO may connect multiple convective systems that are not necessarily dynamically coupled if overlying anvils have merged, skewing the CO diameter to be larger than what is expected of a single convective system. In other cases, when CloudSat does not intersect the center of the storm, CO diameter might underestimate storm equivalent diameter. Moreover, wind shear can cause storms to be oriented in a different direction than the 82° inclined CloudSat track. Neither of these effects are accounted for in this study. Future work is needed to address the relatitve percentages of

CO diameters likely being over- or under-estimated from these effects, although there has been some work done showing that the the characteristic radius of a convective object is sufficiently represented by the diameter that CloudSat measures (e.g. Igel and van den Heever, 2015b). Finally, the A-Train's inability to capture the full diurnal cycle or storm evolution may be partially mitigated by combining such measurements with those that have a higher temporal resolution, such as geostationary satellite observations, to account for storm life-cycle and geographic area and provide deeper insights into convective processes (e.g. Sauter et al., 2019; Takahashi and Luo, 2014).

Chapter 4

A multi-satellite perspective on *hot tower* characteristics in the equatorial trough zone

4.1 Introduction

The *hot tower* hypothesis posited by Herbert Riehl and Joanne Simpson (Malkus) in 1958 and revisited in 1979 (hereafter, RM58 and RS79, respectively) has largely shaped our understanding of tropical deep convective systems impacting large-scale circulations. They argued that individual updrafts, or *hot towers*, transport boundary layer air to the upper troposphere that not only balances local radiative cooling, but also supplies a surplus of energy to be transported to higher latitudes. RM58 and RS79 estimated

that 1500-5000 *hot towers* (modified to 1600-2400 *hot towers* in RS79), each having a diameter of 3-5 km, populate 30 synoptic disturbances at any given time within a region known as the equatorial trough zone (5°S - 15°N) in which energy is exported to higher latitudes within the upper troposphere. However, their estimates were based on analytical calculations with limited access to observations. The focus of this study is to provide an updated *hot tower* estimate using a novel approach that combines multiple satellite observing perspectives of *hot towers*.

The *hot tower* hypothesis propelled both field campaigns, such as Tropical Ocean Global Atmospheres Coupled Ocean Atmosphere Response Experiment (TOGA COARE), and satellite missions such as the Tropical Rainfall Measuring Mission (TRMM), which was proposed and led by Joanne Simpson, to characterize atmospheric deep convective systems, their energetics, and their coupled interactions with the local and large-scale environment (e.g. Chen and Houze Jr, 1997; Johnson et al., 1999; Nesbitt et al., 2000; Reed and Recker, 1971; Yanai et al., 1973; Zipser et al., 2006, among others). Such observations have aided in modifying the definition of a *hot tower*. The initial *hot tower* estimate was made by assuming that updrafts ascend adiabatically, or do not entrain any surrounding air, which imposed restrictions on updraft sizes and vertical velocities (RM58). Early measurements from Global Atmospheric Research Program's (GARP) Atlantic Tropical Experiment (GATE) found that updraft core sizes and vertical velocities are much smaller than what would be required with adiabatic ascent (LeMone and Zipser, 1980; Zipser and LeMone, 1980). It has since been argued that while updrafts entrain air, they can be

reinvigorated through condensational freezing that enables them to supply the necessary moist static energy to the upper troposphere (Zipser, 2003). In the final publication that Joanne Simpson co-authored, idealized model simulations showed that updrafts that reach the upper troposphere and entrain air could supply sufficient energy and mass to the upper troposphere (Fierro et al., 2009). A *hot tower* was redefined as "any deep convective cloud with a base in the planetary boundary layer (PBL) and reaching near the upper-tropospheric outflow layer". It is therefore important to capture the frequency and characteristics of *hot towers* that fit both the initial and updated definitions.

From an observational perspective, convective core sizes and vertical velocities provide insight into the energetic contributions of updrafts. Historically, convective mass flux has been defined using field campaign measurements to understand how much mass is transported vertically within updraft regions (e.g. Byers and Braham, 1948; Giangrande et al., 2016; LeMone and Zipser, 1980; Lucas et al., 1994). However, information from field campaigns is limited to specific regions and times, so they do not capture the statistical properties on a tropics-wide scale. Satellite observations have been implemented to study convective mass flux on a tropics-wide scale (Masunaga and Luo, 2016), but it has proven challenging to quantify convective mass flux because of the inability to measure vertical velocities. A more general term, considered the convective vertical intensity, is an alternative approach to measuring vertical velocities that captures the depth of observed convective cores. Convective core vertical structures from A-Train measurements have been used to estimate the height at which ascending motion ceases and detrainment begins, as well as the height at which precipitation-sized particles extend in the atmosphere

as proxies related to intensity and convective mass flux (Luo et al., 2014, 2010; Masunaga and Luo, 2016; Takahashi and Luo, 2014). More recently, it has been found that the convective core center of gravity (CoG) is a useful estimate of intensity as it captures the vertical hydrometeor distribution, or the mean location of mass in the upper troposphere (Pilewskie and L'Ecuyer, 2022; Storer et al., 2014).

Previous literature has noted that, in addition to condensation within convective updrafts, both the thermodynamic impact of phase changes within stratiform areas as well as the radiative effects by cloud shields heat and influence the moisture within the large-scale surroundings (e.g. Houze Jr., 1981; Stephens and Wilson, 1980). To understand how mass and energy are distributed within, and potentially exported from, the upper troposphere, precipitation amount and cloud extent of convective systems containing *hot towers* must be characterized in relation to their parent convective updrafts. It has been found that wider convective cores that extend deeper into the atmosphere tend to produce larger anvil extents compared to weaker and smaller cores (Takahashi et al., 2021, 2017), suggesting that the most intense cores contribute the most mass in the upper troposphere. However, convective systems have the largest extent and climatologically contribute the most rainfall over the tropical ocean despite not being the most intense (Nesbitt and Zipser, 2003). It has been suggested that the heaviest precipitation is often attributed to stratiform rain and not by the precipitation within convective cores themselves (Hamada et al., 2015; Houze, 1997) despite convective areas generally having higher rain rates than stratiform areas (e.g. Nesbitt et al., 2000; Schumacher and Houze, 2003). These

studies highlight the complex relationships between anvil, precipitation, and convective core properties.

Complexities are often attributed to environmental influences that vary both spatially and temporally. For example, surface temperatures and atmospheric conditions over the Congo Basin and Amazon are ideal for generating the deepest, or most intense, convective systems across the tropics (Heymsfield et al., 2010; LeMone and Zipser, 1980; Lucas et al., 1994; Takahashi and Luo, 2014; Takahashi et al., 2023; Zipser et al., 2006). Temporal cycles also influence convective activity, and these influences vary regionally. While the Intertropical Convergence Zone (ITCZ), which defines the region where precipitation prevails in the tropics, shifts latitudinally over the course of the year over land, there is little latitudinal shift in precipitation over some oceanic regions such as the East Pacific and Atlantic Oceans (Stephens et al., submitted). In terms of how convection changes over the course of the day, there exists a strong diurnal cycle in convective intensity over land but not over ocean. However, there is a noticeable diurnal cycle in convective frequency, anvil horizontal extent, and precipitation that peak in the early morning over the ocean (Chen and Houze Jr, 1997; Liu and Zipser, 2008; Nesbitt and Zipser, 2003; Pilewskie and L'Ecuyer, 2022). Over the Maritime Continent islands, land-ocean interactions that induces land-sea-breeze circulations contributes to a strong diurnal cycle of precipitation (e.g. Miller et al., 2003; van Bemmelen, 1922; Yang and Slingo, 2001). These examples motivate the need for a detailed analysis studying the spatiotemporal variability in convective cores, cloud extent, and precipitation on a tropics-wide scale.

The focus of this analysis is to provide an update on the frequency and spatial occurrence of all deep convective cores and more specifically *hot towers*, and to relate their characteristics to cold cloud and precipitation features using a new multi-year dataset that combines CloudSat and CALIPSO observations with passive satellite estimates of precipitation, outgoing longwave radiation (OLR), and brightness temperatures (BTs). In the next section, we define assumed deep convective updraft regions in two ways: 1) *hot towers* that have cloud tops reaching the tropopause as posited initially by RM58, and 2) deep convective cores that only require cloud top heights to extend beyond the minimum detrainment height (Takahashi and Luo, 2012). Intensity and convective mass flux proxies are defined using combined CloudSat and CALIPSO measurements. The following section compares *hot tower* frequency, intensity, and mass flux proxies to that of all deep convective cores within the tropical trough zone (TTZ; Stephens et al., submitted), which is an updated boundary to the equatorial trough zone. The temporal and regional variabilities of all deep convective core, and exclusively *hot tower*, properties are compared to climatological precipitation and high cloud measurements to relate the strength and location of vertical mass transport to TTZ-wide cloud and precipitation productivity. Finally, a new estimate of how many *hot towers* occur at any given time using a combination of leo-geo observations is provided.

4.2   Data and Methods

4.2.1   Defining the Tropical Trough Zone (TTZ)

The *hot tower* hypothesis was proposed based on the understanding that there is a surplus of energy that exists within the tropics that must be exported to higher latitudes where there is an energy deficit. The ocean supplies most of the heat transported out of the tropics, which makes it challenging to partition between the atmospheric and oceanic contributions of meridional energy transport. As a workaround, RM58 and RS79 reasoned that the oceanic component of meridional heat transport is negligible at the times of year when the sea surface temperature (SST) is at a maxima or minima (local rate of change of SST is zero) as no energy can be gained nor exported. They found that these local maxima and minima occur at the end of February at 5°S and August at 15°N. These latitudes became known as the bounds of the equatorial trough zone, which is a 10-degree latitudinal band that shifts 10 degrees over the course of a year. Thus, the equatorial trough zone is considered the region where tropical deep convection contributes to meridional atmospheric energy transport.

Stephens et al. (submitted) used CERES radiative flux measurements to update this analysis and found that 13°S and 19°N are the latitudes at the end of February and August, respectively, that define the dividing lines between energy transfer to both summer and winter poles. This updated region is renamed as the Tropical Trough Zone (TTZ) to match the fact that the latitude bounds extend to higher latitudes within the tropics

(i.e., not confined to the equator) compared to the bounds of the equatorial trough zone. The present study focuses on convective characteristics within the 32-degree TTZ at all times of year. We do not constrain the band to be 10 degrees that shifts over the course of the year, meaning that our *hot tower* estimate is calculated over the 32-degree extent.

4.2.2 Defining deep convective cores and *hot towers* from an A-Train perspective

This study uses a combination of measurements from satellite members of the A-Train constellation. Launched in 2006, CloudSat is a nadir-pointing satellite with a 94 GHz Cloud Profiling Radar (CPR) that made twice-daily measurements at 0130 and 1330 local solar time (LST) between August 2006 to March 2011 and transitioned to operating only during the daytime beginning in 2012. A unique feature of the CPR is that it has a minimum sensitivity of -30.5 dBZ, meaning that it is sensitive to cloud droplets and light precipitation (Stephens et al., 2002). However, because of the short wavelength, the radar attenuates when encountering precipitation-sized hydrometeors. It has a 1.4 km cross-track resolution and 1.8 km along-track resolution, with a vertical resolution of 480 m that is oversampled to 240 m that enables it to capture vertical characteristics of convective systems (Tanelli et al., 2008). Stephens et al. (2008) provides an overview of the CloudSat mission, and detailed information on 2B-GEOPROF, 2C-PRECIP-COLUMN, and ECMWF-AUX data that are used in this analysis can be found from the CloudSat Data Processing Center at `https://www.cloudsat.cira.colostate.edu`.

Convective characteristics are taken from a "convective object" (CO) database, which consists of identified convective systems using a two-dimensional image detection approach (Pilewskie and L'Ecuyer, 2022). Deep convective cores are identified along CloudSat curtains using the "Conv_strat_flag" variable from the 2C-PRECIP-COLUMN data product. Profiles are flagged as "convective" if the height of the radar attenuates at least 1 kilometer above the freezing level. It is inferred that convective updrafts vertically transported hydrometeors to levels above the freezing level, and their ability to attenuate suggests that these hydrometeors are on the scale of precipitation droplets. Contiguous convective flags along a profile are grouped to define a deep convective core. Because individual updrafts can be under a kilometer in diameter (Giangrande et al., 2013; Wang et al., 2020), which is less than the CPR along-track resolution, it is possible that the diameters of the CPR-detected convective cores are overestimated. Nevertheless, the bulk cloud microphysical response to convective updrafts are captured within these defined core regions (Pilewskie and L'Ecuyer, 2022; Takahashi and Luo, 2014).

In this study, deep convective cores are required to have a cloud top height of at least 10 km following buoyancy reasonings outlined in Takahashi and Luo (2012, 2014); Takahashi et al. (2017). This also follows the updated hot tower definition in Fierro et al. (2009). To be consistent with RM58 and RS79, we define a *hot tower* as a convective core that overshoots the environmental tropopause. In this study, we make no assumptions based on whether cores that reach the environmental tropopause entrain surrounding air. The following criteria are employed to define *hot towers* along a CloudSat overpass:

1. A convective core is identified following the methods outlined above (see also Pilewskie and L'Ecuyer (2022)).

2. Use the 'cloudtype' and 'cloudtopheight' variables from 2b-CLDCLASS-LIDAR to select the height of the cloud layer defined as "deep convection" from each profile within the core (this is to avoid any multi-layer clouds).

3. Calculate the lapse-rate tropopause height (height in the atmosphere when the lapse rate is less than 2 km; LRT) and cold point tropopause height (height of the minimum temperature; CPT) at each convective core location using state variables that are interpolated to each CPR bin from the ECMWF-AUX data product.

4. If the core cloud top height (CTH) has a height greater than 16 km, which is considered the lower limit of the tropopause height in the tropics, and is greater than both the LRT and CPT heights, then it is considered a *hot tower*.

Cloudy pixels that meet the -28 dBZ threshold or are identified by Cloud-Aerosol Lidar with Orthogonal Polarization (CALIOP) on board CALIPSO are connected to the deep convective cores and/or hot towers to create a completed convective object. Figure 4.1 shows a combined CPR-CALIOP cross-section of a synoptic event located over the South Pacific Ocean on January 1, 2009. Several deep convective cores are identified within this system, but only two of them are flagged as *hot towers* as denoted by the shaded blue columns. Within the largest *hot tower*, there is noticeable attenuation above the freezing level signifying that this is an active updraft region. Interestingly, CALIOP detects an
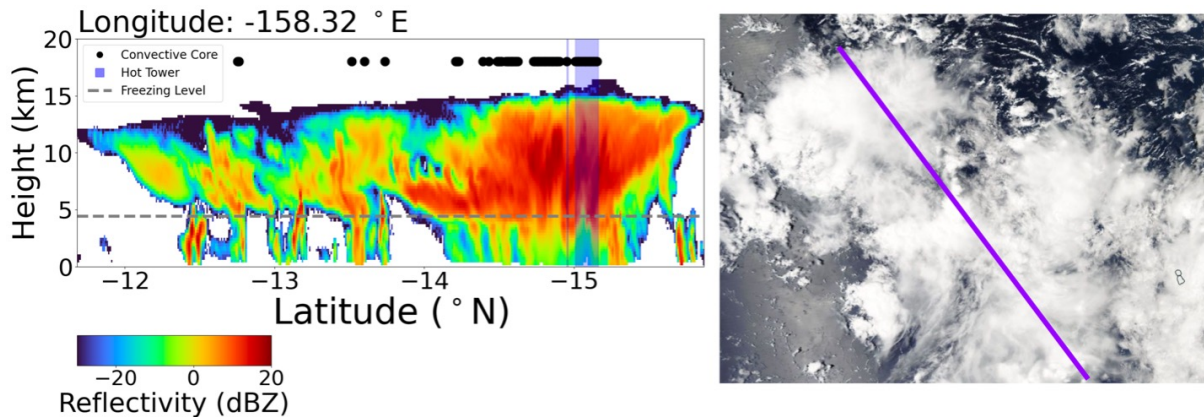
FIGURE 4.1: (Left) CloudSat CPR radar reflectivity profile of a convective system found to have several convective cores (black dots), two of which are flagged as *hot towers* defined by the shaded blue columns. The area between CALIOP-detected cloud base and heights are filled in with "fake" -30 dBZ values. (Right) Aqua MODIS true color corrected reflectances of storm from EOSDIS Worldview. The purple line indicates the location of CloudSat overpass.

overshooting top just south of the *hot tower*, but no active deep convective core is found in this region. This suggests that there could be a temporal lag between an active updraft region and the development of an overshooting top, or perhaps the updraft is sheared.

4.2.3   Accumulated rCoG as a proxy for vertical mass transport

To capture the vertical intensity of convective cores and *hot towers*, we calculate the convective core center of gravity (CoG), which is the center of mass of the convective core weighted by CloudSat reflectivity values. The mean freezing level of the convective object is subtracted from each core CoG (hereafter considered relative CoG, or rCoG) to capture the lofted effect of the largest hydrometeors. More details on this calculation are found in Pilewskie and L'Ecuyer (2022).

A unique index used to capture the energetic impact of tropical storms is the Accumulated

Cyclone Energy (ACE), which is defined as the summed squared estimated 6-hourly maximum sustained wind speed (Bell et al., 2000). Although ACE is not a direct measure of energy, it is credited for capturing the overall impact of cyclone activity on climate by weighing storm intensity by its lifetime (Bell et al., 2000; Camargo and Sobel, 2005). Following similar reasoning, we define accumulated rCoG as the product between the core or hot tower rCoG, length along the CloudSat overpass (hereafter, diameter; D), and number (N) of convective cores or hot towers ($N \times D \times rCoG$) within a given domain. Like ACE, these are continuous measures that can be used to relate to other climate variables (Camargo and Sobel, 2005), such as precipitation and high cloud amount that capture the relationship between vertical and horizontal mass transport. The accumulated rCoG is similar to the convective mass flux in that rCoG is a proxy for the vertical velocity and D represents the coverage.

4.2.4 Contextual precipitation, cloud, and OLR datasets

Although CloudSat and CALIPSO measurements provide detailed information on the instantaneous vertical structures of convective clouds, they are limited in capturing the horizontal high cloud extent both spatially and temporally. Furthermore, these measurements are not able to capture heavy precipitation that often accompanies convective systems. Therefore, additional satellite observations are used to characterize the tropics-wide the distribution of high cloud and the heaviest precipitation in relation to convective vertical mass transport characteristics.

The Global Precipitation Measurement (GPM) mission is a network of satellites designed

jointly between the Japan Aerospace Exploration Agency (JAXA) and the United States National Aeronautics and Space Administration (NASA) to be a follow-on to the Tropical Rainfall Measuring Mission (TRMM) (Lu and Yong, 2018). The GPM constellation carries a Dual-frequency Precipitation Radar (DPR) with both Ku (13 GHz) and Ka (35 GHz) bands in addition to a multichannel (10-183 GHz) GPM Microwave Imager (GMI) (Hou et al., 2014). Integrated Multi-satellitE Retrievals (IMERG) is a level-3 precipitation algorithm that combines all microwave measurements from the GPM constellation with infrared estimates and precipitation gauge analyses to create a global uniformly-gridded climatology of surface precipitation. The GPM IMERG V06B monthly data product provides monthly mean rain rates at a $1° \times 1°$ resolution between January 2006 - September 2021 (Huffman et al., 2020).

The Clouds and the Earth's Radiant Energy System (CERES) project combines radiometric measurements from six instruments hosted on EOS Terra, Aqua, Suomi National Polar-orbiting Partnership (NPP), and National Oceanic and Atmospheric Administration's (NOAA) Joint Polar Satellite System 1 (JPSS-1) satellites to provide a record of top-of-atmosphere and surface radiative fluxes between March 2000 through present-day. CERES Energy Balanced and Filled (EBAF) Edition 4.2 data product is a level-4 product at $1° \times 1°$ resolution that provides monthly and climatological mean clear-sky and all-sky TOA fluxes (Loeb et al., 2018). For this study, we select rain rates and all-sky TOA longwave fluxes over the TTZ between 2007-2016.

Our aim for updating the hot tower estimate is to consider both the spatial and temporal variability of convective core activity. Because of the variability in convective core activity over the diurnal cycle, we employ passive infrared satellite observations that capture inferred convective cloud activity at the cloud top on a half-hourly basis (Janowiak et al., 2017). First, Moderate Resolution Imaging Spectroradiometer (MODIS) 11-micron brightness temperatures from the MOD06-5KM-AUX P1 R05 data product are matched to the identified hot towers to provide a distribution of infrared brightness temperature thresholds. The convenience of using these observations is that MODIS flies on both Terra and Aqua within the A-Train constellation. The MOD06-5KM-AUX P1 R05 data product contains a subset of Collection 6 Aqua MODIS cloud properties (Toller et al., 2013) that are oversampled to match CloudSat CPR footprints at a 5 km resolution using a nearest neighbors approach (Cronk and Partain, 2018). To characterize the diurnal cycle of high cloud top activity across the TTZ that aids in creating a new hot tower estimate, 11-micron brightness temperatures from NCEP/CPC L3 Half Hourly 4km Global (60S - 60N) Merged IR V1 (GPM_MERGIR) data product are averaged at each hour over 2013. GPM_MERGIR is a product created by the Goddard Earth Sciences Data and Information Services Center and provides half-hourly near-global 4-km gridded IR brightness temperature data from European (METEOSAT-5/7/8/9/10), Japanese (GMS-5/MTSat-1R/2/Himawari-8), and US (GOES-8/9/10/11/12/13/14/15/16) geostationary satellites. Data have been corrected for zenith angle dependence to reduce discontinuities at the boundaries of each satellite observing domain (Janowiak et al., 2017).

a)

b)
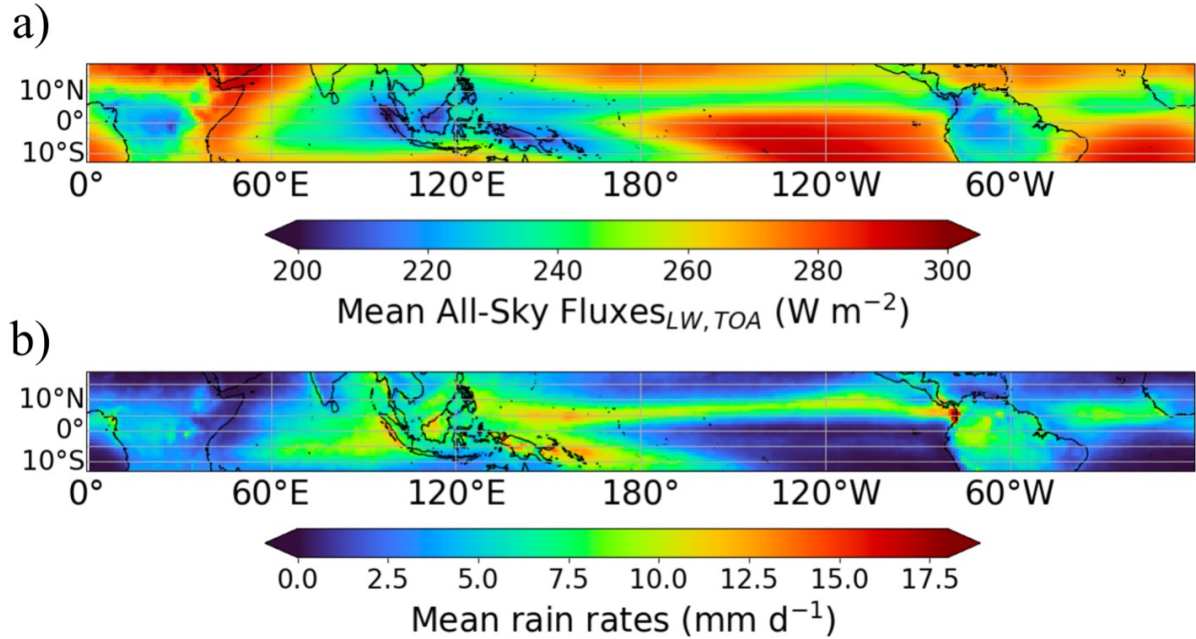
FIGURE 4.2: (a) CERES EBAF (Energy Balanced and Filled) monthly mean top-of-atmosphere all-sky longwave radiative fluxes. (b) Global Precipitation Measurement (GPM) Integrated Multi-satellitE Retrievals (IMERG) monthly mean rain rates. Both are averaged between January 2007 - December 2016.

4.3   Results

4.3.1   Convective core and hot tower characteristics in relation to high clouds and precipitation within the TTZ

Convective updrafts are often associated with producing extensive cloud shields that can spatially organize on scales up to thousands of kilometers (Nakazawa, 1988; Zipser, 1969), denoted by a significant reduction in outgoing longwave radiation (OLR) as shown in Figure 4.2a. These cloud shields are associated with heavy precipitation (Figure 4.2b), particularly in the Intertropical Convergence Zone (ITCZ) and over the Maritime Continent.

Figure 4.3a shows the distribution of deep convective core counts within the TTZ. As a reminder, the deep convective cores follow the relaxed hot tower definition of Fierro et al. (2009). Over the ocean, the highest climatological mean rain rates (Figure 4.2b) occur where deep convective cores are most frequent, suggesting a relationship between core frequency and surface precipitation accumulation. However, over land this relationship is not as apparent seeing that, for example, deep convective cores most frequently occur over the Amazon Basin but do not produce the heaviest rain rates. Likewise, the concentration of convective cores over the Congo Basin is similar to but contributes nearly half the climatological mean rain rates as over the West Pacific Warm Pool and South Pacific Convergence Zone.

Cores are most vertically intense over land, particularly over Africa (Figure 4.3b), as was noted by Zipser et al. (2006) and more recently Takahashi et al. (2023). The sizes of cores are fairly homogeneous across the TTZ–ranging between 6-8 km and are only slightly larger ($\sim$9 km) over Africa (Figure 4.3c). The distribution of accumulated rCoG is found in Figure 4.3e and is primarily weighted by core counts; however, despite there not being as many cores over the Congo Basin as over South America, the mass flux proxies are equal in magnitude in these regions due to cores in the Congo Basin being more intense and larger. Furthermore, continental convection has a higher accumulated rCoG per area than over the ocean and Maritime Continent.

Figure 4.4 presents convective core and mass flux properties of *hot towers*, or deep convective cores that reach the environmental tropopause. In any given area the *hot tower*
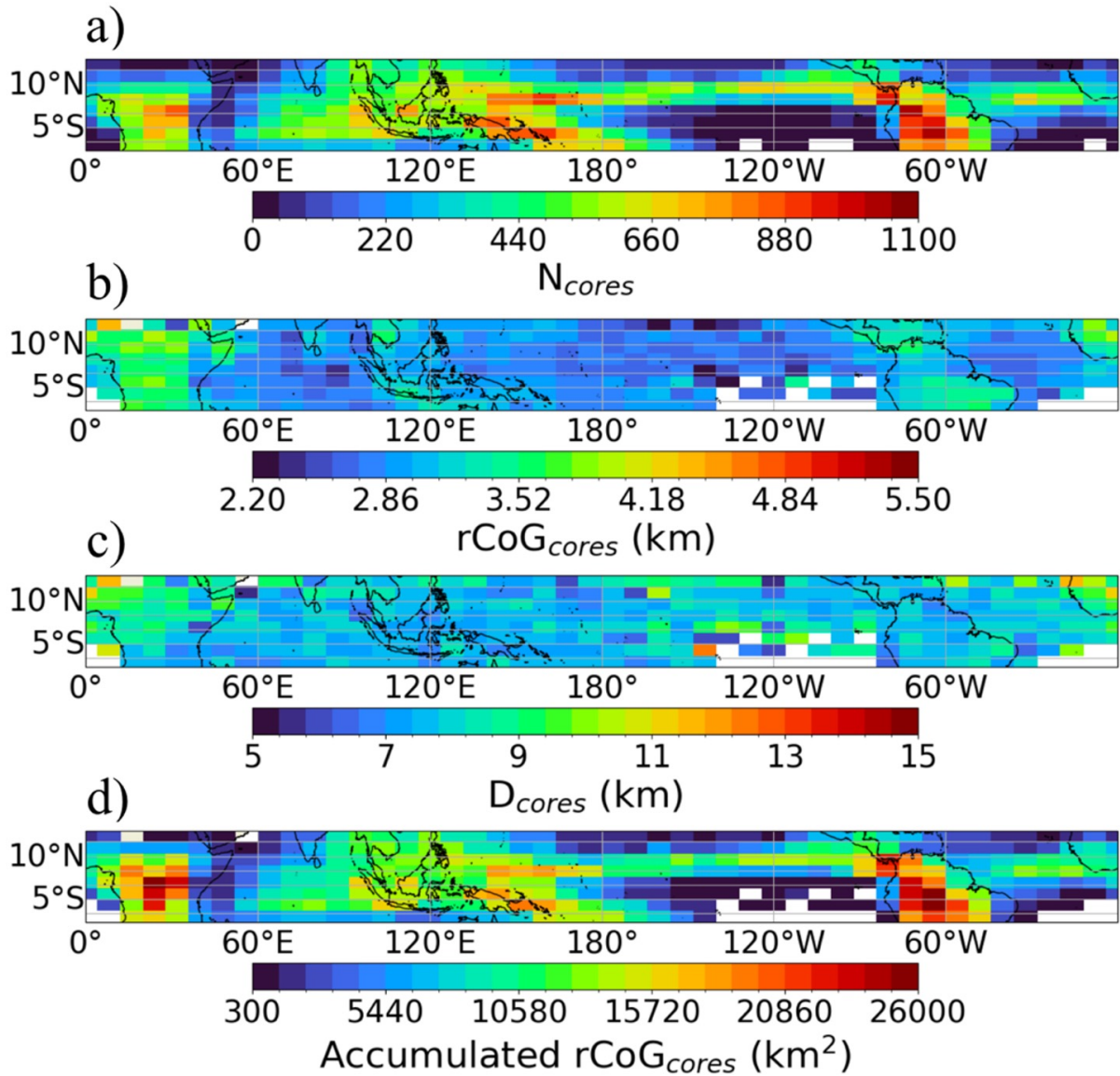
FIGURE 4.3: (a) Number of convective cores, (b) mean core relative Center of Gravity (rCoG), (c) mean core diameter, and (e) *accumulated rCoG* defined as the product between the rCoG, core diameter, and the number of cores in each grid box. At least 20 cores are required in each 8° × 4° grid box for a mean to be calculated. The cores are identified at 1:30 am/pm LST between 2006-2016.

count does not exceed 35% of the total convective core count as shown in Figure 4.4a. The highest fraction of hot towers relative to all cores preferentially occur over regions where convection is thermodynamically driven by warm surface temperatures, such as over India and the Bay of Bengal above 10°N, West Africa, the Congo Basin, and off the coasts of the Maritime Continent Islands. Figures 4.4b-c show that the spatial distribution of rCoG and core sizes for hot towers follows the distribution for all cores. However, hot towers have on average a 128% higher rCoG (Figure 4.4b) and 146% larger (Figure 4.4c) diameter compared to all deep convective cores (Figure 4.3). Figures 4.4d indicates that the largest total mass flux contributions from hot towers are in regions where there are the most counts (not shown). In regions where the fraction of hot towers to all cores is largest, hot towers contribute over 40% of the total accumulated rCoG (Figure 4.3e) owing to their enhanced size and intensity relative to all cores.

Bretherton and Hartmann (2009) note that large-scale vertical motion fields and the vertical velocities of an ensemble of convective systems are coupled. Vertical pressure velocity profiles are climatologically "top-heavy", or higher cloud tops, over the West Pacific Ocean compared to over the East Pacific Ocean, which is associated with "bottom heavy" profiles Back and Bretherton (2006); Bretherton and Hartmann (2009). These characteristics are apparent in Figures 4.3 and 4.4, which show that both the frequency of deep convective cores (Figure 4.3a) and the fraction of cores that are hot towers (Figure 4.4a) over the East Pacific Ocean is less than that over the West Pacific Ocean. Furthermore, cores have a higher accumulated rCoG per area over the West Pacific compared to

over the East Pacific, and the accumulated rCoG contribution by hot towers is at least three times greater over the West Pacific Ocean than over the East Pacific Ocean.

RM58 reasoned that a synoptic disturbance with a wavelength of $\sim$ 1350 km is the main mode of convection within the tropics–10% of which is occupied by active rain and 10% of the active rain is occupied by undilute towers. Figure 4.5 shows the distribution and length scales of the convective objects in which convective cores and *hot towers* reside. COs containing *hot towers* are on the order of 1000 km in length and are most prevalent over the Maritime Continent. Previous literature has noted that this region is dominated by mesoscale convective systems (MCSs) that have merged anvils, otherwise known as "mesoscale convective complexes" or "superclusters" (Maddox, 1980; Mapes and Houze, 1993; Yuan and Houze, 2010).

The distribution of convective objects follows that of the convective core frequency, which is reasonable given that $\sim$ 85% of the objects contain three or fewer coresor hot towers (Figure 4.5a). However, over 50% of COs contain multiple cores suggesting that energy is not being vertically distributed primarily through isolated updrafts. Figure 4.6b-c show the distribution of convective objects sorted by how many convective cores the objects contain. Systems with one core most frequently occur over the Amazon Basin and over Indonesia. COs with greater than five cores most frequently occur over the West Pacific Warm Pool and off the Pacific coast of South America and Indonesian coasts where the highest climatological mean rain rates occur. This is in agreement with previous literature
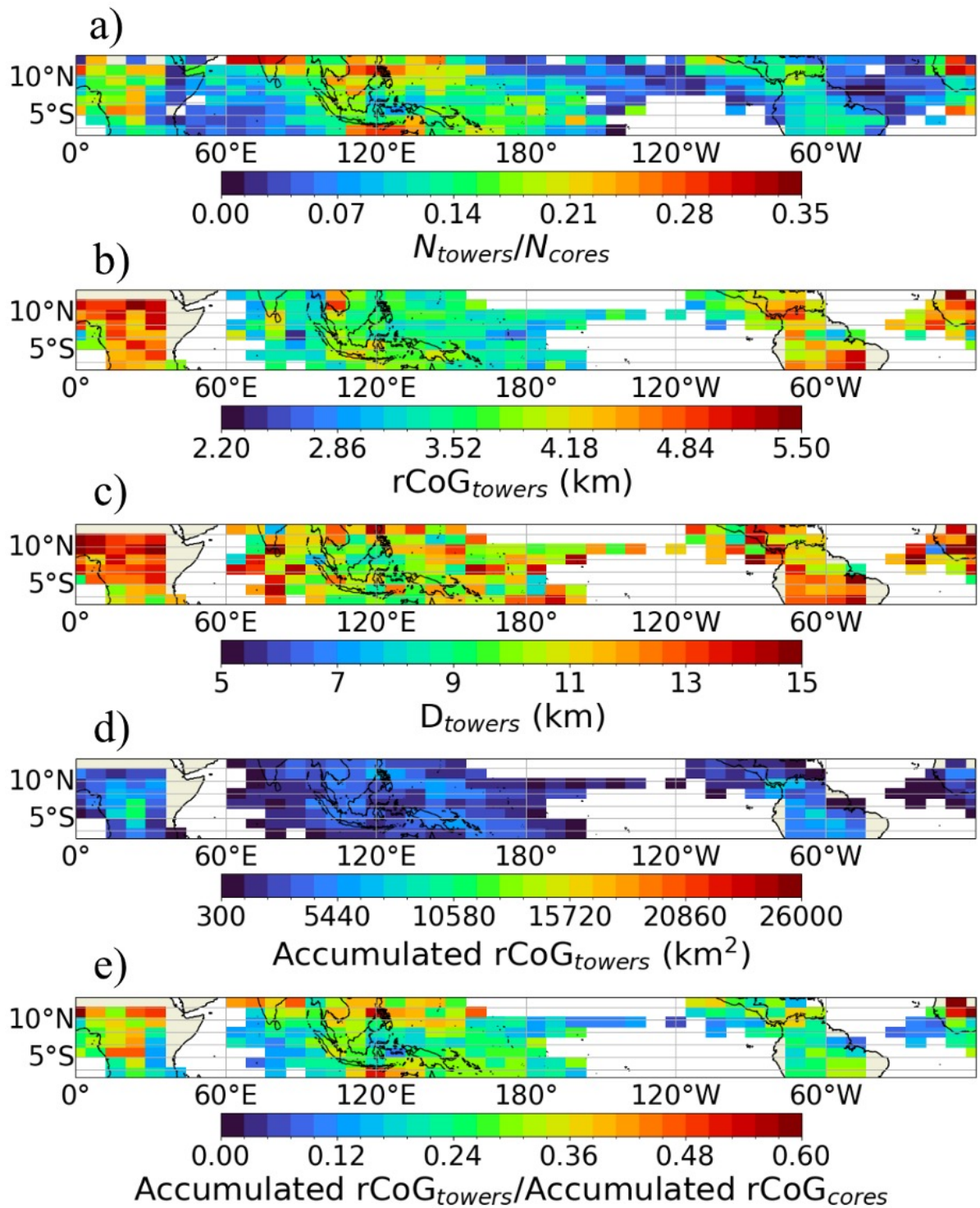
FIGURE 4.4: (a) *hot tower* counts divided by counts of all cores, (b-d) Like Figure 4.3b-d but for *hot towers*, and (e) accumulated rCoG of *hot towers* divided by accumulated rCoG of all deep convective cores. At least 20 *hot towers* have to be included within the $8° \times 4°$ grid boxes for the mean or fraction to be calculated.
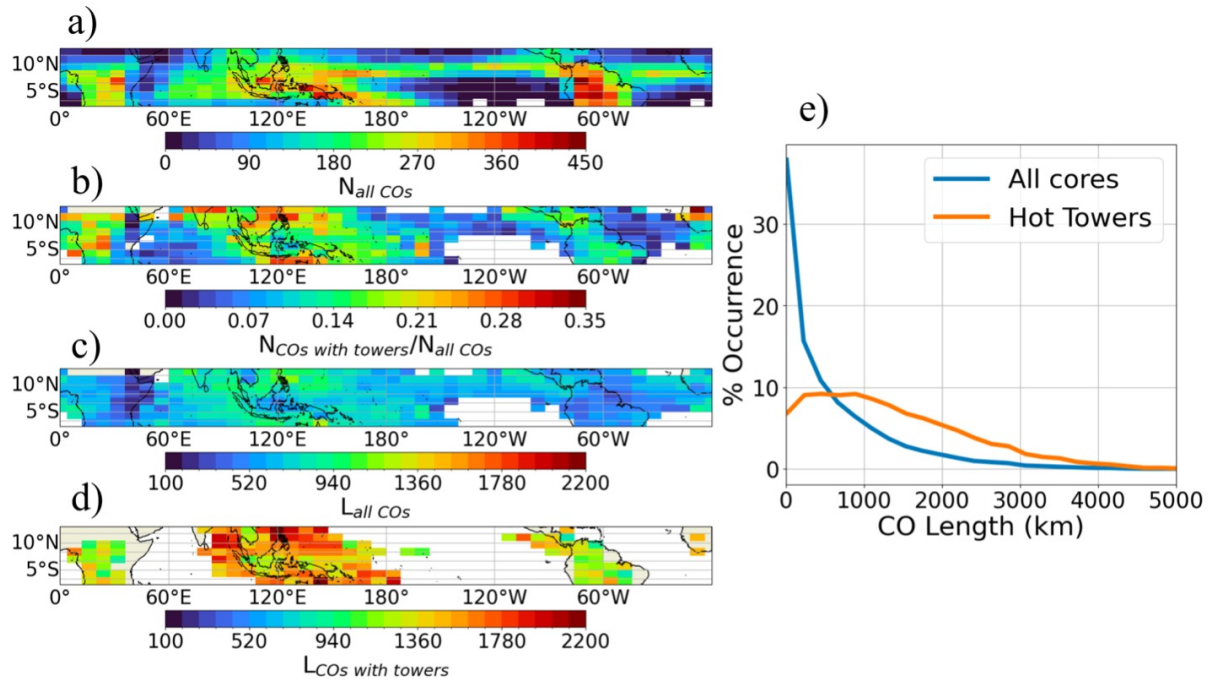
FIGURE 4.5: (a) Counts of all convective objects (COs), (b) Ratio of counts of COs that contain *hot towers* to counts of all COs, (c) mean CO length and (d) mean length of COs that contain *hot towers*. At least 20 cores or *hot towers* are required in each grid box for a mean to be calculated. (e) PDF showing the frequency of convective object length sorted by systems that contain (blue) either *hot towers* or deep convective cores or (orange) must contain at least one *hot towers*.

that has noted that the highest precipitation accumulation over the ocean is attributed to the frequency of convection (Hamada et al., 2015).

4.3.2 Spatiotemporal variability of convective activity within the TTZ

RM58 do not discuss how spatiotemporal variability of deep convection could influence the estimate. As mentioned in previous literature and from the characteristics outlined above, convective behavior varies regionally. We define three dominant regimes of convective activity that are loosely based on regions defined in Williams and Stanfill (2002) and
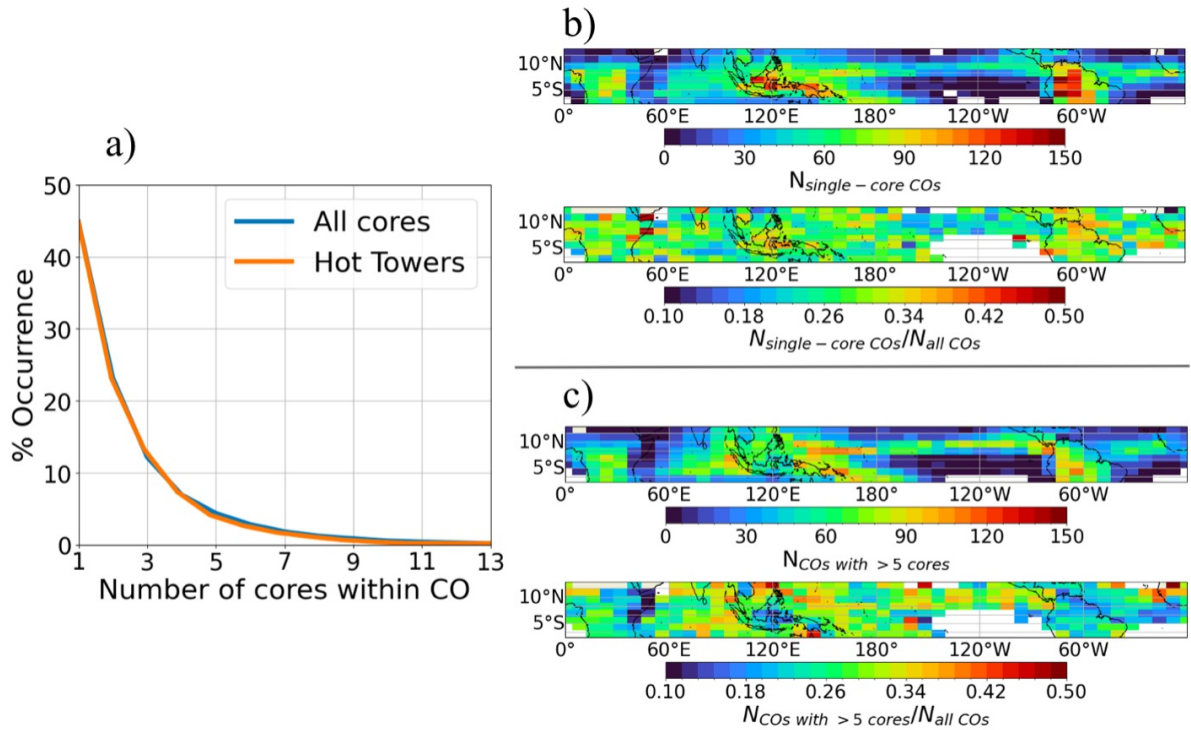
FIGURE 4.6: (a) Percent occurrence of the number of cores within convective objects sorted by systems that contain (blue) either *hot towers* or deep convective cores or (orange) must contain at least one *hot towers*. (b) Distributions of (top) the number of convective objects with one core and (bottom) single-core convective objects divided by number of all convective objects (Figure 4.5a). (c) Distributions of (top) the number of convective objects with more than five cores and (bottom) convective objects with more than five cores divided by Figure 4.5a.

elaborated upon in Stephens et al. (submitted):

1. Continental land in which convection is driven by several factors such as orography, land heterogeneity (e.g., rainforest, desert, etc.), and the diurnal and seasonal variability in surface heating from solar insolation;

2. ITCZ ocean consisting of the East Pacific, South Pacific, Central Pacific, and Atlantic Oceans that are driven by sea surface temperature gradients and moisture convergence in the low-levels; and

3. Maritime Continent that includes the Indian and West Pacific Oceans in addition to land. Convection is often concentrated over the West Pacific Ocean due to anomalously warm sea surface temperatures compared to other parts of the ocean. The islands have their own complex terrain that, in addition to the land-sea-breeze circulations generated, influence convection unlike anywhere else within the TTZ.

The full distribution of convective core and *hot tower* activity within these three regimes are shown in Supplemental Figure A.1. *Hot towers* contribute 5%, 7%, and 15% to the full convective activity over continental land, ITCZ ocean, and the Maritime Continent, respectively.

Figure 4.7 shows the distribution in monthly (a) total core and (b) *hot tower* counts, mean intensity, and accumulated rCoG between 2007-2016 within the different regions. The seasonal cycle in convective core frequency is bimodal across all regions, with peaks in convective core frequency doubling the minima. The peaks occur in May and October for the ocean and Maritime Continent. Over land, the peak in core frequency occurs during October with a second maximum in April. Monthly mean rCoG decreases and plateaus for the remainder of the year over the ocean and Maritime Continent, but is bimodal over land and maximizes in September. Because both core frequency and intensity exhibit a seasonal variability, while convective core size does not (not shown), there is a bimodal distribution in the accumulated rCoG. Thus, it is expected that the most mass that reaches the upper troposphere from all convective cores peaks in May and October over

all ocean and the Maritime Continent, and primarily in October with a secondary peak in April over land.

hot tower counts do not have a bimodal seasonal cycle over the ITCZ ocean and Maritime Continent. Over the Maritime Continent, *hot towers* are consistently the most prevalent between June to December compared to other times of year. The seasonality of *hot tower* occurrence over the full ocean is primarily tracking behavior over the Indian and West Pacific Oceans due to the tendency for *hot towers* to occur in these oceans as opposed to over the ITCZ ocean (see Figure 4.4). The annual cycle in mean rCoG for *hot towers* is consistent with that of all cores between January to May over the ocean and Maritime Continent.The cycle in mean rCoG over land cannot be unambiguously determined since there are fewer than 100 *hot towers* for all months except October. Interestingly, the total mass flux from *hot towers* over the full ocean does not vary significantly between June to November due to the combined increase and decrease in mass flux over the Maritime Continent Oceans and ITCZ ocean, respectively. Meanwhile, *hot towers* over the land maintain the seasonal cycle in mass flux that is reflected in all deep convective cores over land.

Figure 4.7c shows the monthly mean rain rates and OLR averaged over the full TTZ. Over the course of a year the range in monthly mean rain rates is 0.02 mm h^{-1}. The most rain is produced at the same time of year as when the most numerous and intense convective cores occur. Mean OLR varies by 4.5 W m^{-2} over the course of the year and has a unimodal cycle. Despite rain rates remaining nearly constant (and reaching a local
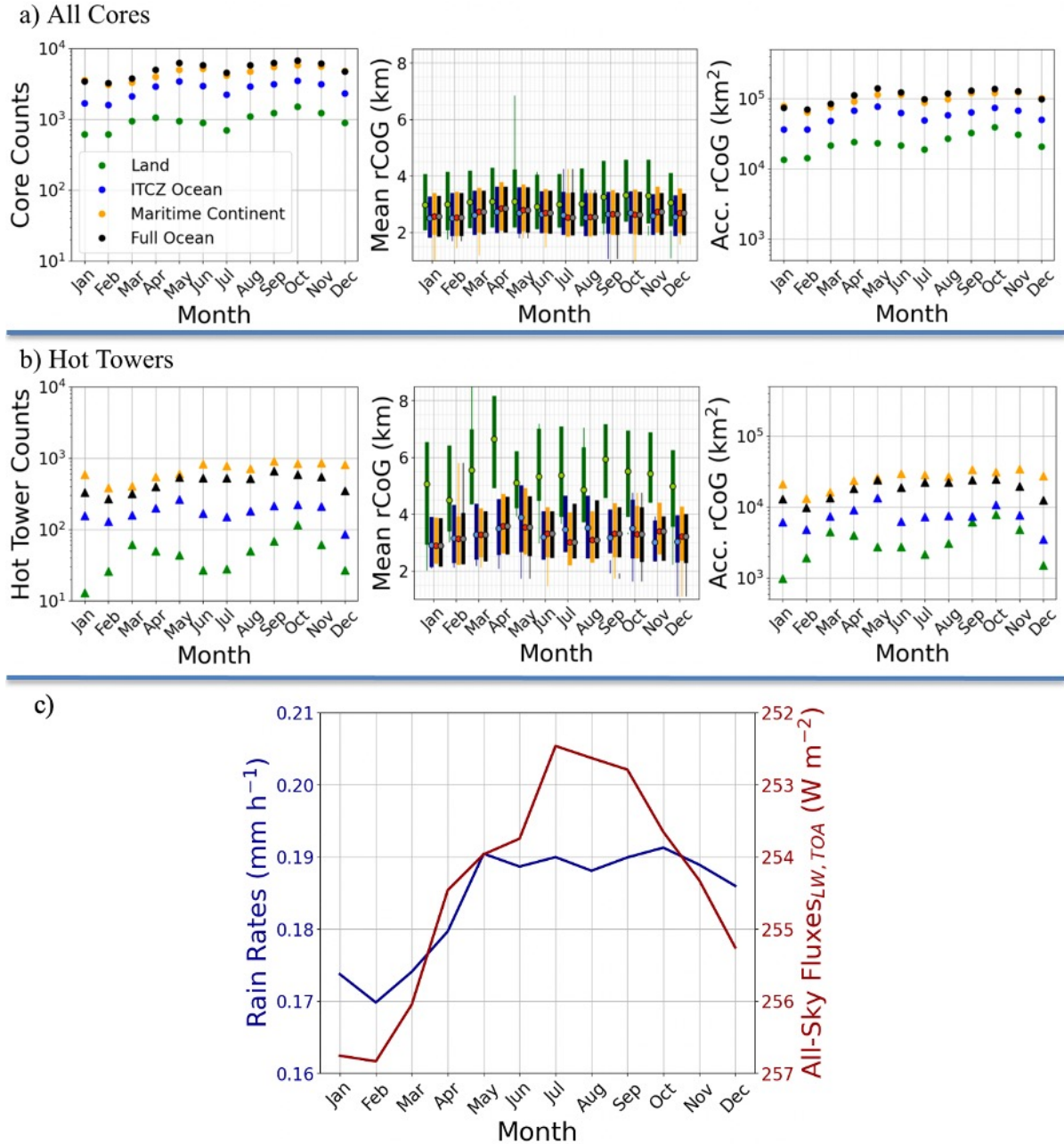
FIGURE 4.7: Monthly CloudSat-detected core (a) and *hot tower* (b) counts (left column), rCoG (middle column), and accumulated rCoG (core counts × mean rCoG × mean size; right column) sorted by land (green), ocean (blue), the Maritime Continent (orange), and the full ocean (black) between January 2007 - December 2010 and January 2012 - December 2016. Full Ocean is the ITCZ ocean plus the Indian and West Pacific Oceans. The rCoG figures show the distribution of the 25% to 75% rCoG values with the dots representing the monthly mean rCoG. (c) Monthly mean CERES EBAF all-sky TOA LW fluxes (dark red) and GPM IMERG rain rates (dark blue) averaged between January 2007 - December 2010 and January 2012 - December 2016 over the full TTZ.

minimum) between May to October, mean OLR reaches a minimum during that time suggesting that clouds deepen during July through September. This could be capturing tropospheric expansion during the boreal summer months. However, this large-scale deepening of clouds is not observed in the annual cycle of individual core rCoG likely because rCoG considers the hydrometeor extent relative to the freezing level. Therefore, the annual cycle of CoG (i.e., including freezing level height) might capture how the height of the freezing level changes over the course of the year. For a more detailed look at the spatiotemporal variability between convective core, high cloud, and precipitation activity, refer to the 10-year time series in Figure S2 and seasonal maps in Figure S3.

4.3.3   How many *hot towers* occur at any given time?

With these geographic and temporal variations in convective activity in mind, we can update the RM58 and RS79 estimates of how many *hot towers* occur at any given time in the TTZ. In particular, we want to capture how the estimate might change over the course of a day. Because it is not possible to estimate how many hot towers occur at any given time solely using A-Train observations given its limited spatial and temporal resolution, we leverage the spatiotemporal resolution of geostationary satellite observations. To do so, Aqua MODIS 11-micron brightness temperatures are co-located to hot tower coordinates. Figure 4.8a shows the BT distribution for all hot towers and deep convective cores identified by CloudSat. The peak BT for hot towers occurs at 195 K, and BTs are slightly lower for higher hot tower cloud top heights (Figure 4.8b). A BT

threshold of 208 K has commonly been used to identify regions of deep convective precipitation using geostationary satellite data (e.g. Mapes and Houze, 1993; Rickenbach, 1999; Williams and Houze, 1987). The present analysis considers exclusively cores that reach the tropopause, and it has been found across multiple reanalysis datasets that the tropical tropopause temperature is less than 195 K (Tegtmeier et al., 2020). Cores that overshoot the tropopause can have brightness temperatures nearing 190 K (e.g. Fiolleau and Roca, 2013).

As shown in Figure 4.8, there is a 45 K range for 90% of hot towers with 70% of hot towers having BTs less than 208 K. However, the BTs of all deep convective cores peak at 210 K, which makes it challenging to adequately define a BT threshold that captures a majority of the deepest core (*hot tower*) activity without including potential information from non-*hot tower*. As a workaround, the probability for detecting a *hot tower* versus a non-*hot tower* is calculated for 5-K BT ranges up to 205 K (i.e., < 195 K, 195-200 K, and 200-205 K), which makes up 62% of the *hot tower* detected. We reason that BTs above 205 K are no longer representative of updrafts that reach the tropopause. The probability of detecting a *hot tower* at any binned BT is given by the red curve in Figure 4.8a. For example, the probability that a BT less than 195 K corresponds to a *hot tower* is 74%, whereas the probability that a BT equal to 205 K corresponds to a *hot tower* is only 15%.

Next, the fraction of the TTZ that contains BTs within each 5-K range at every hour of the day is calculated using the GPM_MERGIR 4 km 11-micron brightness temperature
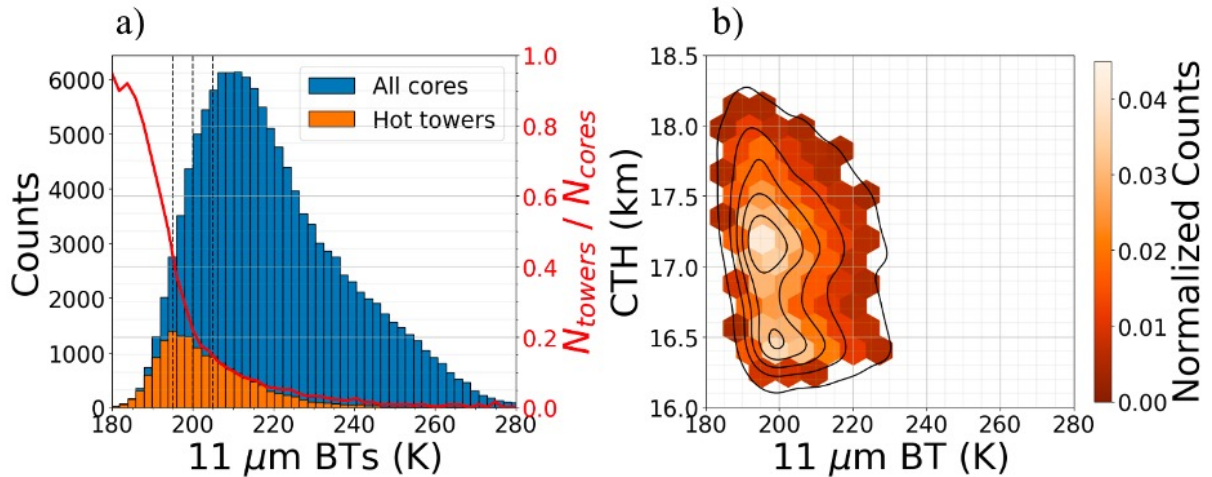
FIGURE 4.8: (a) All core (blue) and *hot tower* (orange) counts binned by their mean core 11-micron brightness temperatures (BTs) from Aqua MODIS. The red curve represents the number of *hot towers* divided by the number of all cores in each BT bin, as shown by the y-axis on the right. Black dashed lines are BT intervals: 195 K, 200 K, and 205 K. (b) Distribution showing the relationship between the *hot tower* cloud top height (y-axis) from CloudSat-CALIPSO and MODIS 11-micron brightness temperatures (x-axis). The innermost line contour corresponds to 10% of the data and each contour is an additional 20% of the data. The shaded hexbins present another distribution perspective. Each hexbin contains a *hot tower* count that is divided by the total *hot tower* count.

data averaged over 2013, as shown in Figure 4.9a. This method assumes that BTs from Aqua Modis reasonably match the GPM_MERGIR data. Figure 4.9a shows that BTs < 195 K cover between 0.03% to 0.075% of the TTZ over the course of a day, with each percentage doubling with an increase in 5 K. BTs < 205 K represent nearly 0.6% of the TTZ. These percentages are comparable to the RM58 estimate that hot towers represent nearly 0.1% of the activity in the TTZ.

We then consider the probability that a given event within each BT range is a hot tower to define a probabilistic fraction of the TTZ comprising hot towers using the equation:

$$F_{TTZ,hottower} = F_{TTZ,BT<195}P_{BT<195,hottower} + F_{TTZ,195<BT<200}P_{195<BT<200,hottower}$$

$$+F_{TTZ,200<TTZ<205}P_{200<TTZ<205,hottower} \quad (4.1)$$

where F is the fraction of the TTZ and P is the probability of a hot tower (given by the ratio of *hot towers* to non-*hot towers*; red curve in Figure 4.8a) for a given brightness temperature range. The surface area of the TTZ is calculated and multiplied by $F_{TTZ,hottower}$, or the probabilistic fraction of the TTZ containing *hot towers*, to estimate the surface area of the TTZ covered by *hot towers*.

Finally, the mean *hot tower* diameter, which is 11.4 km, is used to calculate the surface area of an individual *hot tower*. Dividing the surface area of the TTZ containing *hot towers* by the surface area of an individual *hot tower* provides an estimate for how many *hot towers* occur over the full diurnal cycle (Figure 4.9b). Across the full TTZ, it is estimated that there are 1200-2300 *hot towers* with the minimum occurring at noon LST and the maximum at 0430 LST. The A-Train captures the onset of peak *hot tower* activity during its 0130 LST observing period; however, *hot tower* activity is at a near minimum during 1330 LST.

We also estimate the *hot towers* within each region (i.e., land, ITCZ ocean, Maritime Continent, and full ocean) following this methodology using the mean *hot tower* diameters given in Table 4.1. Figure 4.9b shows that the peak at 0430 LST is largely from *hot towers*
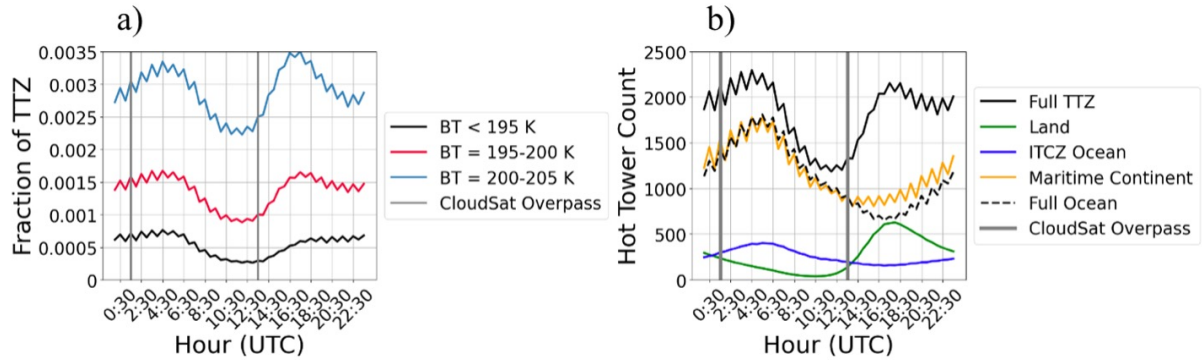
FIGURE 4.9: (a) Diurnal cycle of *hot tower* fractions defined by BT < 195 K (black), BT = 195-200 K (red), and BT = 200-205 K (blue) over the TTZ averaged over 2013 and (b) estimated hot tower count over the diurnal cycle separated by the full TTZ (black), land (green), ITCZ ocean (blue), the Maritime Continent (orange), and the full ocean (dashed black). The vertical grey lines represent the times of CloudSat flyovers.

TABLE 4.1: Mean *hot tower* length within each region averaged between 2007 - 2016, excluding 2011.

	Land	*ITCZ Ocean*	*Maritime Continent*	*Full Ocean*	***Full TTZ***
Length (km)	13.3	11.9	10.6	11.4	**11.4**

over the Maritime Continent, Indian Ocean, and West Pacific Warm Pool. Continental *hot tower* counts peak in the afternoon, which supplies the secondary peak in the TTZ-wide count. Supplemental Figure A.4 shows the estimated *hot tower* counts sorted by season, with the most *hot towers* occurring during SON in 2013, followed by MAM, JJA, and finally DJF. Figure A.2, which presents the monthly core and hot tower estimate from solely CloudSat observations, indicates that 2013 might have been an anomalous year of convective activity, as the highest estimated hot tower counts across the 10-year time period occurred around September 2013. Interestingly, these anomalies are not represented in either the IMERG precipitation or CERES OLR data.

4.4 Conclusions

4.4.1 Synthesis

The focus behind this analysis is to provide an observational update on convective core and system characteristics using satellite observations within the tropical trough zone (13°S - 19°N), which is known to be the region where energy is primarily exported to higher latitudes. RM58 and RS79 postulated that convective updrafts reaching the tropopause, or *hot towers*, transport boundary layer air to the upper troposphere that both balance radiative cooling and supply a surplus of energy to be transported laterally. With combined CloudSat and CALIPSO observations, we identify deep convective cores that surpass both the cold point tropopause and lapse rate tropopause heights and document their geographic and temporal frequency. It is found that *hot towers* make up on average 10% of all convective cores but are between 125-150% larger in diameter and more intense than the full distribution of deep convective cores.

We propose that the convective core reflectivity-weighted relative Center of Gravity of multiplied by the core diameter provides a sufficient proxy for the convective mass flux of a convective core. Multiplying this value by the total number of cores in any given area can provide an understanding of the cumulative convective mass flux of a region, or accumulated rCoG. Along the ITCZ band stretching from the West Pacific Warm Pool to the Atlantic Ocean as well as over the South Pacific Convergence Zone, precipitation and high cloud cover are the most productive. Over these regions there is also a large

accumulated rCoG by all convective cores. However, the *hot tower* accumulated rCoG is smaller per grid box over these regions compared to over land. If convective cores that reach the upper troposphere are the primary energy sources for atmospheric meridional energy transport, then the upper tropospheric energy source preferentially occurs over continental land and off-equatorial regions within the Maritime Continent where *hot towers* tend to occur and contribute the largest mass flux. However, if cores that reach the upper troposphere supply sufficient energy as noted by Fierro et al. (2009), then the primary energy sources extend into the West Pacific Warm Pool and South Pacific Convergence Zone. Still, it is particularly surprising that convection across the full ITCZ ocean (i.e., including the East Pacific and Atlantic Oceans) may not contribute as much energy to higher latitudes compared to convection over the aforementioned regions.

Also noted is the apparent seasonal cycle in convective core and *hot tower* frequency and intensity across three distinct regimes within the TTZ: ITCZ ocean, continental land, and the Maritime Continent (including the West Pacific and Indian Oceans). Convective core frequency, and to a lesser extent, intensity, exhibit a bimodal spread that peaks first in April (land) or May (ITCZ ocean and Maritime Continent) and October (all regions). Over the ocean and Maritime Continent where rain rates are the highest, core frequency follows the seasonal cycle of precipitation suggesting that precipitation is more so controlled by the frequency of cores compared to other convective core characteristics such as intensity.

Finally, we provide an updated estimate of how many *hot towers* occur at each hour over

the course of a day using the probability that a given brightness temperature below 205 K is a *hot tower* from geostationary satellite observations averaged during 2013. Our mean *hot tower* estimate of 1200-2300 is similar to the 1600-2400 estimate made by RS79 despite differences in methodologies, in defining the trough region, and in the mean *hot tower* diameter. Because we do not include BT data greater than 205 K, it is possible that the calculated number of *hot towers* is an underestimate. The observed *hot tower* diameter of 11.4 km is over two times larger than the RM58 estimate of 3-5 km. Recent studies using CloudSat data have also reported convective core diameters ranging between 10-14 km (e.g. Derras-Chouk and Luo, submitted; Takahashi and Luo, 2012; Takahashi et al., 2023). Derras-Chouk and Luo (submitted) also provide a hot tower estimate, using instead a convective mass flux approach with geostationary satellite observations. They report 600-800 hot towers at any given time within a 10-degree band, with noticeable differences in counts between DJF and JJA. It is understandable that our estimate is larger than that of Derras-Chouk and Luo (submitted) considering that our estimate is over a larger domain.

4.4.2 Questions remaining within the *hot tower* framework

It remains to be understood whether *hot towers* exist in the way that was first proposed by RM58 and RS79. Whether updraft regions are the sole contributors to supplying energy for lateral transport within the atmosphere has been discussed over the years. More recently, it has been suggested using aquaplanet simulations that the energy exported from humid environments is supplied by the absorption of longwave radiation by clouds

as opposed to solely the distinct updrafts (Needham and Randall, 2021). If this is the case, it could be that the regions that are primarily the most humid and produce the largest cloud cover are the energy source for lateral transport. This occurs primarily over the Maritime Continent and West Pacific Warm Pool where there is a strong coupling between the frequency of convective updrafts, and high cloud and precipitation productivity.

If it is the case that deep convective cores supply the energy for atmospheric meridional transport, it would be worthwhile to understand how much more energy, if at all, convective cores that reach the tropopause contribute compared to those that do not extend into the tropopause. The product of *hot tower* size and intensity is over two times greater than that of cores that do not reach the tropopause; however, they are a lot more infrequent. Is it the case that these *hot towers* supply most of the energy in the upper troposphere compared to the more frequent, but less intense, convective cores? This is the type of question that observations from the INvestigation of Convective UpdraftS (INCUS) and Atmospheric Observing System (AOS) missions combined with simulations from global storm resolving models, will hopefully help address.

Chapter 5

Observational Evidence towards a Weakened Cooling Top-of-Atmosphere Net Cloud Radiative Effect Associated with the Most Intense Convective Systems

5.1 Introduction

The dynamic, thermodynamic, and radiative processes associated with atmospheric deep convection all play a crucial role in influencing the Earth's radiative energy budget, atmospheric circulation, and hydrological cycle. Specifically, tropical deep convective updrafts vertically redistribute energy and transport moisture from the surface to the upper troposphere and, to first order, help regulate mid-latitude temperatures. How intense convective systems become not only governs other storm properties such as cloud and rainfall production, but it also influences the surrounding environment by creating damaging winds and promoting other hazards that influence people's lives and well-being. As convective systems are expected to increase in intensity under future climate scenarios (e.g. Cheng et al., 2022; Diffenbaugh et al., 2013; Singh and O'Gorman, 2015), it is becoming increasingly important to understand how deep convective intensity relates to other storm properties and its influence on the Earth's top-of-atmospheric radiative energy budget (e.g. Harrison et al., 1990; Ramanathan et al., 1989).

Although it is generally accepted that deep convective clouds contribute a near-neutral impact at the top-of-atmosphere (Hartmann et al., 1992; Kiehl and Ramanathan, 1990; Ockert-Bell and Hartmann, 1992; Rossow and Zhang, 1995; Zhang et al., 1995), some speculate that this could be just a coincidence (e.g. Kiehl, 1994) or the result of a feedback that exists to maintain a balance in the net radiation at the top of the atmosphere between the convective and non-convective regions (e.g. Hartmann and Berry, 2017; Hartmann et al., 2001). These conjectures drive the question: given evidence that deep convection

may become more intense in a warming climate, how will changing deep convective cloud properties alter the top-of-atmospheric radiative energy budget?

How deep convective systems change in response to warming sea surface temperatures has been the focus of several studies beginning in the early 1990s (e.g. Hartmann and Larson, 2002; Lindzen et al., 2001; Pierrehumbert, 1995; Ramanathan and Collins, 1991). These studies presented cases for opposing high cloud feedback mechanisms that argued how anvil amount would respond to warming SSTs. Methodological inconsistencies with the Lindzen et al. (2001) "adaptive iris effect", in which it was suggested that cloud droplets would increasingly contribute to precipitation as opposed to detraining into the anvil (i.e., enhanced precipitation efficiency), triggered a debate (e.g. Del Genio and Kovari, 2002; Hartmann and Michelsen, 2002; Lin et al., 2002; Rapp et al., 2005), thus further promoting attention to this topic. Despite the controversy, the importance of relating mass flux within convective updrafts to rainfall, anvil cloud amount, and the associated radiative response was recognized. It has been suggested that a reduction in high cloud cover, possibly associated with increased convective precipitation efficiency (Clement and Soden, 2005; Wielicki et al., 2002) and/or a strengthening of the Hadley Cell (e.g. Chen et al., 2002), resulted in a net gain in the top-of-atmosphere radiative energy budget in the tropics between the mid 1980s to late 1990s (e.g. Wielicki et al., 2002; Wong et al., 2006).

Since then, both modeling and observational studies have posited physical mechanisms for a high cloud shift in response to warming sea surface temperatures (e.g. Bony et al., 2016;

Bretherton et al., 2005; Zelinka and Hartmann, 2010). One mechanism that has garnered significant attention is convective self-aggregation in which, under idealized conditions and particularly over warmer SSTs, clear-sky regions expand and dry, which causes the deep convective region to shrink and systems increasingly cluster. This process moistens and enhances latent heat release within the convective region, thus promoting convective updrafts to deepen, or intensify (e.g. Arnold and Randall, 2015; Bretherton et al., 2005; Coppin and Bony, 2015; Wing and Cronin, 2016; Wing and Emanuel, 2014, and others). Several studies have tried to diagnose whether this mechanism exists in reality using both passive microwave satellite and active radar observations by aggregating pixel-level data over a grid box and assigning indices based on how convective clouds organize, or cluster, on various length and spatial scales (e.g. Brueck et al., 2020; Holloway et al., 2017; Kadoya and Masunaga, 2018; Retsch et al., 2020; Tobin et al., 2013, 2012; Tompkins and Semie, 2017, and others). Both modeling and observational studies suggest that an increased clustering of deep convective clouds has the potential to reduce cloud shortwave cooling and increase longwave radiative cooling to space in the clear-sky regions (Bony et al., 2016; Coppin and Bony, 2015; Saint-Lu et al., 2020; Tobin et al., 2012), a process now referred to as the tropical anvil cloud amount feedback.

Meanwhile, some observational studies have suggested that convective anvils might thin with warming (Höjgård-Olsen et al., 2022; Kubar and Jiang, 2019; Liu et al., 2017). This cloud optical depth feedback (Stephens and Greenwald, 1991; Stephens and Webster, 1981) may influence both longwave and shortwave cloud radiative effects and could be further connected to an overall reduction in anvil cloud extent (Gasparini et al., 2023).

At the same time, another convective cloud feedback mechanism has been proposed independent of the reduction in anvil framework. The tropical high cloud altitude feedback suggests that convection will deepen as sea surface temperatures increase due to troposphere expansion, which may result in a marginal increase in the longwave cloud radiative effect associated with higher convective cloud top heights (Hartmann and Larson, 2002; Zelinka and Hartmann, 2010).

It remains unclear as to whether longwave or shortwave cloud radiative effects respond more strongly to intensifying convection and, therefore, whether the top-of-atmospheric radiative fluxes in the convective region will remain in balance. This is because there is a lack of knowledge in two areas: 1) how convective cloud properties vary with the intensity of the parent convective cores (e.g. Elsaesser et al., 2022; Li and Schumacher, 2011), and 2) how the net radiative response of deep convective systems respond to these changes (Stephens, 2005).

This study seeks to address these issues using a novel storm object-identification framework based on active spaceborne satellite observations. Similar approaches have been demonstrated for connecting anvil vertical and horizontal characteristics to their parent convection (e.g. Bacmeister and Stephens, 2011; Deng et al., 2016; Hu et al., 2021; Igel et al., 2014; Igel and van den Heever, 2015a; Li and Schumacher, 2011; Xu et al., 2016; Yuan and Houze, 2010; Yuan et al., 2011; Zheng et al., 2018, among others). For example, Li and Schumacher (2010) used Tropical Rainfall Measuring Mission (TRMM)

Precipitating Radar (PR) measurements to identify the different anvil properties of active convection based on droplet composition. It was found that convection associated with very thick anvils (i.e., anvil that the TRMM PR can detect) is deeper, stronger, and covers more area than convection with no anvil detected. However, they pointed out that when compared to CloudSat measurements, the PR underestimates both anvil cloud top height and horizontal extent due to its limited 17 dBZ sensitivity. This limitation made it impossible to quantify the radiative impacts of these changes.

CloudSat and Cloud-Aerosol Lidar and Infrared Pathfinder Satellite Observations (CALIPSO) measurements have been particularly useful for studying the vertical structure of deep convective clouds to infer microphysical processes associated with anvil development. Yuan et al. (2011) defined cloud objects identified with CloudSat's Cloud Profiling Radar (CPR) and observed that the anvil formed closest to active raining regions is the thickest region of the anvil and consists of detrained graupel particles that were formed through riming in the updraft regions. The larger particles fall at a quicker rate than smaller particles, which partially explains the anvil thickness. However, smaller particles continue to grow and fall at a slower rate, which explains the narrowing of anvil clouds as their distance, and ultimately lifetime, from the raining core increases. Deng et al. (2016) included CALIPSO Cloud-Aerosol Lidar with Orthogonal Polarization (CALIOP) measurements in their objects to distinguish thin anvil development. They emphasize the complexity of anvil development, noting that the scaling of deep convection, its life stage, intensity, and the large-scale environment are all important factors impacting anvil productivity.

More generally, these studies reveal the need to consider cloud properties on the scale of discrete convective objects to gain insights into the responses of the component cloud elements to environmental changes. This study applies a cloud object analysis framework to examine the deep convective cloud properties and net radiative effects at the root of high cloud amount, optical depth, and altitude feedbacks. Using a CloudSat radar-defined proxy for convective core vertical intensity, the relative magnitudes of LW and SW CRE responses to convective intensity are quantified for contiguous convective objects (CO) identified in combined CloudSat-CALIPSO measurements. Though cloud feedbacks cannot be diagnosed using composites of static satellite snapshots, the analysis provides insights into storm behavior that may shed light on how the radiative effects of tropical convection might respond to future intensification. The next section introduces the convective object database used for this study. Section three presents the distribution of present-day convective cloud radiative effects over the tropical ocean. The following section quantifies their variation with anvil thickness and cloud top height. Then, CO cloud properties and radiative effects are compared between populations of storms that are sorted by their core vertical intensity in the fourth section. The final section discusses the extent to which these results can be used as a benchmark for modeling studies that explore how deep convective cloud properties and their radiative responses might alter under a changing climate.

5.2   Data and Methodology

5.2.1   Identifying Deep Convective Systems with A-Train Measurements

Active convection is identified using CloudSat's 94 GHz nadir-looking Cloud Profiling Radar (CPR) that has a resolution of 1.4 km $\times$ 1.8 km with a vertical resolution of 480 m and oversampled to 240 m (Tanelli et al., 2008). The high spatial resolution and vertical-profiling capabilities make the CPR useful for observing signatures of lofted large hydrometeors within deep convective cores that are typically no more than a few kilometers in diameter (Giangrande et al., 2013; Wang et al., 2020; Yang et al., 2016). The CPR's minimum sensitivity of -28 dBZ further enables it to detect cloud droplets and light precipitation, essential for quantifying the radiative effects of associated cloud cover. However, from a radiative perspective, detrained cirrus is also important to capture. Incorporating measurements from the Cloud–Aerosol Lidar with Orthogonal Polarization (CALIOP) on board CALIPSO captures thin cloud structure that often goes undetected by the CPR (Deng et al., 2016).

Combined data from the CPR and CALIOP are used to distinguish "convective objects" (COs) consisting of radar-detected convective cores with surrounding precipitating or non-precipitating cloud, which differs from the 2B-CLDCLASS-lidar "deep convective cloud" definition that requires that the region is heavily raining with possible hail (Sassen et al., 2008). Details of this object-identification algorithm are described in

Pilewskie and L'Ecuyer (2022) (hereafter, PL22). Convective flags from the CloudSat 2C-PRECIP-COLUMN (2CPC) "Conv_strat_flag" variable are first identified along a CloudSat overpass under the condition that the CPR signal is attenuated at least one kilometer above the freezing level. Contiguous convective flags are grouped and defined as convective cores. Cloud top and base heights found in the 2B-CLDCLASS-lidar product are derived from CALIOP measurements to fill in cloud missed by the CPR. Adjacent profiles along the CloudSat track that contain either pixels corresponding to a reflectivity value greater than -28 dBZ or have CALIOP-detected cloud cloud connect to the convective cores and complete the CO. Constraints introduced in PL22 for discerning active convection globally are also adopted in this analysis: 1) COs need to contain at least 2% convective precipitation compared to the area of non-convective precipitation and 2) COs are at least 9 km (five profiles) long to limit the likelihood that CloudSat only samples the edge of a convective system.

It is quite common for observed convective objects to have multiple deep convective cores connected by anvil and detrained cirrus. Because it is not possible to determine whether these systems are organized by the same physical processes, we distinguish systems that consist of either a single observed cell or multiple cells in the analysis. A convective object with one cell follows the conceptual model of a convective system with a single precipitating region that may or may not have non-precipitating anvil development. If a convective object has more than one identified convective core, it is considered unicellular if the cores are embedded in a single precipitating region (i.e., no more than two non-precipitating flags are observed between cores). This definition is comparable to the geometric-based

definitions of a "pedestal" (Igel et al., 2014) or "convective pillar" (Hu et al., 2021) in that the bulk of upward mass transport occurs in this region. Systems with multiple cores separated by at least two non-precipitating CloudSat fields of view are considered multicellular. We are unable to distinguish organized multicellular systems from those that arise from the merging of distinct systems using solely A-Train observations. This may be possible by coupling to geostationary observations that scan a larger, two-dimensional horizontal extent and provide temporal context, but establishing a consistent definition of convective objects from these two distinct perspectives is far from trivial and beyond the scope of the present work.

5.2.2   Defining "Convective Intensity" in the Tropics

Many studies have defined tropical deep convective intensity based on the vertical velocity of individual updrafts or cores (e.g. Doswell, 2001; Zipser et al., 2006). Large updraft velocities loft hydrometeors high into the atmosphere, which contributes to the full convective system deepening. Outside of field campaigns, it is challenging to make instantaneous measurements of vertical velocities within updrafts that are on a kilometer-scale (Giangrande et al., 2013; Wang et al., 2020). Thus, indirect proxies of convective intensity have been employed across multiple scales. Some satellite-based studies have used precipitation-based proxies for intensity, such as the radar echo top height or rainfall accumulation (e.g. Hamada et al., 2015; Liu and Zipser, 2013, 2005; Liu and Zipser, 2008; Liu et al., 2008b; Takahashi and Luo, 2014; Zipser et al., 2006). Studies focused on climate change scenarios require an understanding of how systems will change on large

spatiotemporal scales. Monthly mean ascent values have been used to bin regions dynamically according to bulk convective activity (e.g. Bony et al., 2004; Bony et al., 1997) given that, to a first order, the large-scale mean ascent corresponds to an average of the mass flux in individual convective clouds (Emanuel, 1994).

Because this study is highlighting convective properties on a cloud scale, we employ a proxy for convective intensity that is directly representative of the hydrometeor distribution resulting from individual updrafts. Reflectivity measurements within each profile of an identified convective core are used to calculate its Center of Gravity (CoG) following the method outlined in Storer et al. (2014) and subsequently in PL22. This value corresponds to the height at which the bulk hydrometeor mass is transported into the troposphere. The height of the mean freezing level is subtracted from the CoG to define the relative CoG (rCoG) to capture how efficiently mass is transported into the upper atmosphere (PL22).

5.2.3   Categorizing the Convective Objects

We categorize convective systems based on the cloud top height, whether underlying low-level cloud is present, and at what time of day the systems occur, which all factor into their radiative effects. For a system to be included in this analysis, its mean convective core rCoG must be at least 1 km above the freezing level. A mean 8 km cloud top height is used as a threshold to determine if a CO is in a cumulus mode (CTH < 8 km) or a deep convection mode (CTH >= 8 km). Table 5.1 shows that only 4% of the full database belongs to the congestus mode due to the rCoG height requirement. Nearly half of the

TABLE 5.1: Number of convective objects observed over the tropical ocean sorted by convective type, time of day, and CloudSat mission eras.

Total COs	Congestus		Deep Convection			
51273	2178 (4%)		49095 (96%)			
			Ice-only		Underlying liquid	
			25605 (50%)		23490 (46%)	
	Single	Multi	Single	Multi	Single	Multi
1330 LT (2006-2011)	530	133	5067	3638	2834	4807
17009 (33%)	(1.0%)	(0.2%)	(10%)	(7%)	(6%)	(9%)
0130 LT (2006-2011)	663	176	5225	2818	2867	5366
17115 (33%)	(1.3%)	(0.3%)	(10%)	(5%)	(6%)	(10%)
1330 LT (2012-2016)	525	151	4999	3858	2845	4771
17149 (34%)	(1.0%)	(0.3%)	(10%)	(8%)	(6%)	(9%)

COs in the deep convective mode contain liquid cloud underlying the anvil, which has the potential to enhance the SW CRE of a CO compared to a CO with no underlying cloud. Therefore, the fraction of underlying cloud within each deep CO (hereafter, F_{liquid}) is calculated to further partition COs into "ice-only" ($F_{liquid} <= 0.1$) or with "underlying cloud" ($F_{liquid} > 0.1$). The low cloud extent is at most 50% of the CO length for 95% of the COs that contain low cloud. Note that the multi-cell "ice-only" CO in Figure 5.1 contains low-level cloud between -2.5 to -3.5 °N and 1 to 1.5 °N. It is categorized as such because the low cloud reflectivity profiles are connected to the deep convective system.

Because deep convective objects are required to have cores with a cloud top height above 8 kilometers, they are deemed as "active" convective cases that span the life stages between
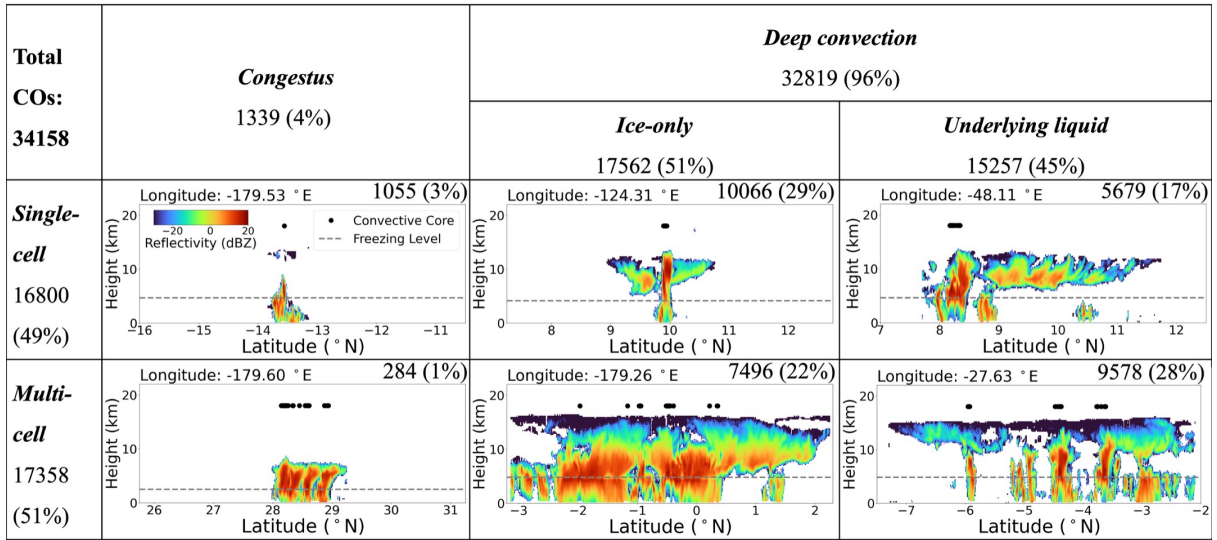
FIGURE 5.1: Diagram presenting the sampling for each convective object type based on if they are single- or multi-celled (rows) and congestus or deep convection (columns). Deep convection is partitioned into ice-only or containing underlying liquid. A reflectivity profile case with the deep convective cores (black dots) and mean freezing level (black dashed line) is presented for each convective object type. The numbers pertain to convective objects observed at 1330 LT between 2006-2016.

developing to mature. Table 5.1 shows that there are 51,273 total active convective objects within the database that fit the criteria outlined. The sampling of single- and multi-cell systems is nearly equal; however, ice-only COs more frequently contain only one cell, while systems containing low-level cloud often have multiple precipitating cells. The time of day at which a convective object is observed is also important to consider since there is no solar illumination at 0130 LT. Since the SW CRE is zero for COs observed during this time, they contribute a warming impact at TOA by their greenhouse effect. Differences in total CO sampling as well as the sampling for each convective type between the two time periods are negligible for the 2006-2011 period (Table 5.1). Only daytime convective objects are stored in the database for 2012-2016 due to CloudSat's transition to daytime-only operations starting in 2012, otherwise known as the DO-Op period.

5.2.4   Top of Atmosphere Cloud Radiative Effects

This study uses the most recently released Revision 05 Product 2 (R05 P2) 2B-FLXHR-lidar data, which is available from the CloudSat data processing center (`https://www.cloudsat.cira.colostate.edu/data-products/2b-flxhr-lidar`). Vertical profiles of shortwave and longwave radiative fluxes are derived from estimates of broadband fluxes that are consistent with CloudSat, CALIPSO, and MODIS retrievals of atmospheric, cloud, and surface properties (Henderson et al., 2013; L'Ecuyer et al., 2008). Matus and L'Ecuyer (2017) related radiative fluxes from this data product to CERES output and found that the monthly mean 2.5-degree root-mean-square differences for SW fluxes is 13.8 W m^{-2} and 5.9 W m^{-2} for LW fluxes. The R05 version uses the CloudSat 2C-ICE product (Deng et al., 2013, 2010) to capture cirrus cloud properties (Hinkelman and Marchand, 2020), with the updated P2 version of R05 now containing radiative fluxes calculated for the DO-Op period and fills in gaps where data was previously missing in older product versions (Henderson and L'Ecuyer, 2023).

The top-of-atmosphere shortwave, longwave, and net cloud radiative effects are calculated for each profile within a convective object and averaged over it using the equations:

$$< CRE_{LW,TOA} >= [(F_{down} - F_{up})_{all-sky} - (F_{down} - F_{up})_{clear-sky}]_{LW,TOA}, \qquad (5.1a)$$

$$< CRE_{SW,TOA} >= [(F_{down} - F_{up})_{all-sky} - (F_{down} - F_{up})_{clear-sky}]_{SW,TOA}, \qquad (5.1b)$$

$$< CRE_{Net,TOA} >=< CRE_{LW,TOA} > + < CRE_{SW,TOA} >, \qquad (5.1c)$$

with F_{down} and F_{up} corresponding to the downward and upward fluxes in all-sky and clear-sky conditions (Hartmann et al., 1986; Henderson et al., 2013; Oreopoulos and Rossow, 2011; Ramanathan et al., 1989). Under the assumption that the observed storms could exist at any time of day given the weak diurnal cycle over the ocean (Liu and Zipser, 2008; Nesbitt and Zipser, 2003), $< CRE_{SW,TOA} >$ values are normalized by the diurnally averaged insolation (hereafter, $< \widehat{CRE}_{SW,TOA} >$) to extrapolate the limited CloudSat sampling to all times of day (L'Ecuyer et al., 2019; Matus and L'Ecuyer, 2017).

5.3   The Radiative Impact of Tropical Oceanic Convection

It is well-understood that convective clouds provide a near-zero net cloud radiative effect at the top of the atmosphere due to their shortwave and longwave cloud radiative effects nearly cancelling. We verify this by calculating the total contribution of convective systems to the total top-of-atmosphere cloud radiative effect modified from L'Ecuyer et al. (2019), which consider the temporal frequency and length scales of convective systems within $8° \times 4°$ grid boxes (Figure 5.2):

$$CRE_{LW,TOA} = \frac{\Sigma < CRE_{LW,TOA,Day} > L_{CO,Day} + \Sigma < CRE_{LW,TOA,Night} > L_{CO,Night}}{(N_{Overpasses,Day} + N_{Overpasses,Night})L_{gridbox\ latitude}},$$

$$(5.2a)$$

$$CRE_{SW,TOA} = \frac{\Sigma < CRE_{SW,TOA} > L_{CO,Day}}{N_{Overpasses,Day} L_{gridbox\ latitude}}, \tag{5.2b}$$

$$CRE_{Net,TOA} = CRE_{LW,TOA} + CRE_{SW,TOA}, \tag{5.2c}$$

where $N_{overpasses}$ are the number CloudSat overpasses. Convective cloud contributions to the total cloud radiative effect consider the spatial distribution of each CO by applying the length scale of a convective object (L_{CO}) to the numerator and the latitudinal length of a grid box ($L_{gridbox\ latitude} \sim 222$ km) to the denominator. This ensures that cases where COs might be small (large) but have a large (small) CRE are appropriately offset by considering where CRE is zero in surrounding regions. Figures 5.2c-d demonstrate that the peak magnitudes of both LW and SW CRE at TOA occur in the regions where convection is most prominent and not necessarily where the mean CO length is the largest. Convective objects contribute a mean diurnally-corrected TOA SW CRE of -15.8 W m^{-2}, which is offset by a mean TOA LW CRE of 11.0 W m^{-2} to produce a mean TOA net CRE of -5.3 W m^{-2}. Multiplying this value by the analytical estimate that the tropical ocean makes up 37% of the Earth results in the net impact of tropical oceanic convection being -2.0 W m^{-2} on the global radiation budget. Despite the small mean net radiative contribution by convective objects, the contributions do vary significantly by region. Systems that have the strongest cooling impact nearing -20 W m^{-2} occur in the Indian Ocean, surrounding the Maritime Continent, and in the East and Central Pacific Ocean. Signatures of slight warming on the order of 1-2 W m^{-2} are over the West Pacific
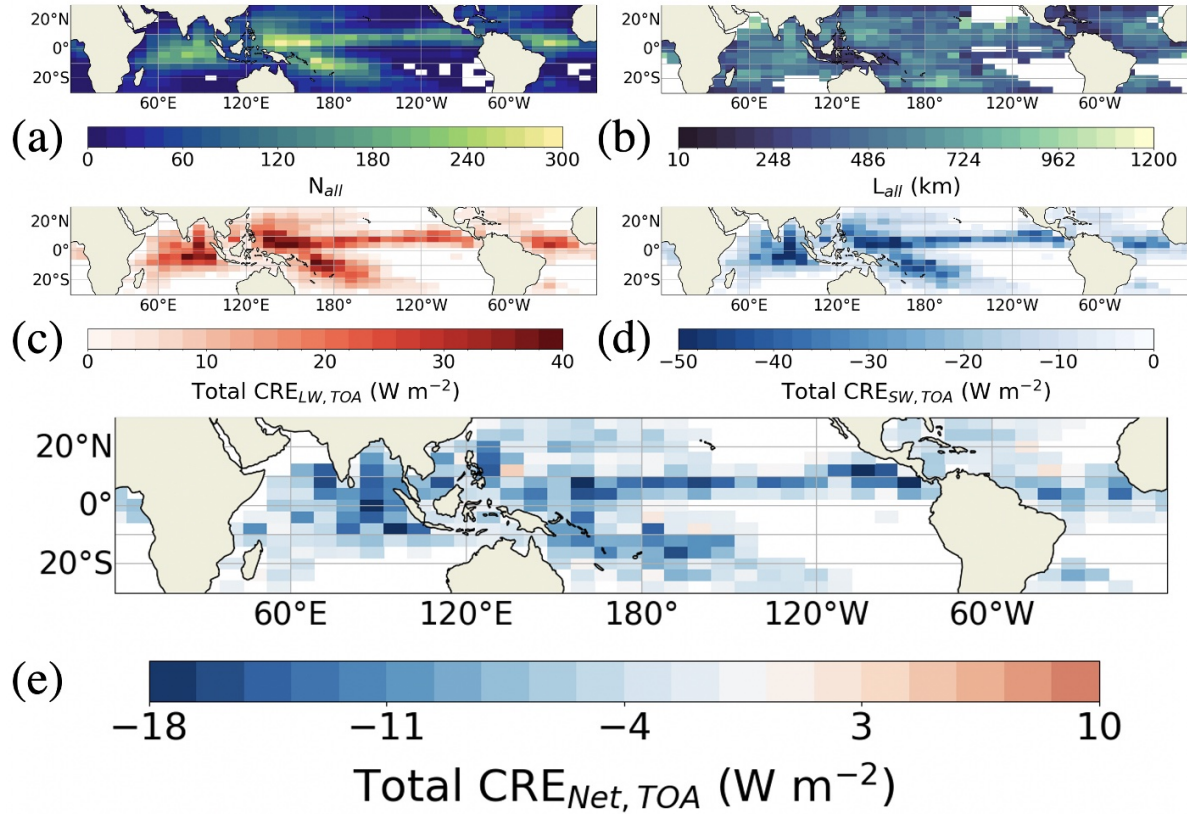
FIGURE 5.2: a) Convective object count (N_{all}), b) mean convective object length (L_{CO}) within grid boxes containing at least 10 COs, convective object contributions to the total c) day and night TOA LW CRE, d) diurnally-corrected TOA SW CRE, and e) TOA net CRE within $8° × 4°$ grid boxes between August 2006 - March 2011.

Warm Pool, South Pacific Ocean, and Atlantic Ocean.

Figures 5.3 and 5.4 show the single- and multi-cell CO distribution and radiative contributions separately. Figures 5.3e and 5.4e indicate that single-cell COs contribute less to the total CRE than multi-cell COs because they have a length scale nearly four times smaller, on average, than multi-cell COs (i.e., L_{single} is 200 km compared to 730 km for L_{multi}). The mean net CRE at TOA of single-cell systems is -1.7 W m^{-2} with a net global radiative impact of -0.6 W m^{-2}, compared to the mean net CRE and net global radiative impact of -4.2 W m^{-2} and -1.6 W m^{-2}, respectively, for multi-cell systems.
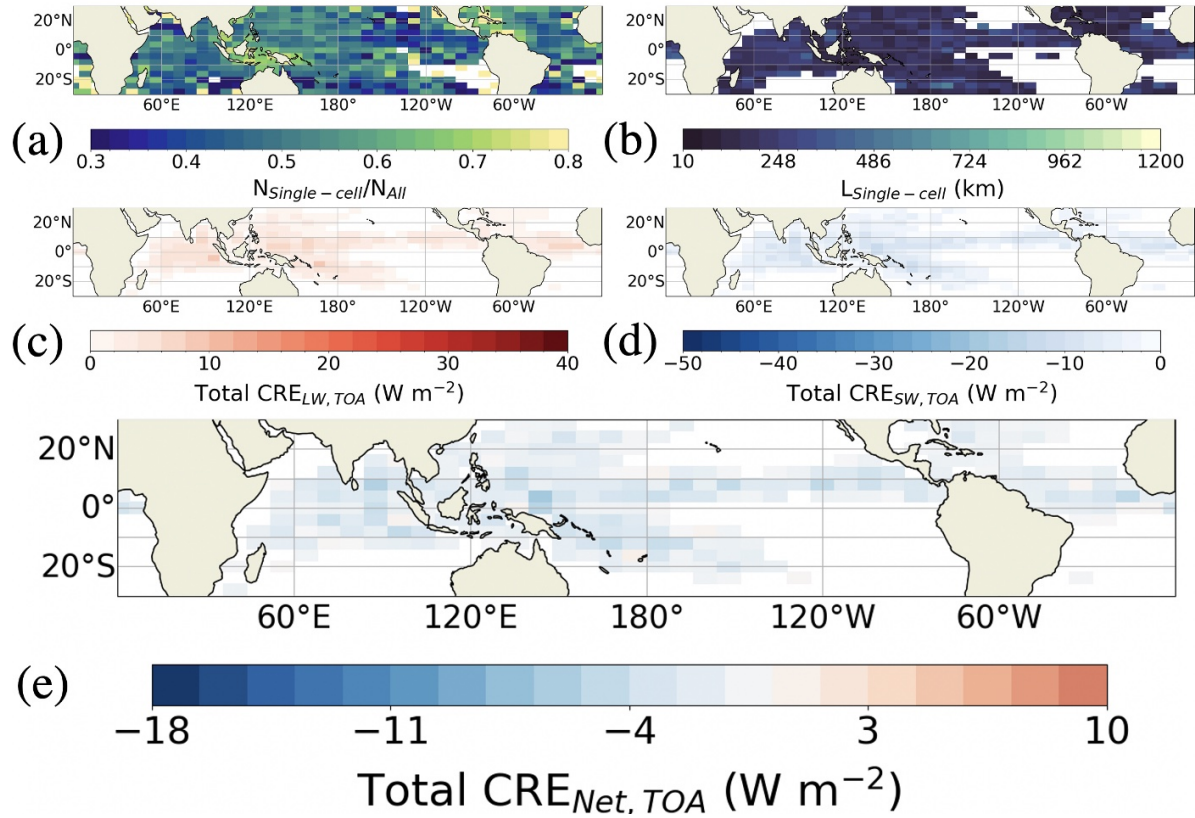
FIGURE 5.3: a) Fraction of single-cell CO counts to counts of all COs, b-e) like Figure 5.2b-e but for single-cell convection.

Table 5.2 presents the conditional mean top-of-atmosphere cloud radiative effects of convective objects calculated from Equation 5.1. The radiative contributions by individual convective objects are nearly two orders of magnitude larger than their total contribution to the global radiative energy budget that considers their spatiotemporal frequency. Furthermore, Table 2 verifies large individual $< CRE_{LW,TOA} >$ and $< \widehat{CRE}_{SW,TOA} >$ values that, when added together, produce a smaller net CRE at TOA. On an individual storm basis, single-cell COs have a 17.9 W m^{-2} greater cooling impact than multi-cell COs.

It is worth noting that, on average, daytime single- and multi-cell systems contribute 8.2
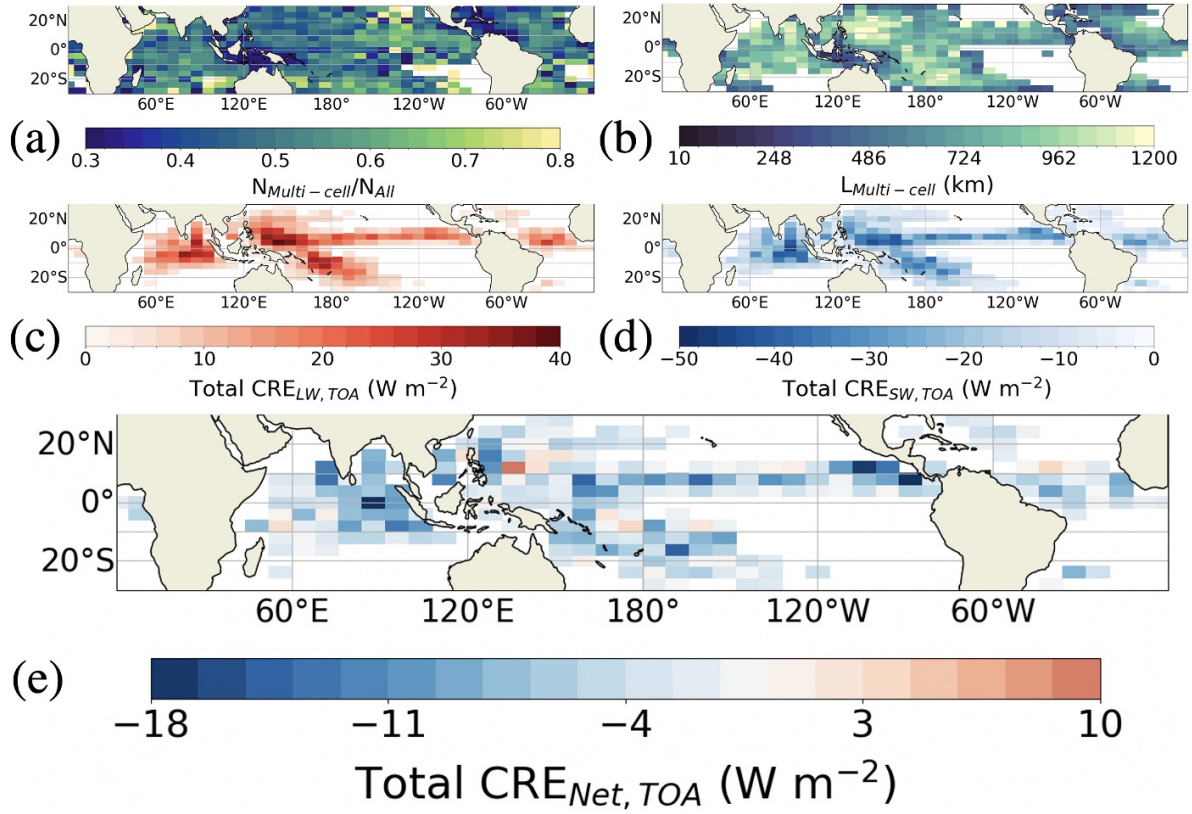
FIGURE 5.4: Like Figure 5.3 but for multi-cell convection.

TABLE 5.2: Tropics-wide conditional mean TOA CRE values for all, single-cell, and multi-cell COs for daytime overpasses between August 2006 - December 2016 (excluding April - December 2011). Also included is the conditional mean LW CRE for nighttime overpasses between August 2006 - March 2011.

	$< CRE_{LW,TOA} >$		$< \widehat{CRE}_{SW,TOA} >$	$< CRE_{Net,TOA} >$
	Day	**Night**		
All COs	105.4	93.9	-161.2	-61.5
Single-cell	97.6	89.4	-163.9	-70.5
Multi-cell	113.1	98.6	-158.5	-52.6
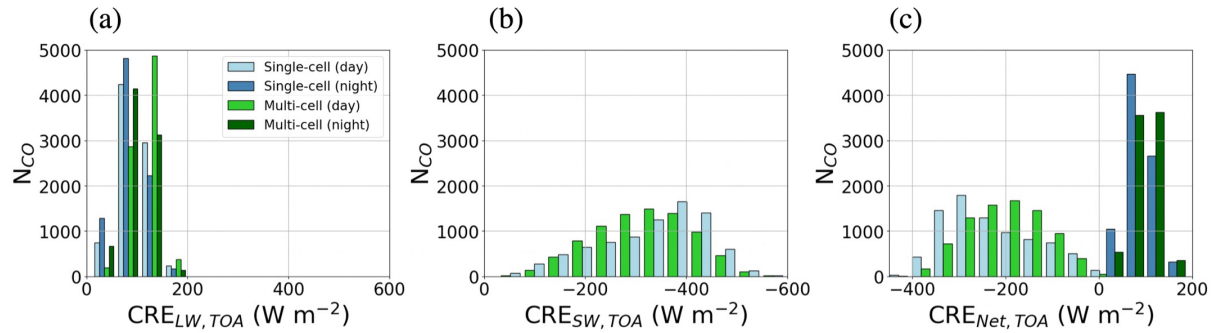
FIGURE 5.5: Distributions of single- and multi-cell convective objects' mean TOA a) day and night LW, b) daytime-only SW, and c) day and night net CRE between 2006-2011. Here SW CRE is only normalized over daytime hours since daytime and nighttime COs are explicitly separated.

W m^{-2} and 14.6 W m^{-2} more $< CRE_{LW,TOA} >$, respectively, than their nighttime counterparts. This is also reflected in Figure 5.5a that shows distributions of $< CRE_{TOA} >$ for all individual convective objects sorted by day and night. The range of $< CRE_{LW,TOA} >$ for both daytime and nighttime overpasses is between 0-200 W m^{-2}, while for daytime-corrected TOA SW CRE, the spread of values is nearly 3 times larger (-50 to -600 W m^{-2}). This results in a TOA net CRE spread that is bimodal with daytime COs contributing to the peak around -300 W m^{-2} and nighttime COs contributing to the second peak between 50-100 W m^{-2} that, when averaged together, produces a mean TOA net CRE of -61.5 W m^{-2}.

5.4 Relating Convective Cloud Properties to their Radiative Effects

5.4.1 Role of Cloud Thickness

The large spread in CRE values apparent in Figure 5.5 is due to the wide range of cloud characteristics that convective systems obtain through differing environmental forcings and life stages. Therefore, the focus of this section is to break down how cloud thickness and cloud top height fundamentally influence their cloud radiative effects among the different CO categories. The top row in Figure 5.6 directly compares $< CRE_{LW,TOA} >$ and $< \widehat{CRE}_{SW,TOA} >$ for COs observed between 2006-2016. Here, and in all subsequent plots, only daytime COs where both LW and SW CRE are available are considered but SW CRE is normalized to emulate their net effect over the full diurnal cycle. The hexbins are colored by the fraction of the CO with a column-integrated cloud optical depth less than one ($F_{COD<1}$ and hereafter, "thin cloud") divided by the fraction of the CO with a COD greater than three ($F_{COD>3}$ or, "thick cloud"), to depict how both SW and LW CRE respond to cloud thickness. COD is integrated over only the atmospheric layers that belong to the high-level cloud to ignore underlying cloud. The -1:1 dashed line signifies the critical point where systems contribute a warming (above the line) or cooling (below the line) at the top-of-atmosphere. The bottom row in Figure 5.6 elaborates on cloud thickness properties by presenting the thin cloud fraction distribution relative to the distribution of thick cloud amount.
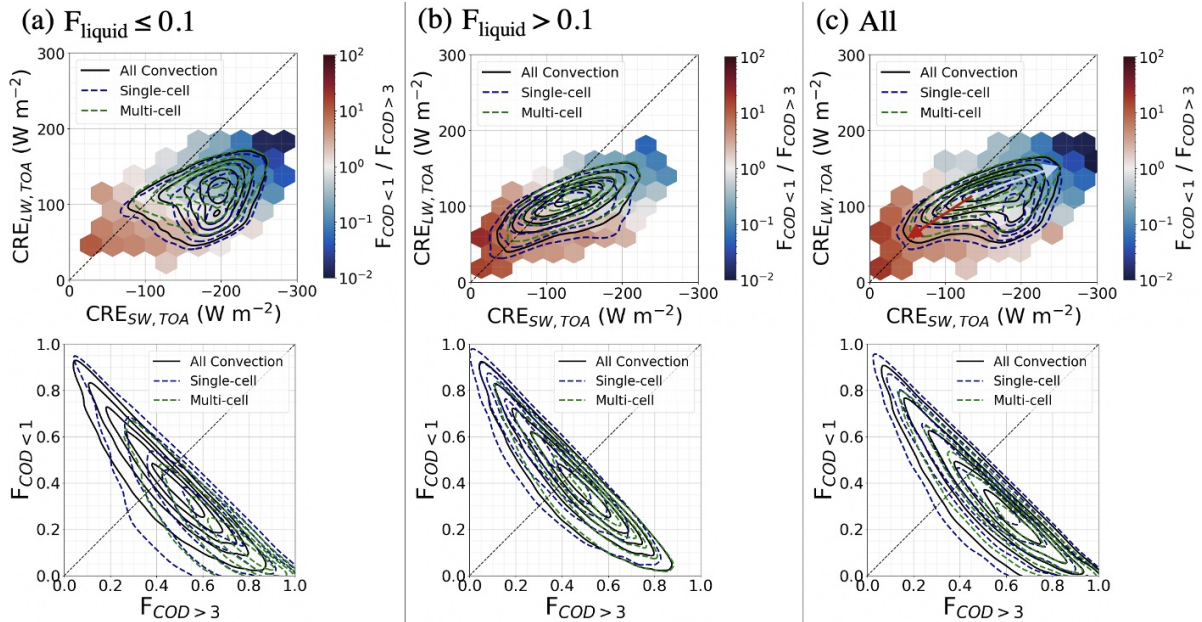
FIGURE 5.6: (Top row) Mean LW CRE vs. mean SW CRE (top row) and (bottom row) fraction of CO with COD < 1 ($F_{COD<1}$) vs. fraction of CO with COD > 3 ($F_{COD>3}$) density contours of early afternoon (a) ice-only ($F_{liquid} <= 0.1$) COs, (b) COs containing low cloud ($F_{liquid} > 0.1$), and (c) all COs. Each CO population is further sorted by single-cell (blue dashed), multi-cell COs (green dashed), and all COs (solid black). Each line contour represents an increase in 10% of the CO population, with the innermost (outermost) contour representing 10% (90%) of the population. Hexbins in the top row are colored by $F_{COD<1}$ / $F_{COD>3}$ and at least 4 COs are required within each hexbin. The direction of spread for COs that contain more (less) thin cloud than thick cloud is highlighted by red (blue) arrows in panel c.

For most of the COs, their SW CRE is more enhanced than their LW CRE as denoted by the contours lying to the right of the -1:1 dashed line. There are two prominent cloud thickness regimes: COs that contain more thick than thin cloud (blue hexbins) and COs that contain more thin than thick cloud (red hexbins). Figure 5.6c suggests a nearly equal population between thicker and thinner COs with the distribution centered on COs that have an equivalent thin-to-thick cloud ratio. Thicker COs have a greater shortwave cloud radiative effect due to higher cloud opacities and albedos compared to thinner COs. Thicker COs also have a higher top-of-atmosphere longwave cloud radiative effect than

thinner clouds because thin clouds allow some emission from the warmer atmosphere below the cloud to escape to space. COs that contribute a neutral or warming impact, which are designated by contours above the -1:1 dashed line, are primarily composed of thin cloud because they are transparent to incoming SW radiation while simultaneously reducing the outgoing longwave radiation.

Figures 5.6a and b categorize CO populations by ice-only or if they contain underlying cloud to isolate low-level cloud radiative contributions to the top-of-atmosphere energy budget. Ice-only systems primarily cool. However, 20% of the systems containing underlying liquid cloud contribute a warming compared to only 5% of ice-only systems. The systems that contribute a warming contain mostly thin cloud, and in fact systems with low-level cloud are more frequently comprised of thin cloud compared to ice-only systems. While the presence of underlying cloud tends to enhance the convective systems' cloud opacity, this result suggests that the opacity by the combined anvils and low-level cloud do not outweigh the greenhouse effect by anvils.

5.4.2 Role of Cloud Top Height

Figure 5.7 shows that $< CRE_{LW,TOA} >$ is the largest for COs that are primarily composed of thick cloud and have the highest cloud top height. $< CRE_{LW,TOA} >$ decreases as a function of both a decrease in cloud top height and an increase in the amount of thin cloud at the expense of thick cloud. When comparing between single- and multi-cell systems, multi-cell systems have a larger $< CRE_{LW,TOA} >$ than single-cell systems for the same given cloud top height and cloud thickness ratio. This, combined with the fact

that multi-cell systems have a higher ratio of thick to thin cloud compared to single-cell systems, explains why the distribution of $< CRE_{LW,TOA} >$ for multi-cell COs is shifted towards larger values than those of single-cell systems.

The $< \widehat{CRE}_{SW,TOA} >$ of COs has a slightly different response to cloud properties compared to $< CRE_{LW,TOA} >$. Only for systems containing primarily thick cloud does $< \widehat{CRE}_{SW,TOA} >$ increase with increasing cloud top heights (middle row of Figures 5.7a and b), which is arguably because the higher the cloud top height, the thicker the cloud. However, as thin cloud fraction increases, the change in $< \widehat{CRE}_{SW,TOA} >$ with CTH becomes negligible. $< \widehat{CRE}_{SW,TOA} >$ for COs with cloud top heights below 8 km, or the congestus mode, is much less sensitive to cloud thickness changes compared to systems with higher cloud tops as they likely contain small liquid drops that are brighter than ice clouds even when they are thin (not shown).

Overall, COs with a cloud top below 8 km produce a net cooling top of atmosphere radiative effect regardless of their cloud thickness (not shown), whereas COs with a high cloud top and composed of more thin cloud compared to thick cloud are radiatively neutral or even contribute a net warming (Figure 5.7, third column). Multi-cell COs have a slightly more enhanced $< CRE_{LW,TOA} >$ and weakened $< \widehat{CRE}_{SW,TOA} >$ compared to single-cell systems for a given cloud thickness ratio. Thus, there is a greater frequency of multi-cell systems that have a radiatively neutral effect at the top of the atmosphere compared to single-cell systems.

(a) Single-cell
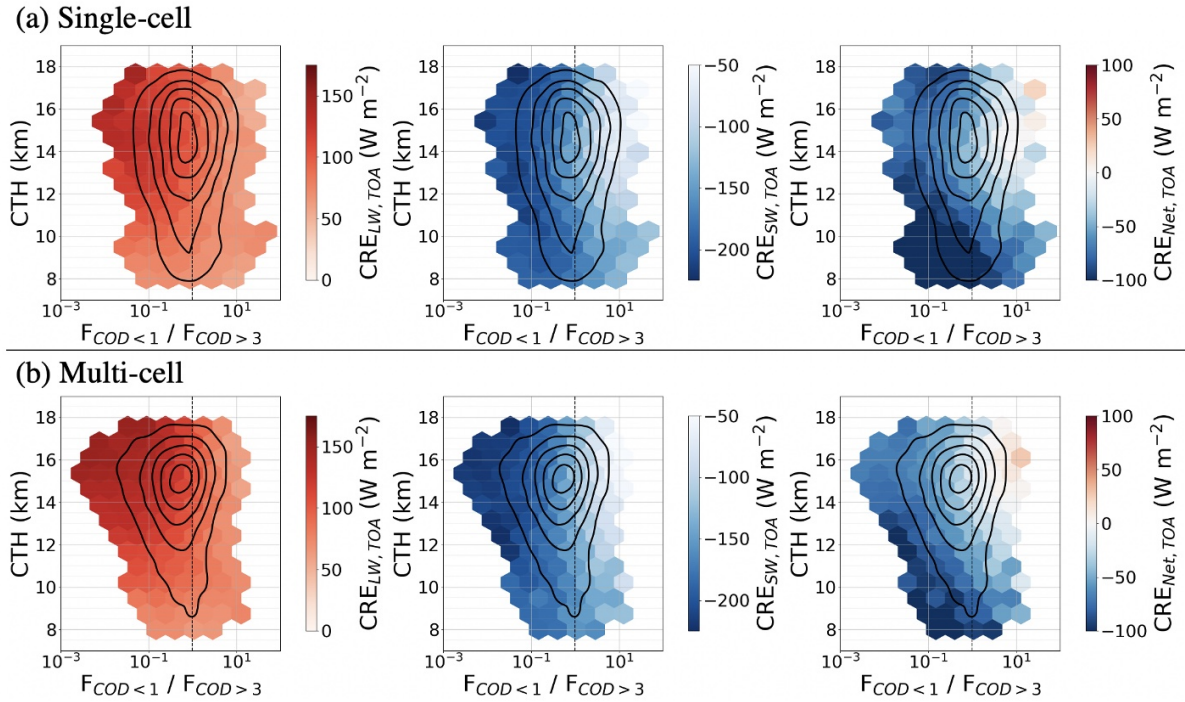
(b) Multi-cell

FIGURE 5.7: Cloud top height (CTH) versus the ratio of thin to thick cloud ($F_{COD<1}/F_{COD>3}$) for (top row) single-cell and (bottom row) multi-cell COs. Each line contour represents an increase in 10% of the CO population, with the innermost (outermost) contour representing 10% (90%) of the population. Hexbins are colored by (a&d) $< CRE_{LW,TOA} >$, (b&e) $< \widehat{CRE}_{SW,TOA} >$, and (c&f) $< CRE_{Net,TOA} >$. At least 4 COs are required within each hexbin.

5.5 Linking Cloud Radiative Effects to Convective Core Intensity

Although convective clouds statistically contribute a cooling effect at the top of the atmosphere, their individual SW and LW CREs are highly variable. This is in part due to their differing cloud top height and cloud thickness features, suggesting that there are varying in-cloud microphysical processes at play. How the strength of the vertical transport within cores relates to the distribution of ice hydrometeors to form a convective system is a key relationship to unpack in the present-day climate, particularly because
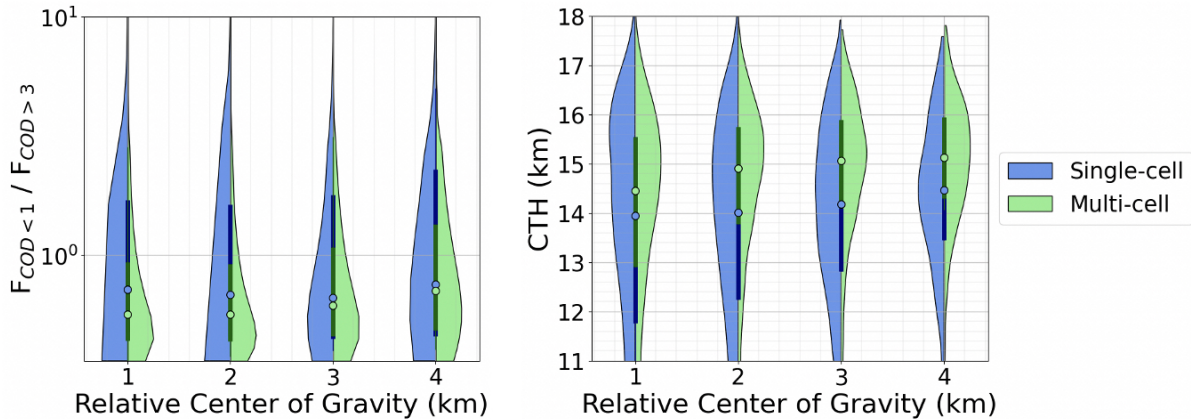
FIGURE 5.8: (Left) Ratio of thin to thick cloud fractions and (right) mean cloud top height as a function of rCOG for daytime deep single-cell (blue) and multi-cell (green) COs between August 2006 - December 2016 (excluding April - December 2011).

this relationship might evolve as the climate warms. The focus of this section is to sort cloud characteristics and their radiative responses by populations of convective objects with different convective core vertical intensities.

5.5.1 Convective cloud properties as a function of intensity

Figure 5.8 shows how the distributions of cloud thickness fraction and cloud top height vary with populations of single- and multi-cell systems sorted by their deep convective core rCoG. Over 50% of single-cell and 75% of multi-cell COs have a greater fraction of thick cloud to thin cloud regardless of their core intensity. However, there is an increased tendency for more intense COs to have a larger area of thin compared to thick cloud. The righthand plot in Figure 5.8 shows that on average, cloud top height increases with intensity. This supports previous work that highlights a correlation between the radar-defined convective core intensity (e.g., echo-top height) and cloud top height (e.g. Liu et al., 2007).

5.5.2   Radiative response to intensity for single-cell systems

Figure 5.9 depicts the distribution of $< CRE_{LW,TOA} >$ and $< \widehat{CRE}_{SW,TOA} >$ for early afternoon single-cell COs sorted by their convective core rCoG and colored by the ratio of thin cloud to thick cloud areas. For ice-only systems (top row), the amount of thick cloud increases at the expense of thin cloud with increasing core intensity. More intense COs are distributed towards more enhanced LW and SW CRE compared to weaker COs given that they are associated with increased cloud thickness and cloud top heights (Figure 5.8). The blue arrow indicates that the distribution of COs moves to a more enhanced SW CRE compared to LW CRE as thick cloud increases at the expense of thin cloud. The highest percentage of ice-only systems that contribute a neutral or warming impact belong to the most intense category despite the amount of thin cloud area relative to thick cloud decreasing with increasing intensity. In fact, some systems that contribute a neutral impact contain a thick cloud area that is two times greater than the area of thin cloud (i.e., $F_{COD<1}/F_{COD>3} = 0.5$). This suggests that systems need not contain as large of a thin cloud area to still contribute a warming owing to the LW enhancement with intensity.

Systems containing underlying liquid cloud happen to increase in thin cloud area, resulting in a greater frequency of COs to contribute a neutral or warming impact, in response to increased intensity. The spread of COs composed of primarily thin cloud runs parallel to the dashed line and can contribute a neutral or warming effect, while those that have a greater thick to thin cloud ratio have a more enhanced SW compared to LW CRE, thus

contributing a cooling effect. Combining the populations of ice-only systems and systems containing low-level cloud (bottom row of Figures 5.9 and 5.10) results in the most intense CO population containing the highest number of COs that contribute a warming effect. The systems that contribute the most cooling (i.e., farthest from the line) are those with the lowest cloud top heights, which are on the order of 10-12 km. However, the 10-12 km population of systems does not exist for COs with an rCoG greater than 3 km; rather, cloud top heights are higher than 12 km for this population. As intensity increases, the distribution of the thin cloud CO regime becomes increasingly parallel to the dashed line (as denoted by the red arrows), meaning that the SW and LW CREs cancel each other when averaging over this population. However, the distribution of COs with a greater fraction of thick cloud has increasingly higher SW and LW CREs with increasing intensity. The change in LW CRE is greater than the change in SW CRE per intensity increase, resulting in the most intense COs having an overall weakened cooling impact. In other words, given that the LW CRE is enhanced in response to the higher cloud top heights, the most intense systems must have a higher thick to thin cloud ratio than weaker systems to contribute an equivalent top-of-atmosphere net cooling effect.

5.5.3   Radiative response to intensity within different ocean basins

We would like to determine whether the relationships between cloud thickness and radiative properties to intensity over the full tropics are represented within specific ocean basins that have different environmental conditions. Figure 5.11 presents the difference between the distributions of single-cell systems with an rCoG > 3 km (green) and those
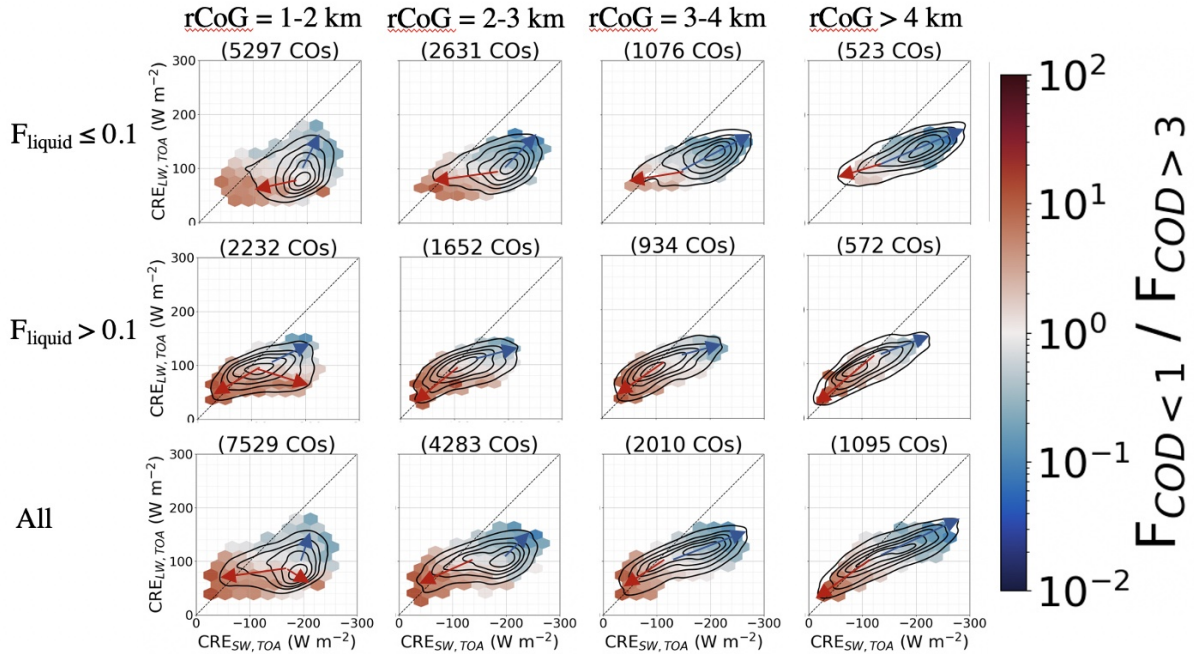
FIGURE 5.9: Convective object mean LW CRE vs. mean SW CRE sorted by their convective core relative Center of Gravity (rCoG) within early afternoon single cell convective objects. The rCoG values are binned by 1-2 km (first column), 2-3 km (second column), 3-4 km (third column), and greater than 4 km (fourth column). The top row is for ice-only systems, the second row is for systems containing underlying liquid cloud, and the third row a combination of both populations. The direction of spread for COs that contain more (less) thin cloud than thick cloud is highlighted by red (blue) arrows.

with an rCoG between 1-2 km (purple). It is apparent in each of the ocean basins that systems with a higher intensity have a greater tendency to contribute a neutral or warming impact compared to weaker systems. Furthermore, in each of the ocean basins except for the South Pacific Ocean, the radiative effects of the two cloud thickness regimes (i.e., $F_{COD<1}/F_{COD>3} < 1$ and $F_{COD<1}/F_{COD>3} > 1$) show up as two distinct nodes: the thick cloud regime is densest at higher SW and LW CREs to the right of the dashed line and the thin cloud regime is centered on or to the left of the dashed line. This is most noticeable over the East and Central Pacific Oceans. There is a greater population of the most intense COs that contribute a neutral or warming effect compared to a cooling effect over
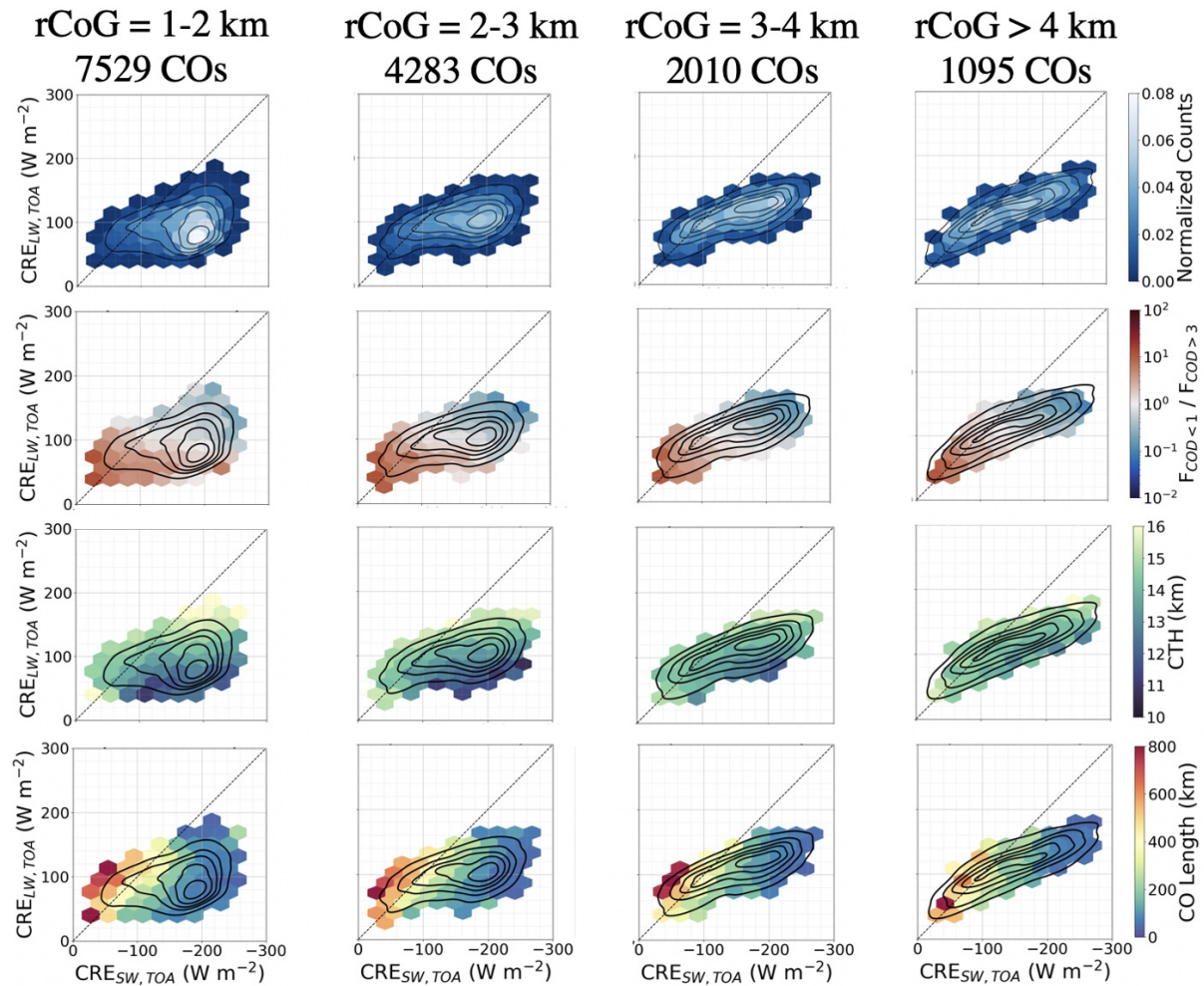
FIGURE 5.10: Like Figure 5.9, but instead with each row colored by different cloud features. The top row is colored by the counts of within each hex bin normalized by the sample size of each rCoG regime, the second row is colored by the thin to thick cloud ratio, the third row is colored by cloud top height, and the bottom row is colored by the CO length.

the Indian Ocean and West Pacific Ocean. Interestingly, the peak density of most intense systems is unimodal over the South Pacific Ocean. The distribution is centered just to the right of the line signifying that these systems contribute a very small cooling impact.
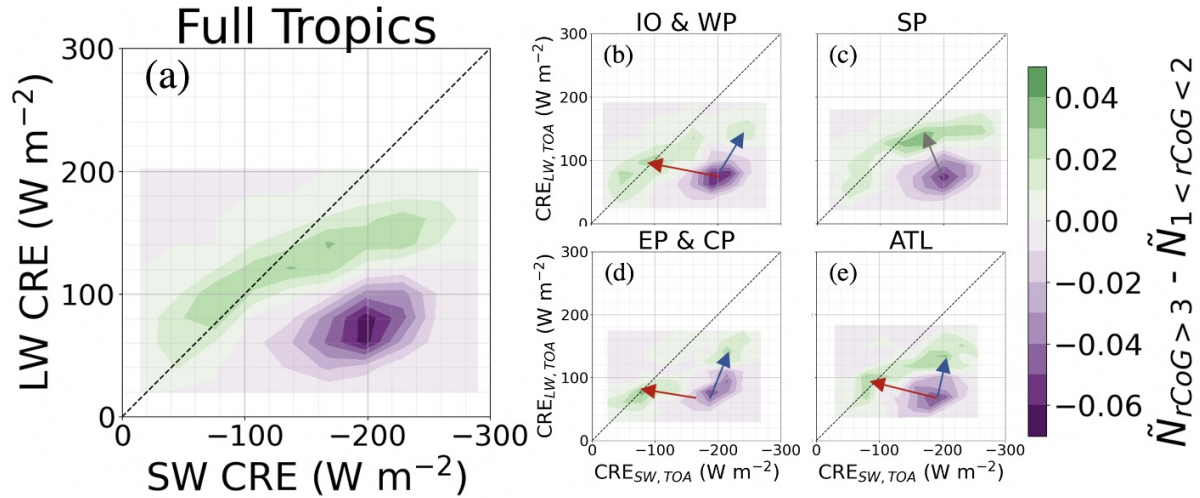
FIGURE 5.11: The difference in normalized counts between the rCoG > 3 km and rCoG 1-2 km daytime-only single cell CO populations expressed as filled contours over a) the full tropical ocean, b) Indian & West Pacific (IO & WP), c) South Pacific (SP), d) East & Central Pacific (EP & CP), and e) Atlantic (ATL) Oceans.

5.5.4 Discussion: multi-cell CO behavior, how cloud and radiative properties relate to cloud extent, and convective organization

Supplemental Figures A.5-A.7 are analogous to Figures 5.9-5.11, except they show the cloud and radiative responses by multi-cell populations sorted by their mean convective core intensity. Overall, the distributions are similar to those of single-cell COs in that a higher frequency of intense multi-cell COs contribute a neutral or warming impact compared to the weakest COs. The cloud and radiative responses to increasing intensity are slightly less pronounced for multi-cell COs compared to single-cell for a couple of reasons. Under the assumption that a multi-cell system represents a large-scale organized system with multiple precipitating cells, averaging the rCoG of multiple cores that could

have various magnitudes could misrepresent the relationship between the intensity of a single core and its adjacent anvil. Another possibility is that multi-cell systems are often in their mature stage, meaning they have reached their maximum cloud top height and thickness, thus their cloud relationships are slightly decoupled from instantaneous updraft intensities. A final possibility is that these systems are not organized under the same physical processes, so averaging rCoG cross all cores would obscure cloud-intensity relationships of systems with their own unique properties.

The tropical high cloud amount feedback considers how cloud extent changes as a function of intensity. By assuming that the CO length is representative of the diameter of the system Igel and van den Heever (2015b), Figure 5.12 presents the relationships between CO length and convective intensity. On an individual convective system scale, which is defined as a system with a single precipitating column, the median cloud extent for the most intense systems increases compared to the weaker populations. Other studies have noted an increase in anvil development associated with systems that have an extensive depth in the atmosphere (e.g. Li and Schumacher, 2011; Stubenrauch et al., 2023), which could be due to the immense transport of hydrometeors to the upper troposphere by intense updraft regions that then spread into large anvils. Interestingly, the distribution spread and median cloud extent for the most intense multi-cell systems decreases. This perhaps highlights a potential feedback between increased updraft intensity and convective system clustering, which is at the root of proposed convective organization mechanisms.

Studies have noted that there is a relationship between cloud extent and thickness (e.g. Li
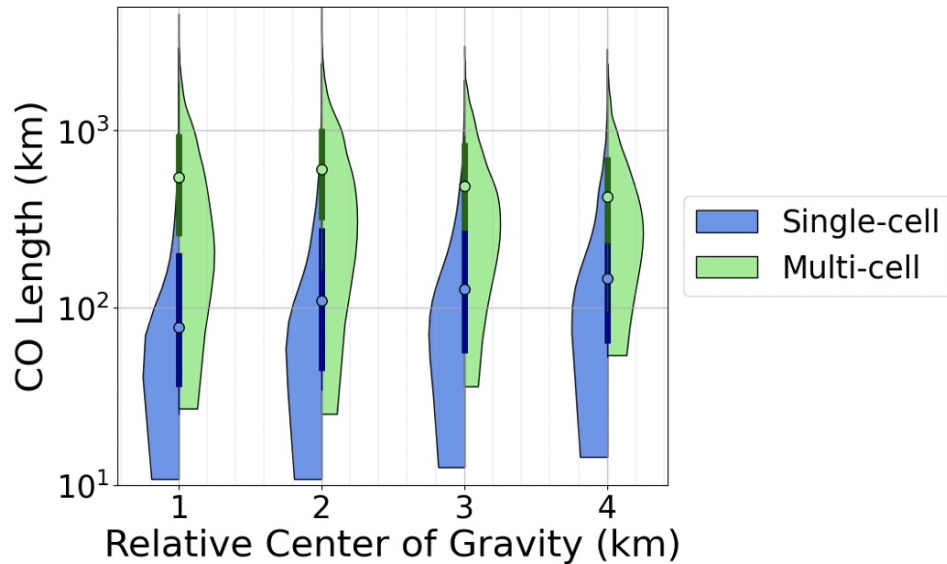
FIGURE 5.12: Like Figure 5.8, but with CO length on the y-axis.

and Schumacher, 2011; Yuan and Houze, 2010). The largest systems, regardless of their intensity, consist mostly of thin cloud (bottom rows of Figure 5.10 and Supplemental Figure A.6) and contribute a neutral or warming impact, while the smallest systems are comprised of primarily thick cloud and contribute a cooling impact. Under the assumption that the CO extent indicates the age of the convective system (Yuan et al., 2011), it follows that systems undergo different top-of-atmosphere radiative effects at each stage of life, with the developing stage contributing primarily a cooling impact and the end of the mature to decay stage contributing a warming impact (Hartmann et al., 2018; Houze Jr., 1982).

5.6 Conclusion

The focus of this analysis was to reveal present-day relationships between convective intensity and their cloud properties and how these properties influence the top-of-atmosphere radiative energy budget. CloudSat and CALIPSO measurements were employed because of the high sensitivity to cloud droplets, including thin anvil, to identify deep convective objects (CO) containing either a single or multiple precipitating column(s). Each CO had a qualitative convective core intensity assigned to it based on a reflectivity-weighted calculation of the core center of mass. This calculation, also known as the relative (to the freezing level) Center of Gravity (rCoG) is particularly useful because it can be calculated directly within both cloud and global storm resolving models (CRMs, GSRMs). To assess the radiative response of convective systems based on their cloud thickness, the cloud optical depth was integrated over the cloudy layer (excluding low-level or upper-level multi-layer clouds) within each profile of the CO. The fraction of the CO with a COD less than 1 divided by the fraction greater than 3 was used as proxy for a "thin"-to-"thick" cloud ratio.

On a tropics-wide scale, convective clouds contribute a net cooling of -2 W m^{-2} to the total top-of-atmosphere radiative energy budget. It is small due to a combination of factors:

1. Because COs occur, on average, only 3% of the time compared to the frequency of A-Train flyovers, their contributions to the global top-of-atmosphere radiative

energy budget are minimal.

2. Convective clouds have varying radiative effects over the course of the diurnal cycle. At night, convective systems only contribute to a top-of-atmosphere longwave cloud radiative effect. However, the shortwave impact during the day is strong enough that it offsets the longwave warming at night such that they still contribute a small cooling when averaging over both day and night.

3. Convective systems have varying cloud opacities and cloud top heights, meaning that there is a 200 W m^{-2} range in mean LW CRE and 600 W m^{-2} in mean SW CRE. However, because LW CRE and SW CRE are often simultaneously either enhanced or weakened depending on the cloud thickness, the nearly equal and opposite LW and SW CREs cancel.

As convective cloud properties are expected to alter under climate scenarios, it is worth assessing present-day relationships between convective intensity, which might increase with climate, and their cloud thickness and radiative responses. Both single- and multi-cell COs sorted by their intensity were found to have two distinct cloud thickness regimes. COs with more thin than thick cloud have nearly equal and opposite SW and LW CRE contributions such that their effects increasingly cancel each other as intensity increases. For systems with primarily thick cloud, both the SW and LW CRE contributions increase with increasing intensity, but the LW effect is more sensitive to intensity in SW CRE resulting in these systems more often contributing a weakened cooling or neutral effect. In order for more intense "thick cloud" systems to have an equivalent CRE as weaker

"thick cloud" systems, the ratio of thick to thin cloud must be significantly larger for the more intense systems compared to the weaker systems to enhance the SW CRE and offset the LW CRE.

The radiative response to the two cloud thickness regimes in response to increasing intensity were consistent among both single-cell and multi-cell systems. However, the relationship between convective object length and intensity differs between single- and multi-cell systems differ, with the median single-cell extent increasing and multi-cell extent decreasing with increased intensity. This indicates the importance in understanding how physical processes on multiple scales are at play to influence convective system development on the individual cloud (updraft) scale and on the scale of organized systems consisting of several distinct updrafts. It is also important to understand how processes differ among environments. It was found that cloud radiative effects from convective systems vary in different regions across the ocean, with specific attention to the unique radiative response over the South Pacific Ocean compared to the other ocean basins.

There are limitations to this analysis that should also be addressed. Firstly, whether rCoG is representative of the instantaneous properties of convective updrafts or rather retains memory of previous updrafts remains unclear. For this, it would be useful to simulate the relationship between rCoG and the vertical velocity of updrafts within a CloudSat simulator. Another limitation in the methodology could be how well-represented using the COD thresholds for defining thin and thick cloud are. Furthermore, it would be interesting to explore how COD magnitudes influence their radiative response. For example, how

does the radiative effect of a system that has mostly thick cloud with a COD just above 3 compare to the radiative effect of a system containing 50% cloud with a COD >> 3 and 50% with thin cloud?

Furthermore, this analysis did not focus on convective cloud and radiation relationships to the thermodynamic and dynamic environment, which is important to do to put these results in the context of what might happen under climate change scenarios. In the future, it would be beneficial to make connections to studies that have focused on anvil behavior in response to differing sea surface temperatures and vertical velocities on 100 km domain scales.

Finally, it was noted that convective systems in this analysis primarily contribute a cooling effect, which goes against the notion that they contribute a near-zero effect (Hartmann et al., 2001; Kiehl, 1994). The cooling observed from the active convection studied in this analysis is likely offset by cirrus clouds that are formed and sustained during the decay stage of the convective system. These clouds are the main warming contributors. Thus, it would be very beneficial to quantify the radiative response of convective systems at different life stages as well as the duration of each life stage to understand the full CRE contribution. This could be done by employing cloud tracking mechanisms within other satellite observing platforms (e.g. Fiolleau and Roca, 2013; Xu et al., 2019).

Chapter 6

Conclusion

6.1 Synthesis

Because atmospheric deep convection plays such an important role in influencing Earth's global energy budget, it is increasingly important to consider how deep convective cloud and energetic properties might change due to a changing climate. Updraft vertical velocities may increase in regions that are becoming increasingly moist with warming sea surface temperatures. This could alter the distribution of hydrometeor vertical and horizontal extent, thus influencing both precipitation and anvil cloud development. The focus of this work, therefore, is to document the relationships between these properties applied to our present-day understanding of how convection fundamentally contributes

to the Earth's energy budget: by 1) vertically transporting energy and mass to the upper troposphere, 2) balancing clear-sky radiative cooling through latent heating, and 3) modulating the top-of-atmospheric radiative energy budget.

Because the processes influencing how updraft strength relates to cloud and precipitation development occur on the convective cloud scale and smaller (e.g., cloud microphysical processes), it is necessary to document such characteristics on these scales. We use A-Train observations to create a database of "convective objects" that provides nearly global information on vertical intensity, anvil thickness and horizontal extent, rain rates, radiative effects, and large-scale environmental conditions at 0130 and 1330 LST between 2006-2017. Deep convective cores are identified within CloudSat flyovers based on the height at which the radar signal is attenuated. We define a proxy for the strength of any one core as the height of its reflectivity-based Center of Gravity relative to the freezing level (rCoG).

Chapter 3 showcases the nearly global distribution of convective objects at 0130 and 1330 LST, and provides a complementary cloud perspective to the analyses using a precipitation perspective with TRMM observations (e.g. Liu and Zipser, 2013; Liu et al., 2007; Zipser et al., 2006). As was noted in Zipser et al. (2006), deep convective cores are primarily the most intense over tropical land, specifically over the Congo Basin in Africa. We expand upon TRMM observations by showing that deep convective clouds are the most extensive over the Maritime Continent, as was documented in previous analyses using field campaign and CloudSat-CALIPSO measurements (e.g. Deng et al., 2016; Maddox,

1980; Mapes and Houze, 1993). Most noteably, we leverage the fine spatial resolution and high sensitivity of the CloudSat CPR to identify deep convective cores on a nearly kilometer-scale. We find that convective objects with a high number of deep convective cores primarily have the longest horizontal length scales owing to the amount of non-precipitation anvil that is developed. However, the increase in core prevalence within a system does not necessarily entail that the mean intensity of the system increases. Finally, in addition to the tropics we document characteristics of deep convective systems within the upper latitudes, which would be worth further exploration.

Energy budget analyses on an oceanic tropics-wide, day-to-day scaling tells us that convection redistributes energy and moisture so as to stabilize the tropical environment. However, it remains unclear the role that deep convection plays in exporting energy out of the tropics on longer time scales. Is it the case that updrafts are the sole providers of the energy surplus in the upper troposphere, as was first proposed by Riehl and Malkus (1958) and Riehl and Simpson (1979)? Or do the thermodynamic contributions from stratiform precipitation and LW atmospheric radiative heating by the extensive clouds need to be considered for lateral export (Houze Jr., 1981; Needham and Randall, 2021)? Chapter 4 expands upon the cloud, precipitation, and radiative characteristics laid out in Chapter 3 within the context of lateral energy transport. We identify *hot towers*, or deep convective cores that reach the tropopause, within the tropical trough zone (TTZ; 13°S-19°N), under the assumption that most of the energy transported to higher latitudes occurs within this region (Riehl and Malkus, 1958; Riehl and Simpson, 1979; Stephens

et al., submitted). Deep convective characteristics are largely variable both geographically and temporally, with most of the bulk mass from both convective cores and hot towers being transported to the tropopause over continental land. If it is the case that the updrafts are primarily responsible for providing the energy for lateral transport, then might it be that most of the energy is being exported over tropical land? However, if the thermodynamic and radiative characteristics of deep convective systems are important contributors, then upper tropospheric energy supplies for transport are primarily over the ocean and Maritime Continent.

It is worth considering the energetic contributions by convection within the upper troposphere within a climate context as well. It has been suggested that precipitation is strengthening and clouds are clustering within the Intertropical Convergence Zone (ITCZ) due to warming sea surface temperatures associated with a narrowing of the large-scale mean ascent (eg. Byrne et al., 2018; Su et al., 2017; Wodzicki and Rapp, 2022). Under this notion, it begs the question of how might the amount and distribution of energy within the upper troposphere change? Would these precipitation and cloud properties influence the amount of energy being transported out of the tropics?

Although not directly addressing the previous question, the last analysis chapter is motivated by what might happen to clouds and their top-of-atmosphere radiative effects in a changing climate. Observations suggest that both shortwave and longwave radiative fluxes at the top of the atmosphere can alter in response to modifications to the large-scale circulation over the decadal timescale (Chen et al., 2002; Wielicki et al., 2002;

Wong et al., 2006). Changes in the top-of-atmosphere radiative effects are a response to changes in high cloud behavior, yet it is uncertain how exactly high clouds could have changed. Current theories suggest that an increase in convective intensity and precipitation efficiency is coupled with a decrease in anvil cloud extent owing to an increasingly stable atmosphere in response to warming sea surface temperatures (Bony et al., 2016; Mauritsen and Stevens, 2015; Saint-Lu et al., 2020). It follows that regions of clear-sky radiative cooling would increase, which would contribute to preventing sea surface temperatures from continuing to rise. This is the present-day theory underlying the *tropical high cloud amount feedback*. However, there exists uncertainties within climate models associated with this cloud feedback in large part due to not adequately capturing the relative radiative effects within the cloudy regions with respect to the clear-sky areas.

Therefore, the focus of Chapter 5 is to quantify the radiative response associated with convective cloud intensity and anvil cloud relationships. We constrain the analysis to be over the tropical ocean where theories for high cloud feedbacks have been assessed. It is found that active deep convective objects contribute an overall cooling at the top of the atmosphere, but that their contribution is quite small when considering their overall effect on the global radiative energy budget. This is in large part due to their limited spatiotemporal frequency and the cancellation of the LW and SW effects owing to a large variability in cloud characteristics. However, systems can contribute a warming, and they are often composed of at least 50% cloud with a COD < 1 (thin cloud).

Between populations of convective objects sorted by their intensity, we find that systems

that are the most intense have the highest cloud top heights, and there is a marginal tendency for these systems to have a higher fraction of thin cloud. Overall, the population of most intense COs have the most systems that contribute a warming at the top of the atmosphere. However, the systems that contribute a warming are primarily those that have the largest fraction of thin compared to thick cloud, and not necessarily those with the highest cloud top heights. Interestingly, the most intense population also has the largest range in SW CRE. Therefore, the most intense systems with primarily thick cloud still contribute a cooling, despite an overall increase in LW CRE, due to an enhanced SW CRE. Putting these results in the context of climate change, it is expected that convective clouds will increase in altitude with warming sea surface temperatures, which could marginally enhance their LW CRE (Zelinka and Hartmann, 2009, 2010). However, there might be a greater enhancement in LW CRE within the cloudy region if the reduction in cloud amount contributes more so to a thinning of the anvil as opposed to a reduction of the overall cloud extent. Finally, how the in-cloud radiative effects compare to the magnitude of clear-sky radiative effects would be an important next feature to capture.

6.2   Future Projects

We have the ability to do a lot more analyses given the amount of information stored within the convective object database. The following subsections are glimpses of projects that have been started through collaborations within and outside of the department.

6.2.1 Large-scale environmental controls on convective cloud properties and their radiative response

It is well-understood that deep convection over the ocean favors warm sea surface temperatures. Systems over the ocean predominantly exist over the West Pacific Warm Pool, although systems do exist elsewhere, such as in regions of low-level convergence. Regions of warm sea surface temperatures and low-level convergence are often associated with large-scale mean ascent. As mentioned previously, to a first order, this large-scale mean ascent is a signature of deep convective activity Emanuel (1994). Bony et al. (2006) noted that changes in the tropical mean radiation budget through cloud radiative forcings may be understood by highlighting convective processes that affect cloud development and radiation under specified dynamic and thermodynamic conditions. Within a climate context, Bony et al. (1997) had previously defined monthly mean vertical velocity at 500 hPa and sea surface temperatures (SSTs) as the large-scale dynamic and thermodynamic environments, respectively.

Using the A-Train convective object database, we build upon this work by considering cloud properties such as the vertical intensity of deep convective cores and cloud thickness as signatures of convective processes. Monthly mean vertical velocity at 500 hPa and SSTs from MERRA-2 are matched to the convective objects. Figure 6.1 presents how cloud thickness and radiative effects respond between single-cell CO populations of differing convective core intensity within varying large-scale oceanic environments tropics-wide.

We find that the change in LW CRE as intensity increases is not sensitive to differing large-scale vertical motion environments, but it does decrease with rising SSTs. A similar result is found for changes in SW CRE as a function of intensity. Convective systems over the coldest monthly-mean SST have the greatest increase in thick cloud fraction (i.e. thick cloud increases at the expense of thin cloud) associated with increasing intensity. This results in a weaker increase in net CRE with intensity associated with the coldest SSTs. The largest net CRE increase with intensity is associated with convection over SSTs greater than 299.25 K in ascending and weak vertical motion regimes. It is in these regimes where the LW CRE increase with intensity dominates over the change in SW CRE. Cloud thickness and CRE response to changes in intensity are weakened when considering the full distribution of convection (i.e. multi-cell systems; not shown). We would like to further this work by diagnosing which cloud properties, such as cloud top height and cloud thickness, are the most sensitive to changes in intensity within each large-scale environment. This can help to understand the unique LW and SW radiative effects within each environment.

6.2.2 Relating updraft strength to precipitation, cloud, and radiative efficiencies

How precipitation efficiency contributes to the overall story of convection and climate change has come up throughout this dissertation. Precipitation efficiency is defined as the ratio of surface precipitation to the condensed water path and is a useful metric for understanding large-scale dynamic and thermodynamic impacts on the hydrological
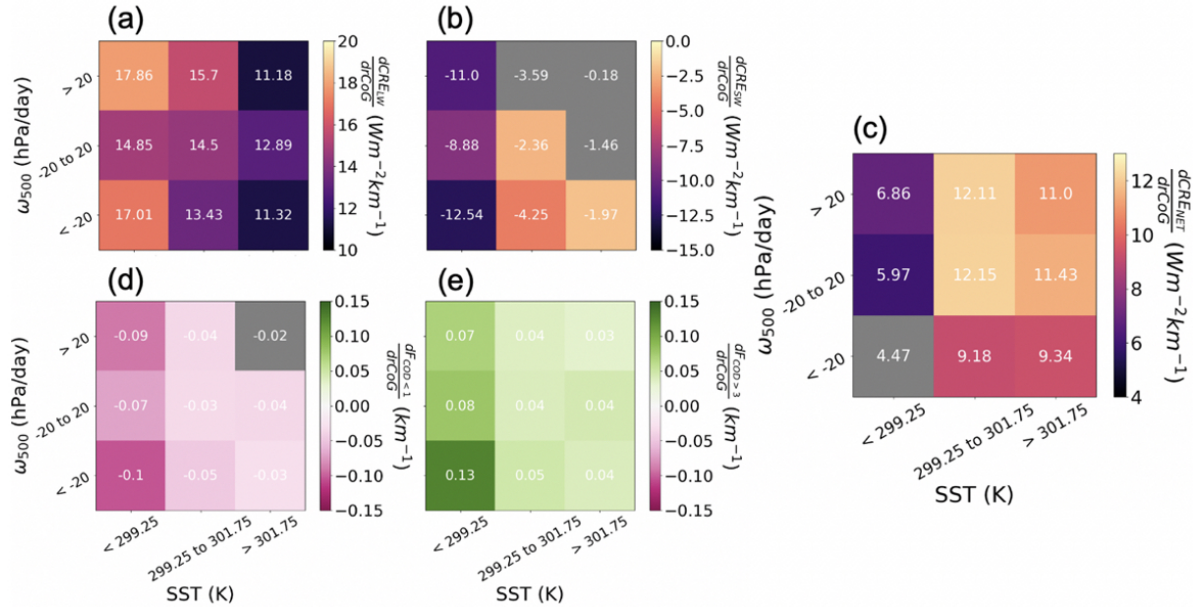
FIGURE 6.1: (a) Change in $< CRE_{LW,TOA} >$, (b) $< \widehat{CRE}_{SW,TOA} >$, (c) $< CRE_{Net,TOA} >$, (d) $F_{COD<1}$, and (e) $F_{COD>3}$, as a function of increasing ice-only, single-cell COs' convective core rCoG observed at 1330 LT and sorted by nine w500-SST regimes. The boxes that are in grey indicate that the correlation coefficient has a p-value > 0.05, so the regression is not significant.

cycle. It is thought that precipitation efficiency might increase in a changing climate (Chen et al., 2002; Lindzen et al., 2001; Mauritsen and Stevens, 2015); however, climate models disagree on both the sign and magnitude of this variable Li et al. (2022). It has often been defined within larger spatiotemporal domains than that of instantaneous cloud objects. But it is becoming increasingly common to capture precipitation efficiency both on a cloud object scale using derived precipitation, ice water path, and liquid water path from satellite observations (e.g. Ito and Masunaga, 2022; Rapp et al., 2005), and even on a convective updraft scale using precipitation, vertical velocity, and a large-scale vertical profile of saturation mixing ratio measurements from ground-based observations (e.g. Narsey et al., 2019).

We have begun looking into how the precipitation and precipitation efficiency of a full CO evolve as a function of core vertical intensity. Based on previous definitions of precipitation efficiency, it is defined by the equation:

$$\epsilon = \frac{<P>}{<IWP>} \tag{6.1}$$

where $<P>$ is the AMSR-E/AMSR2 mean rain rates of each CO in flux units (kg m^{-2} hr^{-1}) and $<IWP>$ is the column-integrated ice water path averaged over each CO from the CloudSat 2C-ICE product. Given large uncertainties associated with the liquid water path retrieval, we do not include it in the denominator and had argued that the IWP contributes the bulk of the condensate within the atmospheric columns of interest. However, upon reading more about precipitation efficiency, it is presently unclear to me whether the large-scale atmospheric condensate, thus the added LWP, needs to be considered within the denominator (Ito and Masunaga, 2022; Narsey et al., 2019).

Figure 6.2a shows the relationship between AMSR-E/AMSR2 rain rates averaged over the raining regions within convective objects and the mean convective core rCoG for single- and multi-cell systems. Both single- and multi-cell convective object populations with the highest convective core rCoG corresponding to a value of 5 km above the freezing level, are, on average, associated with the heaviest conditional mean rain rates. This suggests that from a tropics-wide statistical standpoint, the increased height of the bulk mass within cores, or vertical intensity, is correlated with an increase in rainfall rates. The same is the
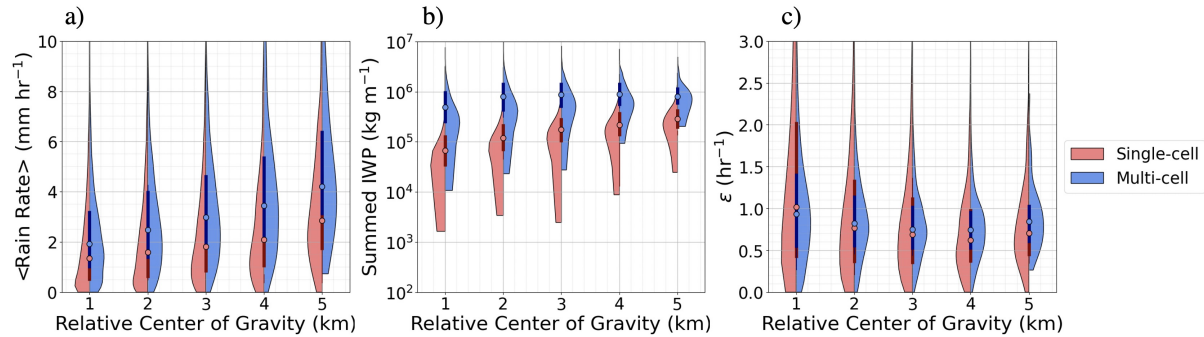
FIGURE 6.2: Violin plots of (a) conditional mean rain rates, (b) column-integrated ice water path (IWP) summed over each CO, and (c) precipitation efficiency (ϵ) as a function of mean convective core relative Center of Gravity calculated for single-cell (red) and multi-cell (blue) convective objects between 2006-2016 from 30°S – 30°N.

case for rain rates averaged over the full CO that is used in Equation 6.1 (not shown). Associated with increased rain rates is an increase in the total IWP for increasingly intense systems (Figure 6.2b). Our current results show that precipitation efficiency decreases as rCoG increases from 1 to 3, but then begins increasing again. Narsey et al. (2019) noted that precipitation efficiency for the most part increased with increased rain rates that increased with larger vertical velocities. However, the relationship between updraft velocity, rain rates, and precipitation efficiency altered in response to differing synoptic conditions. Further work needs to be done on our end to ensure accurate implementation of a proxy calculation for precipitation effiency.

6.2.3 Supplying life-cycle context to instantaneous measurements of A-Train convection

Chapter 5 shows that even within a given intensity population, there is a large spread in cloud radiative effects, which could be due to the large variability in convective life stages that are being captured within each intensity population. In a meeting with Brandon

Wolding a couple of days ago, he mentioned how it might be possible to map out the radiative properties of a convective system over the course of their life cycle. I have demonstrated such an idea on Figure 6.3 colored by CO length to connect it to the life cycle ideas from Yuan et al. (2011). At the initiation stage (1), one might expect the net CRE to be negative owing to a large negative SW CRE from primarily thick cloud and a small positive LW CRE from minimal thin cloud and low cloud top height. Stage 2 is the mature stage in which clouds have deepened thus increasing the LW CRE. The arrow might move towards weakened SW CRE as the amount of detrained cloud, and ultimately thin cloud, increases within the mature life stage. The decay stage (3) is denoted by detrained thin cirrus that have a weakened SW CRE and enhanced LW CRE so as to potentially contribute a warming.

Although it is not possible to track the life cycle of any single system using A-Train observations, we can supplement the CO database with geostationary satellite observations that track deep convective systems. Last summer I spent two months in France collaborating with scientists through Centre National de Recherches Météorologiques (CNRM) and Météo-France in Toulouse who have developed a tracking algorithm, otherwise known as Tracking of Organized Convection Algorithm through 3D SegmentatioN (TOOCAN), to track mesoscale convective systems (MCSs) over their full life cycle in geostationary data. By implementing thresholds of brightness temperature gradients in both space and time, MCSs are identified, tracked, and assigned life stages across the whole tropics (Fiolleau and Roca, 2013). The goal during my time there was to learn how to match the tracked MCSs to the A-Train-based convective objects with the hope that we could use
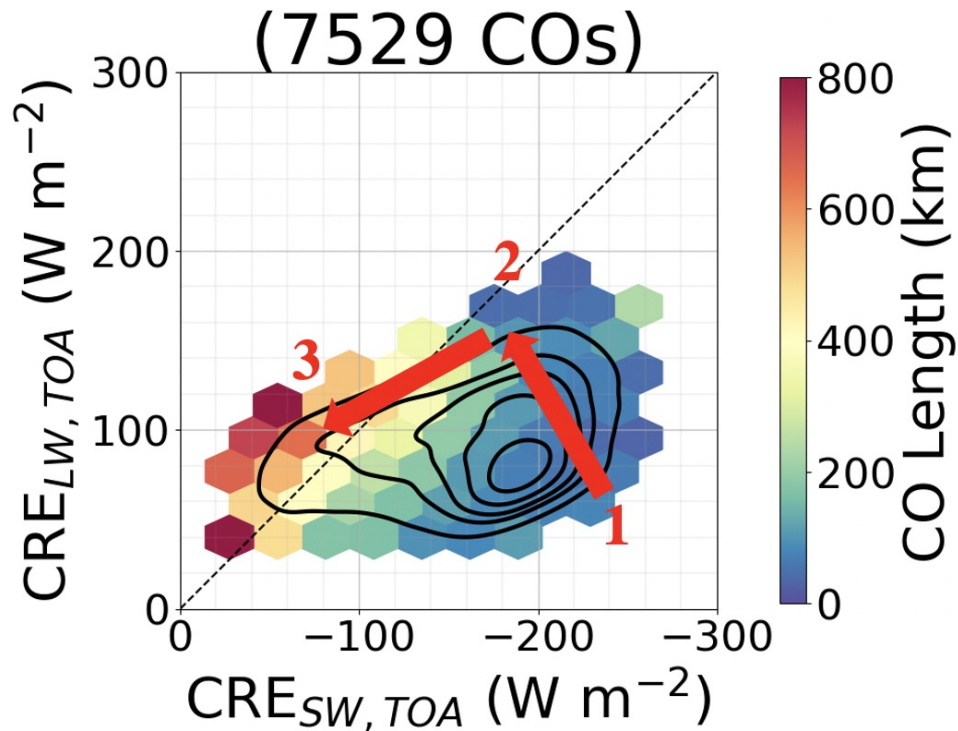
FIGURE 6.3: The bottom-left plot in Figure 5.10 with arrows overlaying the potential
life cycle of a convective system: 1 = initiation, 2 = mature, 3 = decay.

the merged data to understand how the vertical structure and their resulting radiative

effects evolve over time.

The most eye-opening component of this experience was simply being able to observe

how convection is organized using multiple perspectives. Figure 6.4 shows an example of

looking at a convective system consisting of several MCSs from the combined TOOCAN

and A-Train perspectives. This particular A-Train convective object consists of multiple

MCSs, which all have different life stages ranging from 1 (i.e., developing) to 5 (i.e., ma-

ture). To break down the complexities within convective cloud and system morphologies,

we would have to undergo an analysis on multiple scales. For example, on the scale of the

TOOCAN MCS, we seek to understand how convective core features vary when sorted

by distinct life stages. On the scale of the A-Train CO, how do the MCSs characteristics (e.g., life stage, duration, etc.) vary among each other within the CO? Figure 6.5 provides preliminary statistics on the number and life stage of MCSs within COs during one month (July 2014) over the tropical East Pacific Ocean. Nearly half of the observed COs have more than one MCS suggesting that the convective object framework is useful for characterizing the organization of multiple systems. Furthermore, almost the full spectrum of MCS life stages (aside from life stage three, interestingly) is captured within A-Train-detected convection, and there exists quite a range in life stages between MCSs even within the same CO.

It is also of interest to connect the convective cloud properties on multiple scales to the moisture and energetic impacts of convection at different life stages. Work has been started to combine A-Train convection and TOOCAN-tracked MCSs with relative humidity measurements from SAPHIR on board Megha-tropiques to study the two-way interaction between MCSs and environmental moisture over time. However, the specific science questions for this analysis have not been fleshed out yet.

6.2.4   Convection over the Tropical North Atlantic Ocean

I have been enjoying shifting my focus away from climate analyses to a process-level approach for studying convection in working with Angela Rowe's group. The focus of this collaboration is to use the A-Train convective object database to supplement measurements from the two Convective Processes Experiment (CPEX) field campaigns (CPEX-CV and CPEX-AW), which observed deep convective systems in two regions over the
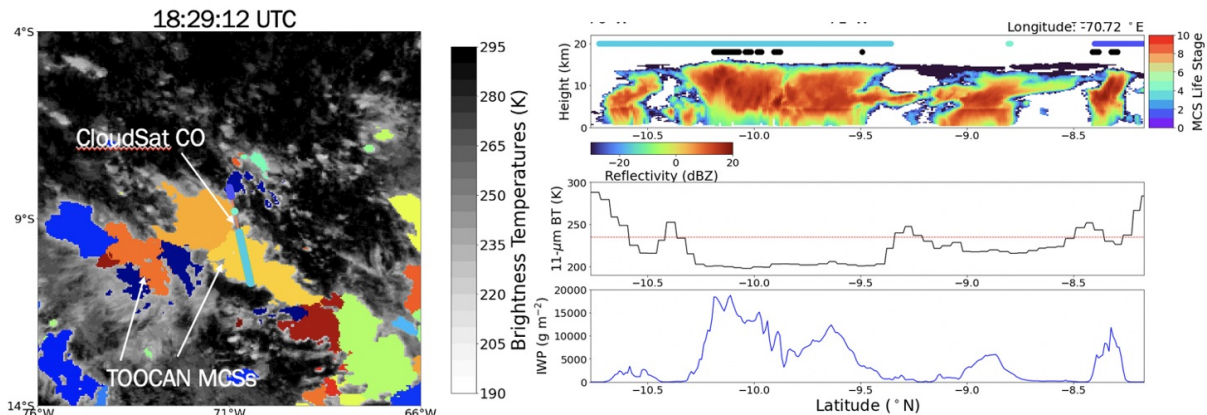
FIGURE 6.4: (Left) GOES-13 brightness temperatures with TOOCAN-detected MCSs represented by the filled colored areas. The A-Train-detected convective object (CO) is shown by the orange transect with blue dots overlaying it representing its life stage. (Right) Top: CloudSat-CALIPSO reflectivity profile of CO with colored dots above designating its life stage. Middle: Modis 11-micron brightness temperatures with red line corresponding to 235 K cutoff threshold that TOOCAN uses for high clouds. Bottom: Ice water path (IWP) from CALIPSO.
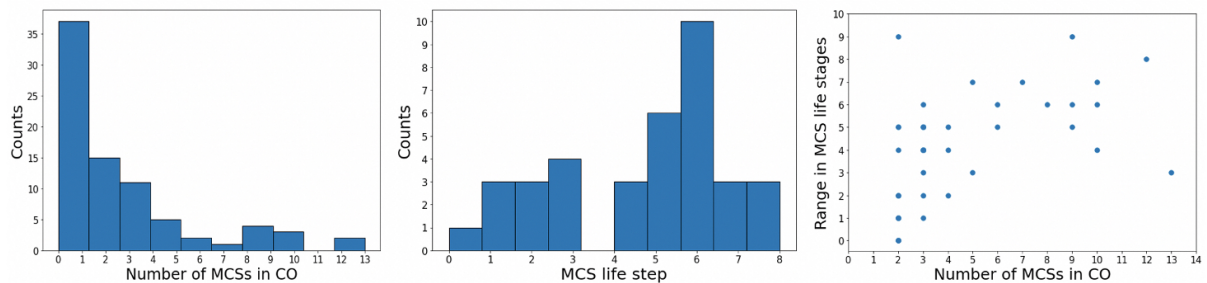
FIGURE 6.5: (Left) Distribution of the number of TOOCAN-detected MCSs within A-Train-detected convective objects over the Tropical East Pacific Ocean during July 2014. (Middle) Life stage of each MCS with 1: developing and 9: decaying. (Right) The range in MCS life stages as a function of the number of MCSs within each convective object.

Tropical North Atlantic Ocean. The motivation of these field campaigns were to relate the structure and development of convective systems to environmental conditions such as moisture and vertical wind shear. Therefore, I plan to characterize convective system properties, such as their size and raining area, as a function of vertical wind shear within the CO database. It is expected that the magnitude of low-level shear might have an

influence on the raining region within systems, while upper-level shear would influence anvil detrainment and ultimately the convective object extent. Angela also noted that even between the East and West Atlantic Ocean, systems looked vastly different. It will be interesting to study how these relationships vary between the East and West Atlantic, and how they differ from the West Pacific where convection is so prevalent.

6.2.5 Post-Graduate Plans

I will be starting a post-doc position at Columbia University and NASA GISS beginning in January 2024. I will be working with Greg Cesana to characterize different types of high clouds (e.g. stratiform and cumuliform) using satellite observations from CERES, CloudSat, and CALIPSO. Additionally, I will be calculating their short-term and long-term cloud feedbacks with the goal of using these constraints to evaluate climate models.

I have also been asked to co-organize a NASA(AOS)-INCUS-GEWEX convection cloud tracking workshop to be held in April 2024 at NASA GISS. It is a follow-on to a workshop in April 2023 that introduced the tobac tracking algorithm that was initiated between scientists at CSU and Oxford. The goal of this upcoming workshop will be to highlight key strengths and weaknesses from all of the cloud tracking algorithms that are currently underway, with a particular focus on bridging convective cloud morphology to environmental influences that could help apply physical reasoning to convective organization indices. Hopefully this experience will not only help with my present cloud tracking analysis, but will also increase my understanding on the coupled interactions between tropical convection and the local and large-scale dynamic and thermodynamic environments.

Appendix A

Supplemental Figures

A.1   Supplemental Figures for Chapter 4

Supplemental Figure A.2a shows the expected monthly counts of convective cores (black) and hot towers (red) at 1330 LST. The expected monthly counts are calculated by taking the number of cores (hot towers), dividing them by the number of orbits for that month that are stored in the database, and multiplying by the expected number of orbits per month assuming that CloudSat and CALIPSO were operational for every flyover between 2006-2016. The expected number of orbits per month is defined by multiplying the approximate number of CloudSat revolutions per day, which is 14.6, by the average number of days in a month (30 days). The months where there were fewer than 100 cores and/or flyovers detected are masked to ensure a representative timeseries.
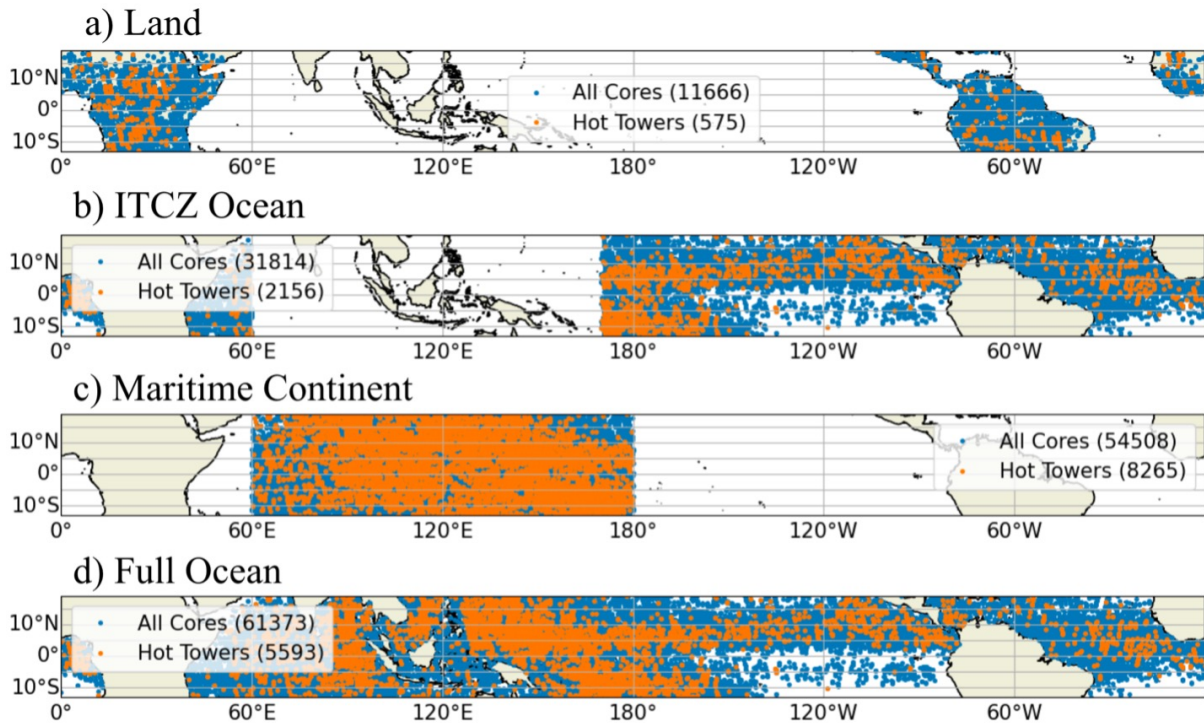
FIGURE A.1: Locations of CloudSat-detected cores (blue dots) and *hot towers* (orange dots) over (a) land, (b) ITCZ ocean, (c) Maritime Continent, and (d) the full ocean between January 2007 - December 2010 and January 2012 - December 2016.

There appears to be a seasonal cycle in the frequency of convective cores, as there generally are minima in core activity between December to February of each year with a corresponding maxima around September or October. The amplitudes in the frequency of hot towers generally follow the overall convective core activity; however, the dominant peaks in hot tower activity are in the later half of each year, which is also evident in Figure 8b. Supplemental Figure 1b shows that the seasonal cycle of both rain rates and OLR follow that of convective core frequency as they consistently are at a minimum at the beginning of each year over the course of the 10 year period. Conversely, both rain rates and core frequency peak in the middle to the end of each year. The anomalous peaks in core frequency in 2013 correspond to a slight increase in the precipitation trend
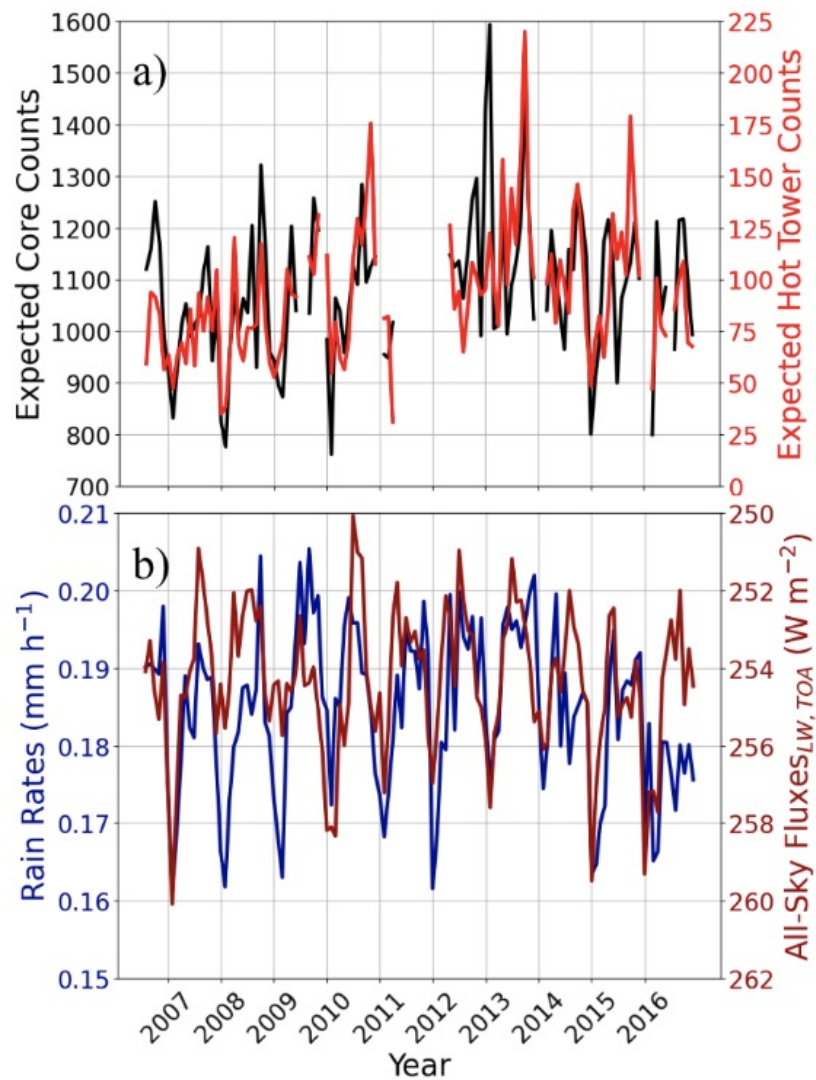
FIGURE A.2: (a) Expected core (black) and hot tower (red) counts at 1330 LST per month between August 2006 - December 2016. Data is masked when there are less than 100 counts or CloudSat granules in a month. (b) Monthly mean GPM IMERG rain rates (dark blue) and CERES EBAF all-sky TOA LW fluxes (dark red) averaged over the full TTZ between August 2006 - December 2016. The y-axis is inverted for the LW fluxes to distinguish whether they are correlated to rain rates.

mean rain rate and a potential deepening of clouds.

A.2 Supplemental Figures for Chapter 5
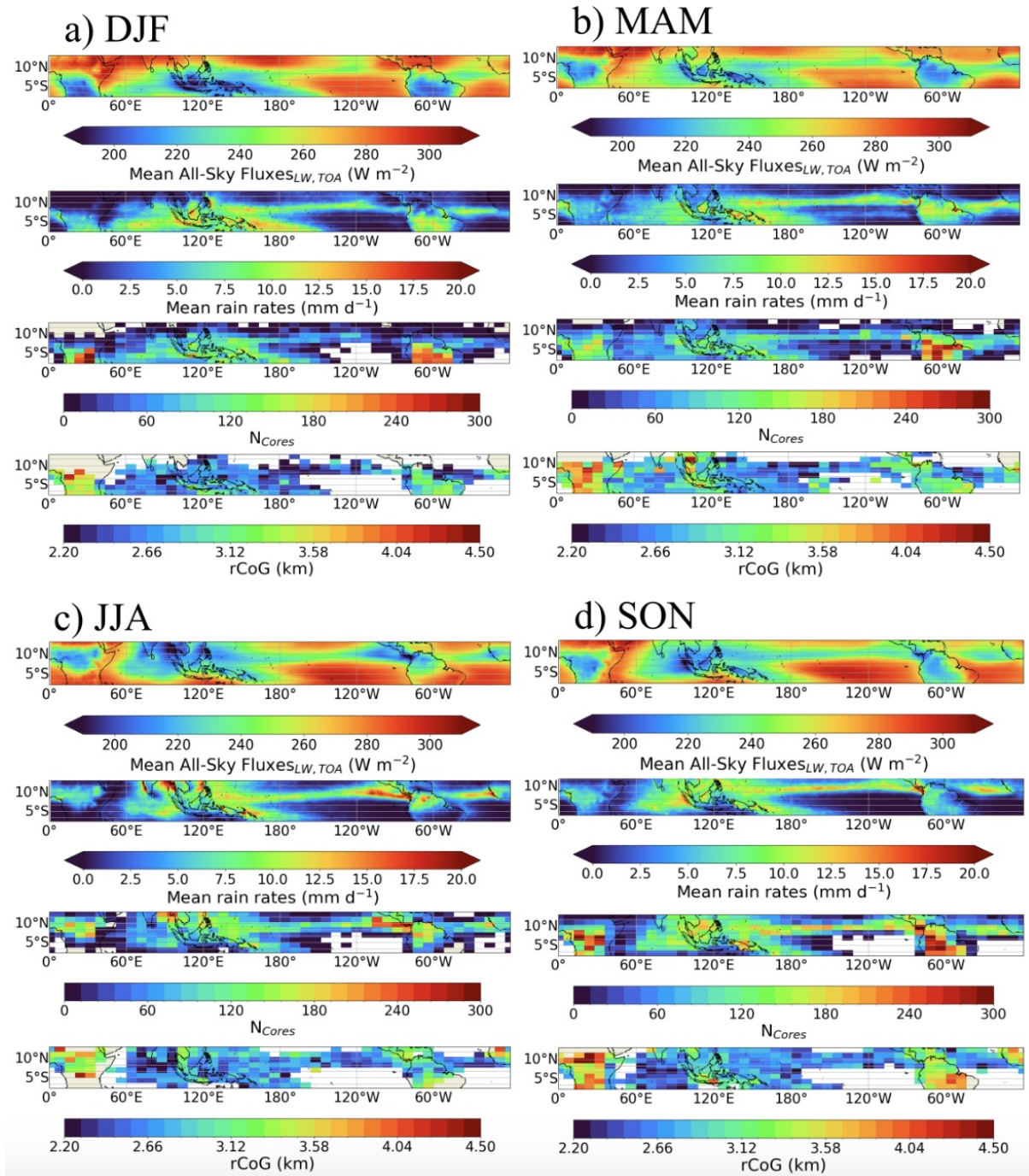
FIGURE A.3: Mean outgoing longwave radiation (first), mean rain rates (second), number of convective cores (third), and mean rCoG (last) between January 2007-December 2010 and January 2012-December 2016 sorted by seasons: (a) December, January, February (DJF); (b) March, April, May (MAM); (c) June, July, August (JJA); and (d) September, October, November (SON). At least 20 cores or *hot towers* are required in each grid box for mean rCoG to be calculated.
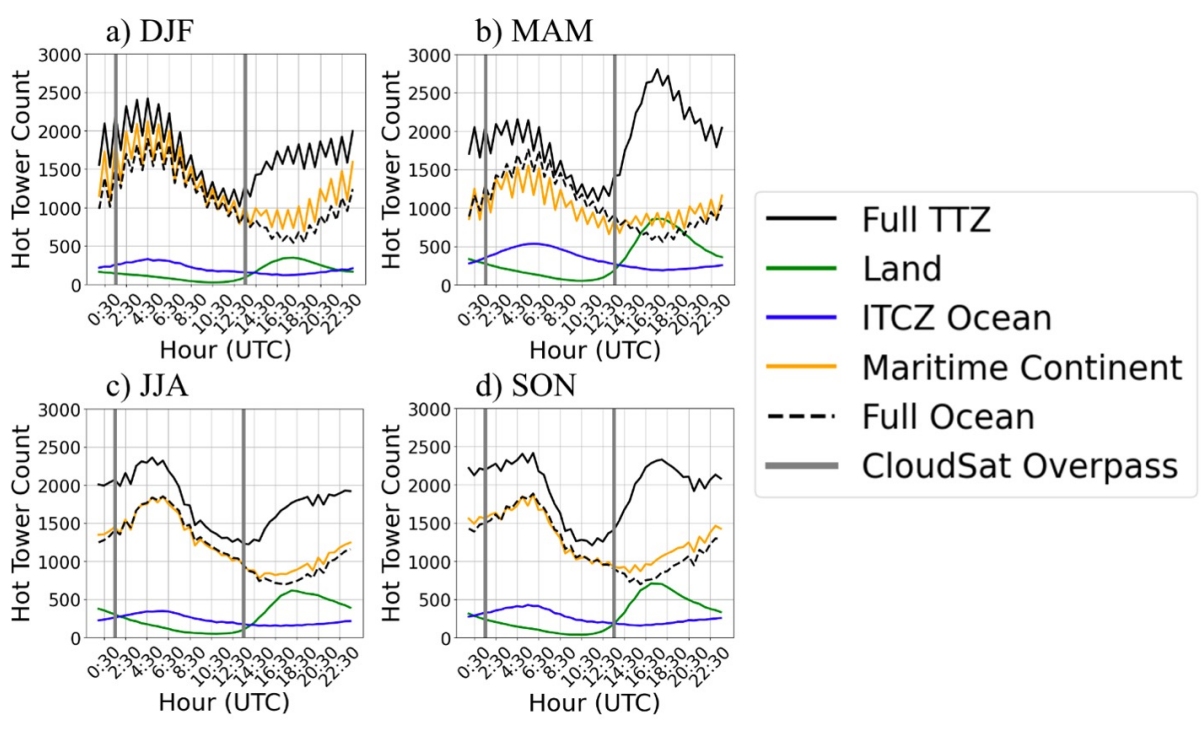
FIGURE A.4: Like Figure 4.9b, but sorted by season: (a) December, January, February (DJF), (b) March, April, May (MAM), (c) June, July, August (JJA), and (d) September, October, November (SON)..
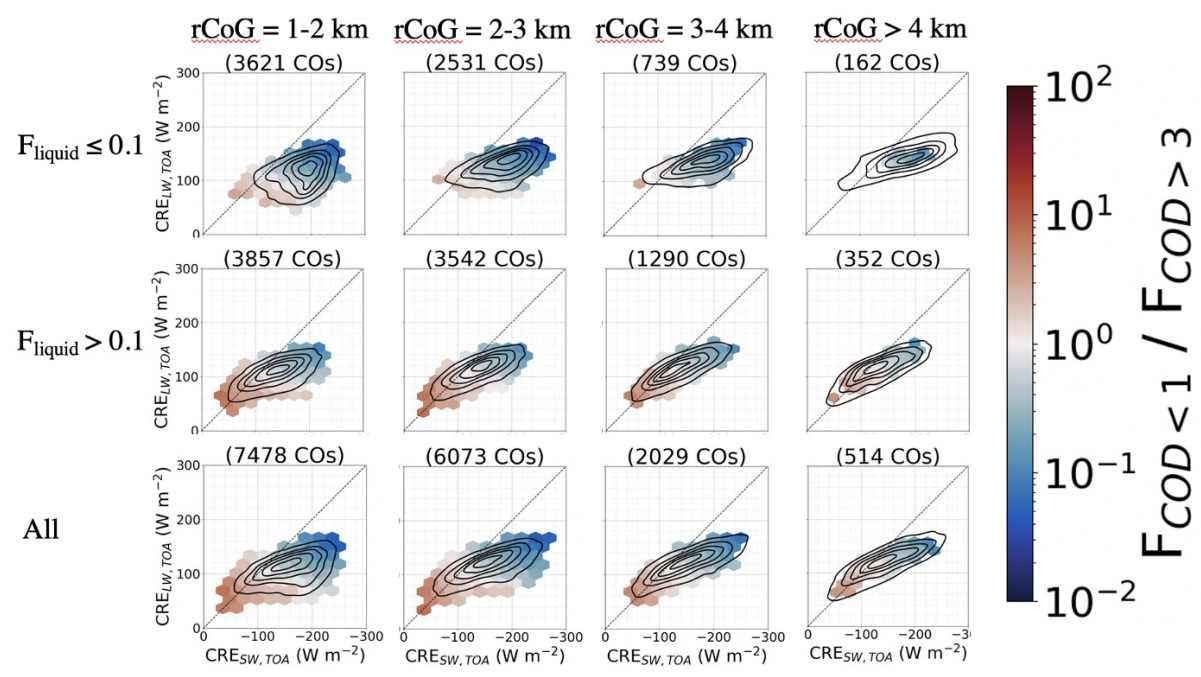
FIGURE A.5: Like Figure 5.9 but for multi-cell systems.
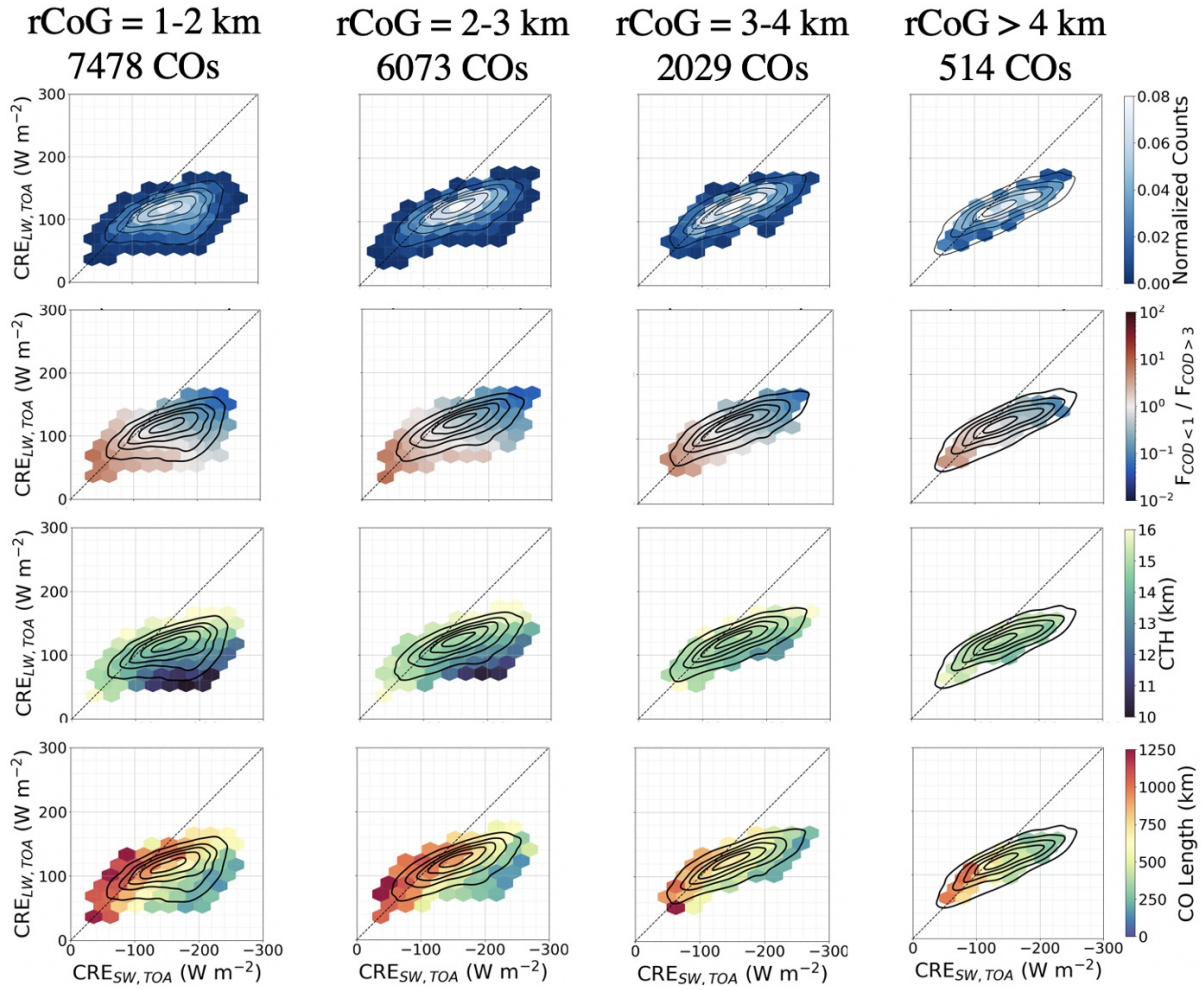
FIGURE A.6: Like Figure 5.10 but for multi-cell systems.
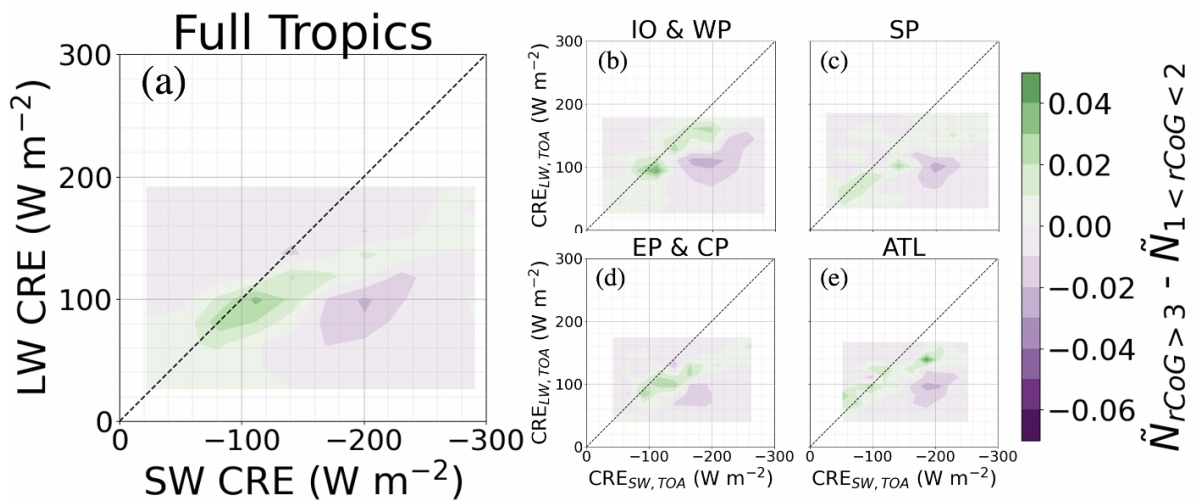
FIGURE A.7: Like Figure 5.11 but for multi-cell systems.

Bibliography

Allen, M. R. and W. J. Ingram, 2002: Constraints on future changes in climate and the hydrologic cycle. *Nature*, **419**, 228–232, doi:10.1038/nature01092.

Arnold, N. P. and D. A. Randall, 2015: Global-scale convective aggregation: Implications for the Madden-Julian Oscillation. *Journal of Advances in Modeling Earth Systems*, **7**, 1499–1518, doi:10.1002/2015MS000498.

Back, L. E. and C. S. Bretherton, 2006: Geographic variability in the export of moist static energy and vertical motion profiles in the tropical pacific. *Geophysical Research Letters*, **33**, doi:https://doi.org/10.1029/2006GL026672.

Bacmeister, J. T. and G. L. Stephens, 2011: Spatial statistics of likely convective clouds in CloudSat data. *J. Geophys. Res*, **116**, 4104, doi:10.1029/2010JD014444.

Battaglia, A., J. M. Haynes, T. L'Ecuyer, and C. Simmer, 2008: Identifying multiple-scattering-affected profiles in CloudSat observations over the oceans. *J. Geophys. Res. Atmos.*, **113**, doi:https://doi.org/10.1029/2008JD009960.

Bedka, K., J. Brunner, R. Dworak, W. Feltz, J. Otkin, and T. Greenwald, 2010: Objective Satellite-Based Detection of Overshooting Tops Using Infrared Window Channel Brightness Temperature Gradients. *Journal of Applied Meteorology and Climatology*, **49**, 181–202, doi:10.1175/2009JAMC2286.1.

Bell, G. D., M. S. Halpert, R. C. Schnell, R. W. Higgins, J. Lawrimore, V. E. Kousky, R. Tinker, W. Thiaw, M. Chelliah, and A. Artusa, 2000: Climate assessment for 1999. *Bulletin of the American Meteorological Society*, **81**, S1 – S50, doi:https://doi.org/10.1175/1520-0477(2000)81[s1:CAF]2.0.CO;2.

Berg, W., T. L'Ecuyer, and C. Kummerow, 2006: Rainfall Climate Regimes: The Relationship of Regional TRMM Rainfall Biases to the Environment. *J. Appl. Meteorol. Climatol.*, **45**, 434–454, doi:10.1175/JAM2331.1.

Bony, S., R. Colman, V. M. Kattsov, R. P. Allan, C. S. Bretherton, J.-L. Dufresne, A. Hall, S. Hallegatte, M. M. Holland, and W. Ingram, 2006: How Well Do We Understand and Evaluate Climate Change Feedback Processes? *Journal of Climate*, **19**, 3445, doi:10.1175/JCLI3819.1.

Bony, S., J.-L. Dufresne, H. Le Treut, J.-J. Morcrette, and C. Senior, 2004: On dynamic and thermodynamic components of cloud changes. *Climate Dynamics*, **22**, 71–86, doi:10.1007/s00382-003-0369-6.

Bony, S., K.-M. Lau, and Y. C. Sud, 1997: Sea surface temperature and large-scale circulation influences on tropical greenhouse effect and cloud radiative forcing. *Journal of Climate*, **10**, 2055–2077, doi:10.1175/1520-0442(1997)010<2055:SSTALS>2.0.CO;2.

Bony, S., B. Stevens, D. Coppin, T. Becker, K. A. Reed, A. Voigt, and B. Medeiros, 2016: Thermodynamic control of anvil cloud amount. *Proceedings of the National Academy of Science*, **113**, 8927–8932, doi:10.1073/pnas.1601472113.

Bony, S., B. Stevens, D. M. W. Frierson, C. Jakob, M. Kageyama, R. Pincus, T. G. Shepherd, S. C. Sherwood, A. P. Siebesma, A. H. Sobel, M. Watanabe, and M. J. Webb, 2015: Clouds, circulation and climate sensitivity. *Nature Geoscience*, **8**, 261–268, doi:10.1038/ngeo2398.

Bretherton, C. S., P. N. Blossey, and M. Khairoutdinov, 2005: An Energy-Balance Analysis of Deep Convective Self-Aggregation above Uniform SST. *Journal of the Atmospheric Sciences*, **62**, 4273–4292, doi:10.1175/JAS3614.1.

Bretherton, C. S. and D. Hartmann, 2009: Large-scale controls on cloudiness. *Clouds in the Perturbed Climate System: Their Relationship to Energy Balance, Atmospheric Dynamics, and Precipitation*, doi:10.7551/mitpress/9780262012874.003.0010.

Brueck, M., C. Hohenegger, and B. Stevens, 2020: Mesoscale marine tropical precipitation varies independently from the spatial arrangement of its convective cells. *Q. J. R. Meteorol. Soc.*, **146**, 1391–1402, doi:10.1002/qj.3742.

Burzynski, A. and P. Partain, 2022: Amsr2-aux data set. Technical report, CloudSat Data Processing Center Cooperative Institute for Research in the Atmosphere, Fort Collins, Colorado USA.

Byers, H. R. and R. R. Braham, 1948: THUNDERSTORM STRUCTURE AND CIRCULATION. *J. Atmos. Sci.*, **5**, 71–86, doi:https://doi.org/10.1175/1520-0469(1948)005<0071:TSAC>2.0.CO;2.

Byrne, M. P., A. G. Pendergrass, A. D. Rapp, and K. R. Wodzicki, 2018: Response of the intertropical convergence zone to climate change: Location, width, and strength. *Current Climate Change Reports*, **4**, 355–370, doi:10.1007/s40641-018-0110-5.

Camargo, S. J. and A. H. Sobel, 2005: Western north pacific tropical cyclone intensity and enso. *Journal of Climate*, **18**, 2996 – 3006, doi:https://doi.org/10.1175/JCLI3457.1.

Chen, J., B. E. Carlson, and A. D. Del Genio, 2002: Evidence for strengthening of the tropical general circulation in the 1990s. *Science*, **295**, 838–841, doi:10.1126/science.1065835.

Chen, S. S. and R. A. Houze Jr, 1997: Diurnal variation and life-cycle of deep convective systems over the tropical pacific warm pool. *Quarterly Journal of the Royal Meteorological Society*, **123**, 357–388, doi:https://doi.org/10.1002/qj.49712353806.

Cheng, K.-Y., L. Harris, C. Bretherton, T. M. Merlis, M. Bolot, L. Zhou, A. Kaltenbaugh, S. Clark, and S. Fueglistaler, 2022: Impact of Warmer Sea Surface Temperature on the Global Pattern of Intense Convection: Insights From a Global Storm Resolving Model. *Geophys. Res. Lett.*, **49**, e2022GL099796, doi:https://doi.org/10.1029/2022GL099796.

Cifelli, R., S. W. Nesbitt, S. A. Rutledge, W. A. Petersen, and S. Yuter, 2007: Radar characteristics of precipitation features in the EPIC and TEPPS regions of the East Pacific. *Mon. Weather Rev.*, **135**, 1576–1595, doi:10.1175/MWR3340.1.

Cifelli, R., S. W. Nesbitt, S. A. Rutledge, W. A. Petersen, S. Yuter, and R. Cifelli, 2008: Diurnal Characteristics of Precipitation Features over the Tropical East Pacific: A Comparison of the EPIC and TEPPS Regions. *Journal of Climate*, **21**, doi:10.1175/2007JCLI2020.1.

Clement, A. C. and B. Soden, 2005: The sensitivity of the tropical-mean radiation budget. *Journal of Climate*, **18**, 3189–3203, doi:10.1175/JCLI3456.1.

Coppin, D. and S. Bony, 2015: Physical mechanisms controlling the initiation of convective self-aggregation in a general circulation model. *Journal of Advances in Modeling Earth Systems*, **7**, 2060–2078, doi:10.1002/2015MS000571.

Cronk, H. and P. Partain, 2018: Cloudsat mod06-aux auxiliary data set. Technical report, CloudSat Data Processing Center Cooperative Institute for Research in the Atmosphere, Fort Collins, Colorado USA.

Del Genio, A. D. and W. Kovari, 2002: Climatic properties of tropical precipitating convection under varying environmental conditions. *J. Climate*, **15**, 2597–2615, doi:10.1175/1520-0442(2002)015

Deng, M., G. G. Mace, and Z. Wang, 2016: Anvil productivities of tropical deep convective clusters and their regional differences. *J. Atmos. Sci.*, **73**, 3467–3487, doi:10.1175/JAS-D-15-0239.1.

Deng, M., G. G. Mace, Z. Wang, and R. P. Lawson, 2013: Evaluation of Several A-Train Ice Cloud Retrieval Products with In Situ Measurements Collected during the SPARTICUS Campaign. *J. Appl. Meteorol. Climatol.*, **52**, 1014–1030, doi:https://doi.org/10.1175/JAMC-D-12-054.1.

Deng, M., G. G. Mace, Z. Wang, and H. Okamoto, 2010: Tropical Composition, Cloud and Climate Coupling Experiment validation for cirrus cloud profiling retrieval using CloudSat radar and CALIPSO lidar. *J. Geophys. Res. Atmos.*, **115**, doi:https://doi.org/10.1029/2009JD013104.

Derras-Chouk, A. and Z. J. Luo, submitted: Revisiting riehl and malkus (1958) and riehl and simpson (1979): Characterizing tropical hot towers and estimating convective mass fluxes using geostationary satellite data. *Survey of Geophysics*.

Dessler, A. E., 2013: Observations of Climate Feedbacks over 2000–10 and Comparisons to Climate Models. *Journal of Climate*, **26**, 333–342, doi:10.1175/JCLI-D-11-00640.1.

Diffenbaugh, N. S., M. Scherer, and R. J. Trapp, 2013: Robust increases in severe thunderstorm environments in response to greenhouse forcing. *Proc. Natl. Acad. Sci.*, **110**, 16361–16366, doi:10.1073/pnas.1307758110.

Doswell, C. A., 2001: *Severe Convective Storms—An Overview*, American Meteorological Society, Boston, MA, chapter 1. 1–26.

Easterling, D. R. and P. J. Robinson, 1985: The Diurnal Variation of Thunderstorm Activity in the United States. *J. Appl. Meteorol. Climatol.*, **24**, 1048–1058, doi:10.1175/1520-0450(1985)024<1048:TDVOTA>2.0.CO;2.

Elsaesser, G., R. Roca, T. Fiolleau, A. D. Del Genio, and J. Wu, 2022: A simple model for tropical convective cloud shield area growth and decay rates informed by geostationary ir, gpm, and aqua/airs satellite data. *J. Geophys. Res. Atmos.*, **127**, e2021JD035599, doi:10.1029/2021JD035599.

Emanuel, K. A., 1994: *Atmospheric convection*. Oxford University Press.

Feng, Z., S. Hagos, A. K. Rowe, C. D. Burleyson, M. N. Martini, and d. S. S. P., 2015: Mechanisms of convective cloud organization by cold pools over tropical warm ocean during the AMIE/DYNAMO field campaign. *J. Adv. Model. Earth Syst.*, **7**, 513–526, doi:10.1002/2015MS000470.Received.

Fierro, A. O., J. Simpson, M. A. LeMone, J. M. Straka, and B. F. Smull, 2009: On How Hot Towers Fuel the Hadley Cell: An Observational and Modeling Study of Line-Organized Convection in the Equatorial Trough from TOGA COARE. *J. Atmos. Sci.*, **66**, 2730–2746, doi:https://doi.org/10.1175/2009JAS3017.1.

Fiolleau, T. and R. Roca, 2013: An Algorithm for the Detection and Tracking of Tropical Mesoscale Convective Systems Using Infrared Images From Geostationary Satellite. *IEEE Trans. Geosci. Remote Sens.*, **51**, 4302–4315, doi:10.1109/TGRS.2012.2227762.

Forster, P., T. Storelvmo, K. Armour, W. Collins, J.-L. Dufresne, D. Frame, D. Lunt, T. Mauritsen, M. Palmer, M. Watanabe, M. Wild, and H. Zhang, 2021: *2021: The Earth's Energy Budget, Climate Feedbacks, and Climate Sensitivity*. Cambridge University Press, Cambridge, United Kingdom and New York, NY, USA, 923–1054 pp.

Gasparini, B., S. C. Sullivan, A. B. Sokol, B. Kärcher, E. Jensen, and L. Hartmann, 2023: Opinion : Tropical cirrus — From micro-scale processes to climate-scale impacts. *EGUsphere [preprint]*, 1–47.

Giangrande, S. E., S. Collis, J. Straka, A. Protat, C. Williams, and S. Krueger, 2013: A Summary of Convective-Core Vertical Velocity Properties Using ARM UHF Wind Profilers in Oklahoma. *J. Appl. Meteorol. Climatol.*, **52**, 2278–2295, doi:10.1175/JAMC-D-12-0185.1.

Giangrande, S. E., T. Toto, M. P. Jensen, M. J. Bartholomew, Z. Feng, A. Protat, C. R. Williams, C. Schumacher, and L. Machado, 2016: Convective cloud vertical velocity and mass-flux characteristics from radar wind profiler observations during goamazon2014/5. *Journal of Geophysical Research: Atmospheres*, **121**, 12,891–12,913, doi:https://doi.org/10.1002/2016JD025303.

Gordon, H. B., P. H. Whetton, A. B. Pittock, A. M. Fowler, and M. R. Haylock, 1992: Simulated changes in daily rainfall intensity due to the enhanced greenhouse effect: implications for extreme rainfall events. *Climate Dynamics*, **8**, 83–102, doi:10.1007/BF00209165.

Hamada, A., Y. N. Takayabu, C. Liu, and E. J. Zipser, 2015: Weak linkage between the heaviest rainfall and tallest storms. *Nat. Commun.*, doi:10.1038/ncomms7213.

Harrison, E. F., P. Minnis, B. R. Barkstrom, V. Ramanathan, R. D. Cess, and G. G. Gibson, 1990: Seasonal variation of cloud radiative forcing derived from the Earth Radiation Budget Experiment. *J. Geophys. Res.*, **95**, 18687–18703, doi:10.1029/jd095id11p18687.

Hart, N. C., R. Washington, and R. I. Maidment, 2019: Deep convection over Africa: Annual cycle, ENSO, and trends in the hotspots. *J. Clim.*, **32**, 8791–8811.

Hartmann, D. L. and S. E. Berry, 2017: The balanced radiative effect of tropical anvil clouds. *J. Geophys. Res. Atmos.*, **122**, 5003–5020, doi:https://doi.org/10.1002/2017JD026460.

Hartmann, D. L., B. Gasparini, S. E. Berry, and P. N. Blossey, 2018: The Life Cycle and Net Radiative Effect of Tropical Anvil Clouds. *J. Adv. Model. Earth Syst.*, **10**, 3012–3029, doi:10.1029/2018MS001484.

Hartmann, D. L. and K. Larson, 2002: An important constraint on tropical cloud - climate feedback. *Geophysical Research Letters*, **29**, 249–254, doi:10.1029/2002gl015835.

Hartmann, D. L. and M. L. Michelsen, 2002: No evidence for iris. *Bulletin of the American Meteorological Society*, **83**, 249–254, doi:10.1175/1520-0477(2002)083<0249:NEFI>2.3.CO;2.

Hartmann, D. L., L. A. Moy, and Q. Fu, 2001: Tropical Convection and the Energy Balance at the Top of the Atmosphere. *J. Clim.*, **14**, 4495–4511, doi:https://doi.org/10.1175/1520-0442(2001)014<4495:TCATEB>2.0.CO;2.

Hartmann, D. L., M. E. Ockert-Bell, and M. L. Michelsen, 1992: The Effect of Cloud Type on Earth's Energy Balance: Global Analysis. *J. Clim.*, **5**, 1281–1304, doi:https://doi.org/10.1175/1520-0442(1992)005<1281:TEOCTO>2.0.CO;2.

Hartmann, D. L., V. Ramanathan, A. Berroir, and G. E. Hunt, 1986: Earth Radiation Budget data and climate research. *Rev. Geophys.*, **24**, 439–468, doi:https://doi.org/10.1029/RG024i002p00439.

Haynes, J. M., T. S. L'Ecuyer, G. L. Stephens, S. D. Miller, C. Mitrescu, N. B. Wood, and S. Tanelli, 2009: Rainfall retrieval over the ocean with spaceborne W-band radar. *J. Geophys. Res. Atmos.*, **114**, doi:10.1029/2008JD009973@10.1002/(ISSN)2169-8996.CLOUDSAT1.

Haynes, J. M. and G. L. Stephens, 2007: Tropical oceanic cloudiness and the incidence of precipitation: Early results from CloudSat. *Geophysical Research Letters*, **34**, doi:10.1029/2007GL029335.

Held, I. M. and B. J. Soden, 2006: Robust Responses of the Hydrological Cycle to Global Warming. *Journal of Climate*, **19**, 5686, doi:10.1175/JCLI3990.1.

Henderson, D. and T. L'Ecuyer, 2023: Level 2b fluxes and heating rates with lidar, verson p2 r05. Technical report, Space Science and Engineering Center University of Wisconsin, Madison, Wisconsin USA.

Henderson, D. S., T. L'Ecuyer, G. Stephens, P. Partain, and M. Sekiguchi, 2013: A multisensor perspective on the radiative impacts of clouds and aerosols. *Journal of Applied Meteorology and Climatology*, **52**, 853–871, doi:10.1175/JAMC-D-12-025.1.

Heymsfield, G. M., B. Geerts, and L. Tian, 2000: TRMM Precipitation Radar Reflectivity Profiles as Compared with High-Resolution Airborne and Ground-Based Radar Measurements. *J. Appl. Meteorol.*, **39**, 2080–2102, doi:10.1175/1520-0450(2001)040<2080:TPRRPA>2.0.CO;2.

Heymsfield, G. M., L. Tian, A. J. Heymsfield, L. Li, and S. Guimond, 2010: Characteristics of Deep Tropical and Subtropical Convection from Nadir-Viewing High-Altitude Airborne Doppler Radar. *J. Atmos. Sci.*, **67**, 285–308, doi:https://doi.org/10.1175/2009JAS3132.1.

Hinkelman, L. M. and R. Marchand, 2020: Evaluation of ceres and cloudsat surface radiative fluxes over macquarie island, the southern ocean. *Earth and Space Science*, **7**, e2020EA001224, doi:https://doi.org/10.1029/2020EA001224.

Höjgård-Olsen, E., H. Chepfer, and H. Brogniez, 2022: Satellite Observed Sensitivity of Tropical Clouds and Moisture to Sea Surface Temperature on Various Time and Space Scales: 1. Focus on High Level Cloud Situations Over Ocean. *J. Geophys. Res. Atmos.*, **127**, doi:10.1029/2021JD035438.

Holloway, C. E., A. A. Wing, S. Bony, C. Muller, H. Masunaga, T. S. L'Ecuyer, D. D. Turner, and P. Zuidema, 2017: Observing Convective Aggregation. *Surveys in Geophysics*, **38**, 1199–1236, doi:10.1007/s10712-017-9419-1.

Hou, A. Y., R. K. Kakar, S. Neeck, A. A. Azarbarzin, C. D. Kummerow, M. Kojima, R. Oki, K. Nakamura, and T. Iguchi, 2014: The Global Precipitation Measurement Mission. *Bull. Am. Meteorol. Soc.*, **95**, 701–722, doi:10.1175/BAMS-D-13-00164.1.

Houze, R. A., 1997: Stratiform precipitation in regions of convection: A meteorological paradox? *Bulletin of the American Meteorological Society*, **78**, 2179 – 2196, doi:https://doi.org/10.1175/1520-0477(1997)078<2179:SPIROC>2.0.CO;2.

Houze Jr., R. A., 1977: Structure and Dynamics of a Tropical Squall-Line System. *Mon. Weather Rev.*, **105**, 1540–1567.

Houze Jr., R. A., 1981: Structures of atmospheric precipitation systems: A global survey. *Radio Science*, **16**, 671–689, doi:https://doi.org/10.1029/RS016i005p00671.

— 1982: Cloud clusters and large-scale vertical motions in the tropics. *Journal of the Meteorological Society of Japan. Ser. II*, **60**, 396–410, doi:10.2151/jmsj1965.60.1_396.

Hu, X., J. Ge, W. Li, J. Du, Q. Li, and Q. Mu, 2021: Vertical Structure of Tropical Deep Convective Systems at Different Life Stages From CloudSat Observations. *J. Geophys. Res. Atmos.*, **126**, doi:https://doi.org/10.1029/2021JD035115.

Huffman, G. J., D. T. Bolvin, D. Braithwaite, K.-L. Hsu, R. J. Joyce, C. Kidd, E. J. Nelkin, S. Sorooshian, E. F. Stocker, J. Tan, D. B. Wolff, and P. Xie, 2020: *Integrated Multi-satellite Retrievals for the Global Precipitation Measurement (GPM) Mission (IMERG)*, Springer International Publishing, Cham. 343–353.

Igel, M. R., A. J. Drager, and S. C. van den Heever, 2014: CloudSat cloud object partitioning technique and assessment and integration of deep conevctive anvil sensitivities to SST. *Journal of Geophysical Research : Atmospheres*, **119**, 515–535, doi:10.1002/2014JD021717.Received.

Igel, M. R. and S. C. van den Heever, 2015a: The relative influence of environmental characteristics on tropical deep convective morphology as observed by CloudSat. *J. Geophys. Res.*, **120**, 4304–4322.

— 2015b: Tropical, oceanic, deep convective cloud morphology as observed by cloudsat.

Iguchi, T., N. Kawamoto, and R. Oki, 2018: Detection of Intense Ice Precipitation with GPM/DPR. *J. Atmos. Ocean. Technol.*, **35**, 491–502, doi:10.1175/JTECH-D-17-0120.1.

Iguchi, T., T. Kozu, R. Meneghini, J. Awaka, and K. Okamoto, 2000: Rain-Profiling Algorithm for the TRMM Precipitation Radar. *J. Appl. Meteorol.*, **39**, 2038–2052, doi:10.1175/1520-0450(2001)040<2038:RPAFTT>2.0.CO;2.

IPCC, 2023: *Climate Change 2023: Synthesis Report*. Contribution of Working Groups I, II and III to the Sixth Assessment Report of the Intergovernmental Panel on Climate Change [Core Writing Team, H. Lee and J. Romero (eds.)], Geneva, Switzerland, 35-115 pp.

URL https://www.ipcc.ch/report/ar6/syr/downloads/report/IPCC_AR6_SYR_
LongerReport.pdf

Ito, M. and H. Masunaga, 2022: Process-Level Assessment of the Iris Effect Over Tropical Oceans. *Geophysical Research Letters*, **49**, doi:10.1029/2022GL097997.

Janowiak, J., B. Joyce, and P. Xie, 2017: Ncep/cpc l3 half hourly 4km global (60s - 60n) merged ir v1. Technical report, Goddard Earth Sciences Data and Information Services Center (GES DISC), Greenbelt, MD.

Jensen, M. P., W. A. Petersen, A. Bansemer, N. Bharadwaj, L. D. Carey, D. J. Cecil, S. M. Collis, A. D. Del Genio, B. Dolan, J. Gerlach, S. E. Giangrande, A. Heymsfield, G. Heymsfield, P. Kollias, T. J. Lang, S. W. Nesbitt, A. Neumann, M. Poellot, S. A. Rutledge, M. Schwaller, A. Tokay, C. R. Williams, D. B. Wolff, S. Xie, and E. J. Zipser, 2016: THE MIDLATITUDE CONTINENTAL CONVECTIVE CLOUDS EXPERIMENT (MC3E). *Bull. Am. Meteorol. Soc.*, **97**, 1667–1686, doi:10.1175/BAMS-D-14-00228.1.

Johnson, R. H., T. M. Rickenbach, S. A. Rutledge, P. E. Ciesielski, and W. H. Schubert, 1999: Trimodal characteristics of tropical convection. *Journal of Climate*, **12**, 2397–2418, doi:10.1175/1520-0442(1999)012<2397:tcotc>2.0.co;2.

Kadoya, T. and H. Masunaga, 2018: New observational metrics of convective self-aggregation: Methodology and a case study. *Journal of the Meteorological Society of Japan*, **96**, 535–548.

Kiehl, J. T., 1994: Clouds and Their Effects on the Climate System. *Phys. Today*, **47**, 36–42, doi:10.1063/1.881424.

Kiehl, J. T. and V. Ramanathan, 1990: Comparison of cloud forcing derived from the Earth Radiation Budget Experiment with that simulated by the NCAR community climate model. *J. Geophys. Res. Atmos.*, **95**, 11679–11698, doi:https://doi.org/10.1029/JD095iD08p11679.

Koren, I., O. Altaratz, G. Feingold, Z. Levin, and T. Reisin, 2009: Cloud's Center of Gravity – a compact approach to analyze convective cloud development. *Atmos. Chem. Phys.*, **9**, 155–161.

Kubar, T. L. and J. H. Jiang, 2019: Net Cloud Thinning, Low-Level Cloud Diminishment, and Hadley Circulation Weakening of Precipitating Clouds with Tropical West Pacific SST Using MISR and Other Satellite and Reanalysis Data. *Remote Sens.*, **11**, doi:10.3390/rs11101250.

Kummerow, C., P. J. Brown, R. Ferraro, and D. Randel, 2021a: Amsr-e/aqua l2b global swath surface precipitation gsfc profiling algorithm, version 4.

Kummerow, C., R. Ferraro, and D. Duncan, 2021b: Amsr-e/amsr2 unified l2b global swath ocean products, version 1. Technical report, NASA National Snow and Ice Data Center Distributed Active Archive Center, Boulder, Colorado USA.

Kummerow, C., R. Ferraro, and D. Randel, 2020: Amsr-e/amsr2 unified l2b global swath surface precipitation, version 1. Technical report, NASA National Snow and Ice Data Center Distributed Active Archive Center, Boulder, Colorado USA.

Kummerow, C., Y. Hong, W. S. Olson, S. Yang, R. F. Adler, J. McCollum, R. Ferraro, G. Petty, D.-B. Shin, and T. T. Wilheit, 2001: The evolution of the Goddard profiling algorithm (GPROF) for rainfall estimation from passive microwave sensors. *J. Appl. Meteorol.*, **40**, 1801–1820.

Laing, A. G., R. E. Carbone, and V. Levizzani, 2011: Cycles and propagation of deep convection over equatorial Africa. *Mon. Weather Rev.*, **139**, 2832–2853, doi:10.1175/2011MWR3500.1.

Lebsock, M. D., C. Kummerow, and G. L. Stephens, 2010: An observed tropical oceanic radiative–convective cloud feedback. *Journal of Climate*, **23**, 2065 – 2078, doi:10.1175/2009JCLI3091.1.

L'Ecuyer, T. S. and J. H. Jiang, 2010: Touring the atmosphere aboard the A-Train A convoy of satellites orbiting Earth measures cloud properties, greenhouse gas concentrations, and more to provide a multifaceted perspective on the processes that affect climate. *Physics Today*, **63**, 36–41.

L'Ecuyer, T. S. and G. L. Stephens, 2002: An uncertainty model for Bayesian Monte Carlo retrieval algorithms: Application to the TRMM observing system. *Q. J. R. Meteorol. Soc.*, **128**, 1713–1737.

L'Ecuyer, T. S., N. B. Wood, T. Haladay, G. L. Stephens, and P. W. Stackhouse Jr., 2008: Impact of clouds on atmospheric heating based on the r04 cloudsat fluxes and heating rates data set. *Journal of Geophysical Research: Atmospheres*, **113**, doi:10.1029/2008JD009951.

LeMone, M. A. and E. J. Zipser, 1980: Cumulonimbus Vertical Velocity Events in GATE. Part I: Diameter, Intensity and Mass Flux. *J. Atmos. Sci.*, **37**, 2444–2457, doi:10.1175/1520-0469(1980)037<2444:CVVEIG>2.0.CO;2.

Li, R. L., J. H. Studholme, A. V. Fedorov, and T. Storelvmo, 2022: Precipitation efficiency constraint on climate change. *Nature Climate Change*, **12**, 642–648, doi:10.1038/s41558-022-01400-x.

Li, W. and C. Schumacher, 2011: Thick Anvils as Viewed by the TRMM Precipitation Radar. *J. Clim.*, **24**, 1718–1735, doi:https://doi.org/10.1175/2010JCLI3793.1.

Li, Y., D. W. J. Thompson, G. L. Stephens, and S. Bony, 2014: A global survey of the instantaneous linkages between cloud vertical structure and large-scale climate. *Journal of Geophysical Research (Atmospheres)*, **119**, 3770–3792, doi:10.1002/2013JD020669.

Lin, B., B. A. Wielicki, L. H. Chambers, Y. Hu, and K.-M. Xu, 2002: The Iris Hypothesis: A Negative or Positive Cloud Feedback?. *Journal of Climate*, **15**, 3–7, doi:10.1175/1520-0442(2002)015<0003:TIHANO>2.0.CO;2.

Lindzen, R. S., M. D. Chou, and A. Y. Hou, 2001: Does the Earth Have an Adaptive Infrared Iris? *Bull. Am. Meteorol. Soc.*, **82**, 417–432, doi:10.1175/1520-0477(2001)082<0417:DTEHAA>2.3.CO;2.

Liu, C. and E. Zipser, 2013: Regional variation of morphology of organized convection in the tropics and subtropics. *Journal of Geophysical Research (Atmospheres)*, **118**, 453–466, doi:10.1029/2012JD018409.

Liu, C. and E. J. Zipser, 2005: Global distribution of convection penetrating the tropical tropopause. *Journal of Geophysical Research (Atmospheres)*, **110**, 1–12, doi:10.1029/2005JD006063.

Liu, C. and E. J. Zipser, 2008: Diurnal cycles of precipitation, clouds, and lightning in the tropics from 9 years of TRMM observations. *Geophysical Research Letters*, doi:10.1029/2007GL032437.

Liu, C., E. J. Zipser, D. J. Cecil, S. W. Nesbitt, and S. Sherwood, 2008a: A Cloud and Precipitation Feature Database from Nine Years of TRMM Observations. *Source J. Appl. Meteorol. Climatol.*, **47**, 2712–2728, doi:10.2307/26172764.

Liu, C., E. J. Zipser, G. G. Mace, and S. Benson, 2008b: Implications of the differences between daytime and nighttime CloudSat observations over the tropics. *Journal of Geophysical Research: Atmospheres*, **113**, doi:10.1029/2008JD009783.

Liu, C., E. J. Zipser, and S. W. Nesbitt, 2007: Global Distribution of Tropical Deep Convection: Different Perspectives from TRMM Infrared and Radar Data. *Journal of Climate*, **20**, 489, doi:10.1175/JCLI4023.1.

Liu, R., K.-N. Liou, H. Su, Y. Gu, B. Zhao, J. H. Jiang, and S. C. Liu, 2017: High cloud variations with surface temperature from 2002 to 2015: Contributions to atmospheric radiative cooling rate and precipitation changes. *Journal of Geophysical Research (Atmospheres)*, **122**, 5457–5471, doi:10.1002/2016JD026303.

Loeb, N. G., D. R. Doelling, H. Wang, W. Su, C. Nguyen, J. G. Corbett, L. Liang, C. Mitrescu, F. G. Rose, and S. Kato, 2018: Clouds and the earth's radiant energy system (ceres) energy balanced and filled (ebaf) top-of-atmosphere (toa) edition-4.0 data product. *Journal of Climate*, **31**, 895 – 918, doi:https://doi.org/10.1175/JCLI-D-17-0208.1.

Lu, D. and B. Yong, 2018: Evaluation and hydrological utility of the latest gpm imerg v5 and gsmap v7 precipitation products over the tibetan plateau. *Remote Sensing*, **10**, doi:10.3390/rs10122022.

Lucas, C., E. J. Zipser, and M. A. Lemone, 1994: Vertical Velocity in Oceanic Convection off Tropical Australia. *J. Atmos. Sci.*, **51**, 3183–3193, doi:https://doi.org/10.1175/1520-0469(1994)051<3183:VVIOCO>2.0.CO;2.

Luo, Z., G. Y. Liu, and G. L. Stephens, 2008a: CloudSat adding new insight into tropical penetrating convection. *Geophysical Research Letters*, **35**, L19819, doi:10.1029/2008GL035330.

Luo, Z., G. Y. Liu, G. L. Stephens, and R. H. Johnson, 2009: Terminal versus transient cumulus congestus: A CloudSat perspective. *Geophysical Research Letters*, **36**, L05808, doi:10.1029/2008GL036927.

Luo, Z., G. L. Stephens, K. A. Emanuel, D. G. Vane, N. D. Tourville, and J. M. Haynes, 2008b: On the Use of CloudSat and MODIS Data for Estimating Hurricane Intensity. *IEEE GEOSCIENCE AND REMOTE SENSING LETTERS*, **5**, 13, doi:10.1109/LGRS.2007.905341.

Luo, Z. J., J. Jeyaratnam, S. Iwasaki, H. Takahashi, and R. Anderson, 2014: Convective vertical velocity and cloud internal vertical structure: An a-train perspective. *Geophysical Research Letters*, **41**, 723–729, doi:https://doi.org/10.1002/2013GL058922.

Luo, Z. J., G. Y. Liu, and G. L. Stephens, 2010: Use of a-train data to estimate convective buoyancy and entrainment rate. *Geophysical Research Letters*, **37**, doi:https://doi.org/10.1029/2010GL042904.

L'Ecuyer, T. S., H. K. Beaudoing, M. Rodell, W. Olson, B. Lin, S. Kato, C. A. Clayson, E. Wood, J. Sheffield, R. Adler, G. Huffman, M. Bosilovich, G. Gu, F. Robertson, P. R. Houser, D. Chambers, J. S. Famiglietti, E. Fetzer, W. T. Liu, X. Gao, C. A. Schlosser, E. Clark, D. P. Lettenmaier, and K. Hilburn, 2015: The observed state of the energy budget in the early twenty-first century. *Journal of Climate*, **28**, 8319 – 8346, doi:10.1175/JCLI-D-14-00556.1.

L'Ecuyer, T. S., Y. Hang, A. V. Matus, and Z. Wang, 2019: Reassessing the effect of cloud type on earth's energy balance in the age of active spaceborne observations. part i: Top of atmosphere and surface. *Journal of Climate*, **32**, 6197 – 6217, doi:10.1175/JCLI-D-18-0753.1.

Mace, G. G., M. Deng, B. Soden, and E. Zipser, 2006: Association of tropical cirrus in the 10–15-km layer with deep convective sources: An observational study combining millimeter radar data and satellite-derived trajectories. *Journal of the Atmospheric Sciences*, **63**, 480 – 503, doi:10.1175/JAS3627.1.

Maddox, R., 1980: Mesoscale Convective Complexes. *Bull. Am. Meteorol. Soc.*, **61**, 1374–1387.

Manabe, S. and R. F. Strickler, 1964: Thermal Equilibrium of the Atmosphere with a Convective Adjustment. *Journal of the Atmospheric Sciences*, **21**, 361–385, doi:10.1175/1520-0469(1964)021<0361:teotaw>2.0.co;2.

Manabe, S. and R. T. Wetherald, 1967: Thermal Equilibrium of the Atmosphere with a Given Distribution of Relative Humidity. *Journal of the Atmospheric Sciences*, **24**, 241–259.

Mapes, B. E. and R. A. Houze, 1993: Cloud Clusters and Superclusters over the Oceanic Warm Pool. *Monthly Weather Review*, **121**, 1398, doi:10.1175/1520-0493(1993)121<1398:CCASOT>2.0.CO;2.

Marchand, R., G. G. Mace, T. Ackerman, and G. Stephens, 2008: Hydrometeor detection using cloudsat?an earth-orbiting 94-ghz cloud radar. *Journal of Atmospheric and Oceanic Technology*, **25**, 519 – 533, doi:10.1175/2007JTECHA1006.1.

Markus, T. and D. Cavalieri, 2000: An enhancement of the nasa team sea ice algorithm. *IEEE Transactions on Geoscience and Remote Sensing*, **38**, 1387–1398, doi:10.1109/36.843033.

Masunaga, H., T. S. L'ecuyer, and C. D. Kummerow, 2005: Variability in the Characteristics of Precipitation Systems in the Tropical Pacific. Part I: Spatial Structure. *Journal of Climate*, **18**, 823–840.

Masunaga, H. and Z. J. Luo, 2016: Convective and large-scale mass flux profiles over tropical oceans determined from synergistic analysis of a suite of satellite observations. *Journal of Geophysical Research: Atmospheres*, **121**, 7958–7974, doi:https://doi.org/10.1002/2016JD024753.

Matus, A. V. and T. S. L'Ecuyer, 2017: The role of cloud phase in earth's radiation budget. *Journal of Geophysical Research: Atmospheres*, **122**, 2559–2578, doi:https://doi.org/10.1002/2016JD025951.

Mauritsen, T. and B. Stevens, 2015: Missing iris effect as a possible cause of muted hydrological change and high climate sensitivity in models. *Nature Geoscience*, **8**, 346–351, doi:10.1038/ngeo2414.

Meneghini, R., H. Kim, L. Liao, J. Kwiatkowski, and T. Iguchi, 2021: Path Attenuation Estimates for the GPM Dual-frequency Precipitation Radar (DPR). *J. Meteorol. Soc. Japan. Ser. II*, **advpub**, doi:10.2151/jmsj.2021-010.

Miller, S. T. K., B. D. Keim, R. W. Talbot, and H. Mao, 2003: Sea breeze: Structure, forecasting, and impacts. *Reviews of Geophysics*, **41**, doi:https://doi.org/10.1029/2003RG000124.

Mitchell, J. F. B., 1987: Detection of climate change due to increases in CO_2 and trace gases. *Theoretical and Applied Climatology*, **38**, 234–234, doi:10.1007/BF00867416.

Nakazawa, T., 1988: Tropical super clusters within intraseasonal variations over the western pacific. *Journal of the Meteorological Society of Japan. Ser. II*, **66**, 823–839, doi:10.2151/jmsj1965.66.6_823.

Narsey, S., C. Jakob, M. S. Singh, M. Bergemann, V. Louf, A. Protat, and C. Williams, 2019: Convective Precipitation Efficiency Observed in the Tropics. *Geophys. Res. Lett.*, **46**, 13574–13583, doi:https://doi.org/10.1029/2019GL085031.

Needham, M. R. and D. A. Randall, 2021: Riehl and malkus revisited: The role of cloud radiative effects. *Journal of Geophysical Research: Atmospheres*, **126**, e2021JD035019, doi:https://doi.org/10.1029/2021JD035019.

Nesbitt, S. W. and E. J. Zipser, 2003: The diurnal cycle of rainfall and convective intensity according to three years of trmm measurements. *Journal of Climate*, **16**, 1456–1475, doi:10.1175/1520-0442(2003)016<1456:tdcora>2.0.co;2.

Nesbitt, S. W., E. J. Zipser, and D. J. Cecil, 2000: A Census of Precipitation Features in the Tropics Using TRMM: Radar, Ice Scattering, and Lightning Observations. *Journal of Climate*, **13**, 4087–4106, doi:10.1175/1520-0442(2000)013<4087:ACOPFI>2.0.CO;2.

Ockert-Bell, M. E. and D. L. Hartmann, 1992: The effect of cloud type on earth's energy balance: Results for selected regions. *Journal of Climate*, **5**, 1157–1171.

Oreopoulos, L. and W. B. Rossow, 2011: The cloud radiative effects of International Satellite Cloud Climatology Project weather states. *J. Geophys. Res. Atmos.*, **116**, doi:https://doi.org/10.1029/2010JD015472.

Park, S., S.-H. Jung, and G. Lee, 2015: Cross Validation of TRMM PR Reflectivity Profiles Using 3D Reflectivity Composite from the Ground-Based Radar Network over the Korean Peninsula. *J. Hydrometeorol.*, **16**, 668–687, doi:10.1175/JHM-D-14-0092.1.

Pereira, L. G. and S. A. Rutledge, 2006: Diurnal cycle of shallow and deep convection for a tropical land and an ocean environment and its relationship to synoptic wind regimes. *Mon. Weather Rev.*, **134**, 2688–2701, doi:10.1175/MWR3181.1.

Pierrehumbert, R. T., 1995: Thermostats, Radiator Fins, and the Local Runaway Greenhouse. *Journal of Atmospheric Sciences*, **52**, 1784–1806, doi:10.1175/1520-0469(1995)052<1784:TRFATL>2.0.CO;2.

Pilewskie, J. A. and T. S. L'Ecuyer, 2022: The global nature of early-afternoon and late-night convection through the eyes of the a-train. *Journal of Geophysical Research: Atmospheres*, **127**, e2022JD036438, doi:https://doi.org/10.1029/2022JD036438.

Protopapadaki, S. E., C. J. Stubenrauch, and A. G. Feofilov, 2017: Upper tropospheric cloud systems derived from IR sounders: Properties of cirrus anvils in the tropics. *Atmos. Chem. Phys.*, **17**, 3845–3859, doi:10.5194/acp-17-3845-2017.

Ramanathan, V., R. D. Cess, E. F. Harrison, P. Minnis, B. R. Barkstrom, E. Ahmad, and D. Hartmann, 1989: Cloud-Radiative Forcing and Climate: Results from the Earth Radiation Budget Experiment. *Science (80-.).*, **243**, 57–63, doi:10.1126/science.243.4887.57.

Ramanathan, V. and W. Collins, 1991: Thermodynamic regulation of ocean warming by cirrus clouds deduced from observations of the 1987 El Niño. *Nature*, **351**, 27–32.

Randall, D. A., Harshvardhan, D. A. Dazlich, and T. G. Corsetti, 1989: Interactions among Radiation, Convection, and Large-Scale Dynamics in a General Circulation Model. *Journal of Atmospheric Sciences*, **46**, 1943–1970, doi:10.1175/1520-0469(1989)046<1943:IARCAL>2.0.CO;2.

Rapp, A. D., C. Kummerow, W. Berg, and B. Griffith, 2005: An Evaluation of the Proposed Mechanism of the Adaptive Infrared Iris Hypothesis Using TRMM VIRS and PR Measurements. *J. Clim.*, **18**, 4185–4194.

Rasmussen, K. L., M. M. Chaplin, M. D. Zuluaga, and R. A. Houze, 2016: Contribution of extreme convective storms to rainfall in south america. *Journal of Hydrometeorology*, **17**, 353–367.

Reed, R. J. and E. E. Recker, 1971: Structure and properties of synoptic-scale wave disturbances in the equatorial western pacific. *Journal of Atmospheric Sciences*, **28**, 1117 – 1133, doi:https://doi.org/10.1175/1520-0469(1971)028<1117:SAPOSS>2.0.CO;2.

Retsch, M. H., C. Jakob, and M. Singh, 2020: Assessing Convective Organization in Tropical Radar Observations. *J. Geophys. Res. Atmos.*, **125**, e2019JD031801, doi:10.1029/2019JD031801.
URL https://doi.org/10.1029/2019JD031801

Rickenbach, T. M., 1999: Cloud-Top Evolution of Tropical Oceanic Squall Lines from Radar Reflectivity and Infrared Satellite Data. *Mon. Weather Rev.*, **127**, 2951–2976, doi:https://doi.org/10.1175/1520-0493(1999)127<2951:CTEOTO>2.0.CO;2.

Riehl, H. and J. S. Malkus, 1958: On the heat balance in the equatorial trough zone. *Geophysica*, **6**, 503–538.

Riehl, H. and J. Simpson, 1979: The heat balance of the equatorial trough zone, revisited. *Beitraege zur Physik der Atmosphaere*, **52**, 287–305.

Rossow, W. B. and Y.-C. Zhang, 1995: Calculation of surface and top of atmosphere radiative fluxes from physical quantities based on ISCCP data sets: 2. Validation and first results. *J. Geophys. Res. Atmos.*, **100**, 1167–1197, doi:https://doi.org/10.1029/94JD02746.

Saint-Lu, M., S. Bony, and J.-L. Dufresne, 2020: Observational Evidence for a Stability Iris Effect in the Tropics. *Geophys. Res. Lett.*, **47**, e2020GL089059, doi:https://doi.org/10.1029/2020GL089059.

Sassen, K., S. Y. Matrosov, and J. Campbell, 2007: CloudSat spaceborne 94 GHz radar bright bands in the melting layer: An attenuation-driven upside-down lidar analog. *Geophys. Res. Lett.*, **34**, L16818.

Sassen, K., Z. Wang, and D. Liu, 2008: Global distribution of cirrus clouds from CloudSat/Cloud-Aerosol Lidar and Infrared Pathfinder Satellite Observations (CALIPSO) measurements. *J. Geophys. Res. Atmos.*, **113**, doi:https://doi.org/10.1029/2008JD009972.

Sauter, K., T. S. L'Ecuyer, S. C. van den Heever, C. Twohy, A. Heidinger, S. Wanzong, and N. Wood, 2019: The observed influence of tropical convection on the saharan dust layer. *Journal of Geophysical Research: Atmospheres*, **124**, 10896–10912, doi:https://doi.org/10.1029/2019JD031365.

Schumacher, C. and J. Houze, Robert A., 2003: Stratiform Rain in the Tropics as Seen by the TRMM Precipitation Radar. *Journal of Climate*, **16**, 1739–1756, doi:10.1175/1520-0442(2003)016<1739:SRITTA>2.0.CO;2.

Sherwood, S. C., S. Bony, and J.-L. Dufresne, 2014: Spread in model climate sensitivity traced to atmospheric convective mixing. *Nature*, **505**, 37.

Sherwood, S. C., M. J. Webb, J. D. Annan, K. C. Armour, P. M. Forster, J. C. Hargreaves, G. Hegerl, S. A. Klein, K. D. Marvel, E. J. Rohling, M. Watanabe, T. Andrews, P. Braconnot, C. S. Bretherton, G. L. Foster, Z. Hausfather, A. S. von der Heydt, R. Knutti, T. Mauritsen, J. R. Norris, C. Proistosescu, M. Rugenstein, G. A. Schmidt, K. B. Tokarska, and M. D. Zelinka, 2020: An Assessment of Earth's Climate Sensitivity Using Multiple Lines of Evidence. *Reviews of Geophysics*, **58**, doi:10.1029/2019RG000678.

Shige, S., Y. Nakano, and M. K. Yamamoto, 2017: Role of orography, diurnal cycle, and intraseasonal oscillation in summer monsoon rainfall over the western ghats and myanmar coast. *J. Clim.*, **30**, 9365–9381, doi:10.1175/JCLI-D-16-0858.1.

Simpson, J., R. F. Adler, and G. R. North, 1988: A proposed tropical rainfall measuring mission (trmm) satellite. *Bulletin of the American Meteorological Society*, **69**, 278 – 295, doi:10.1175/1520-0477(1988)069<0278:APTRMM>2.0.CO;2.

Singh, M. S. and P. A. O'Gorman, 2015: Increases in moist-convective updraught velocities with warming in radiative-convective equilibrium. *Q. J. R. Meteorol. Soc.*, **141**, 2828–2838, doi:https://doi.org/10.1002/qj.2567.

Slingo, A. and J. M. Slingo, 1988: The response of a general circulation model to cloud longwave radiative forcing. I: Introduction and initial experiments. *Quarterly Journal of the Royal Meteorological Society*, **114**, 1027–1062, doi:10.1002/qj.49711448209.

— 1991: Response of the National Center for Atmospheric Research community climate model to improvements in the representation of clouds. *Journal of Geophysical Research*, **96**, 15,341–15,357, doi:10.1029/91JD00930.

Solomon, D. L., K. P. Bowman, and C. R. Homeyer, 2016: Tropopause-Penetrating Convection from Three-Dimensional Gridded NEXRAD Data. *J. Appl. Meteorol. Climatol.*, **55**, 465–478, doi:10.1175/JAMC-D-15-0190.1.

Steiner, M., R. A. Houze, and S. E. Yuter, 1995: Climatological characterization of three-dimensional storm structure from operational radar and rain gauge data. *Journal of Applied Meteorology and Climatology*, **34**, 1978 – 2007, doi:10.1175/1520-0450(1995)034<1978:CCOTDS>2.0.CO;2.

Stephens, G. L., 2005: Cloud Feedbacks in the Climate System: A Critical Review. *Journal of Climate*, **18**, 237–273.

Stephens, G. L. and T. D. Ellis, 2008: Controls of global-mean precipitation increases in global warming GCM experiments. *J. Clim.*, **21**, 6141–6155, doi:10.1175/2008JCLI2144.1.

Stephens, G. L. and T. J. Greenwald, 1991: The Earth's radiation budget and its relation to atmospheric hydrology: 2. Observations of cloud effects. *J. Geophys. Res. Atmos.*, **96**, 15325–15340, doi:https://doi.org/10.1029/91JD00972.

Stephens, G. L., M. Hakuba, H. Takahashi, J. Pilewskie, T. Andrews, K. Shiro, C. Stubenrauch, and L. Wu, submitted: Deep convection, cloud feedbacks and climate sensitivity. *Survey of Geophysics*.

Stephens, G. L., A. Slingo, M. J. Webb, P. J. Minnett, P. H. Daum, L. Kleinman, I. Wittmeyer, and D. A. Randall, 1994: Observations of the earth's radiation budget in relation to atmospheric hydrology: 4. atmospheric column radiative cooling over the world's oceans. *Journal of Geophysical Research: Atmospheres*, **99**, 18585–18604, doi:https://doi.org/10.1029/94JD01151.

Stephens, G. L., D. G. Vane, R. J. Boain, G. G. Mace, K. Sassen, Z. Wang, A. J. Illingworth, E. J. O'connor, W. B. Rossow, S. L. Durden, S. D. Miller, R. T. Austin, A. Benedetti, and C. Mitrescu, 2002: The cloudsat mission and the a-train: A new dimension of space-based observations of clouds and precipitation. *Bulletin of the American Meteorological Society*, **83**, 1771 – 1790, doi:10.1175/BAMS-83-12-1771.

Stephens, G. L., D. G. Vane, S. Tanelli, E. Im, S. Durden, M. Rokey, D. Reinke, P. Partain, G. G. Mace, R. Austin, T. L'Ecuyer, J. Haynes, M. Lebsock, K. Suzuki, D. Waliser,

D. Wu, J. Kay, A. Gettelman, Z. Wang, and R. Marchand, 2008: Cloudsat mission: Performance and early science after the first year of operation. *Journal of Geophysical Research: Atmospheres*, **113**, doi:https://doi.org/10.1029/2008JD009982.

Stephens, G. L. and P. J. Webster, 1981: Clouds and climate: sensitivity of simple systems. *J. Atmos. Sci.*, **38**, 235–247, doi:10.1175/1520-0469(1981)038<0235:CACSOS>2.0.CO;2.

Stephens, G. L., P. J. Webster, R. H. Johnson, R. Engelen, and T. L'Ecuyer, 2004: Observational evidence for the mutual regulation of the tropical hydrological cycle and tropical sea surface temperatures. *Journal of Climate*, **17**, 2213 – 2224, doi:10.1175/1520-0442(2004)017<2213:OEFTMR>2.0.CO;2.

Stephens, G. L. and K. J. Wilson, 1980: The response of a deep cumulus convection model to changes in radiative heating. *Journal of Atmospheric Sciences*, **37**, 421 – 434, doi:https://doi.org/10.1175/1520-0469(1980)037<0421:TROADC>2.0.CO;2.

Stephens, G. L. and N. B. Wood, 2007: Properties of tropical convection observed by millimeter-wave radar systems. *Monthly Weather Review*, **135**, 821–842, doi:10.1175/MWR3321.1.

Storer, R. L., S. C. Van Den Heever, and T. S. L'Ecuyer, 2014: Observations of aerosol-induced convective invigoration in the tropical east Atlantic. *J. Geophys. Res.*, **119**, 3963–3975, doi:10.1002/2013JD020272.

Stubenrauch, C. J., G. Mandorli, and E. Lemaitre, 2023: Convective organization and 3D structure of tropical cloud systems deduced from synergistic A-Train observations and machine learning. *Atmos. Chem. Phys.*, **23**, 5867–5884, doi:10.5194/acp-23-5867-2023.

Su, H., J. H. Jiang, J. D. Neelin, T. J. Shen, C. Zhai, Q. Yue, Z. Wang, L. Huang, Y. S. Choi, G. L. Stephens, and Y. L. Yung, 2017: Tightening of tropical ascent and high clouds key to precipitation change in a warmer climate. *Nat. Commun.*, **8**, 1–9, doi:10.1038/ncomms15771.

Takahashi, H. and Z. Luo, 2012: Where is the level of neutral buoyancy for deep convection? *Geophys. Res. Lett.*, **39**, doi:https://doi.org/10.1029/2012GL052638.

Takahashi, H. and Z. J. Luo, 2014: Characterizing tropical overshooting deep convection from joint analysis of CloudSat and geostationary satellite observations. *Journal of Geophysical Research: Atmospheres*, **119**, 112–121, doi:10.1002/2013JD020972.

Takahashi, H., Z. J. Luo, and G. Stephens, 2021: Revisiting the Entrainment Relationship of Convective Plumes: A Perspective From Global Observations. *Geophys. Res. Lett.*, **48**, e2020GL092349, doi:https://doi.org/10.1029/2020GL092349.

Takahashi, H., Z. J. Luo, G. Stephens, and J. P. Mulholland, 2023: Revisiting the Land-Ocean Contrasts in Deep Convective Cloud Intensity Using Global Satellite Observations. *Geophys. Res. Lett.*, **50**, e2022GL102089, doi:https://doi.org/10.1029/2022GL102089.

Takahashi, H., Z. J. Luo, and G. L. Stephens, 2017: Level of neutral buoyancy, deep convective outflow, and convective core: New perspectives based on 5years of CloudSat data. *Journal of Geophysical Research*, **122**, 2958–2969, doi:10.1002/2016JD025969.

Tanelli, S., S. L. Durden, E. Im, K. S. Pak, D. G. Reinke, P. Partain, J. M. Haynes, and R. T. Marchand, 2008: Cloudsat's cloud profiling radar after two years in orbit: Performance, calibration, and processing. *IEEE Transactions on Geoscience and Remote Sensing*, **46**, 3560–3573, doi:10.1109/TGRS.2008.2002030.

Tegtmeier, S., J. Anstey, S. Davis, R. Dragani, Y. Harada, I. Ivanciu, R. Pilch Kedzierski, K. Krüger, B. Legras, C. Long, J. S. Wang, K. Wargan, and J. S. Wright, 2020: Temperature and tropopause characteristics from reanalyses data in the tropical tropopause layer. *Atmospheric Chemistry and Physics*, **20**, 753–770, doi:10.5194/acp-20-753-2020.

Tobin, I., S. Bony, C. E. Holloway, and J.-y. Grandpeix, 2013: Does convective aggregation need to be represented in cumulus parameterizations? *Journal of Advances in Modeling Earth Systems*, **5**, 692–703, doi:10.1002/jame.20047.

Tobin, I., S. Bony, and R. Roca, 2012: Observational evidence for relationships between the degree of aggregation of deep convection, water vapor, surface fluxes, and radiation. *Journal of Climate*, **25**, 6885–6904, doi:10.1175/JCLI-D-11-00258.1.

Toller, G., X. J. Xiong, J. Sun, B. N. Wenny, X. Geng, J. Kuyper, A. Angal, H. Chen, S. Madhavan, and A. Wu, 2013: Terra and Aqua moderate-resolution imaging spectroradiometer collection 6 level 1B algorithm. *Journal of Applied Remote Sensing*, **7**, 073557, doi:10.1117/1.JRS.7.073557.

Tompkins, A. M. and A. G. Semie, 2017: Organization of tropical convection in low vertical wind shears: Role of updraft entrainment. *J. Adv. Model. Earth Syst.*, **9**, 1046–1068, doi:10.1002/2016MS000802.

Trenberth, K. E., J. T. Fasullo, and J. Kiehl, 2009: Earth's global energy budget. *Bulletin of the American Meteorological Society*, **90**, 311 – 324, doi:10.1175/2008BAMS2634.1.

van Bemmelen, W., 1922: Land-und seebrise in batavia. *Beitr. Phys. frei. Atmos.*, **10**, 169–177.

van der Walt, S., J. L. Schönberger, J. Nunez-Iglesias, F. Boulogne, J. D. Warner, N. Yager, E. Gouillart, T. Yu, and T. scikit-image contributors, 2014: scikit-image: image processing in Python. *PeerJ*, **2**, e453, doi:10.7717/peerj.453.

Wang, D., S. E. Giangrande, Z. Feng, J. C. Hardin, and A. F. Prein, 2020: Updraft and Downdraft Core Size and Intensity as Revealed by Radar Wind Profilers: MCS Observations and Idealized Model Comparisons. *J. Geophys. Res. Atmos.*, **125**, e2019JD031774, doi:https://doi.org/10.1029/2019JD031774.

Wielicki, B. A., T. Wong, R. P. Allan, A. Slingo, J. T. Kiehl, B. J. Soden, C. T. Gordon, A. J. Miller, S.-K. Yang, D. A. Randall, F. Robertson, J. Susskind, and H. Jacobowitz, 2002: Evidence for Large Decadal Variability in the Tropical Mean Radiative Energy Budget. *Science*, **295**, 841–844, doi:10.1126/science.1065837.

Williams, E. and S. Stanfill, 2002: The physical origin of the land–ocean contrast in lightning activity. *Comptes Rendus Phys.*, **3**, 1277–1292, doi:https://doi.org/10.1016/S1631-0705(02)01407-X.

Williams, M. and R. A. Houze, 1987: Satellite-observed characteristics of winter monsoon cloud clusters. *Monthly Weather Review*, **115**, 505 – 519, doi:10.1175/1520-0493(1987)115<0505:SOCOWM>2.0.CO;2.

Wing, A. A. and T. W. Cronin, 2016: Self-aggregation of convection in long channel geometry. *Quarterly Journal of the Royal Meteorological Society*, **142**, 1–15, doi:10.1002/qj.2628.

Wing, A. A. and K. A. Emanuel, 2014: Journal of advances in modeling earth systems convection in idealized numerical modeling simulations. *Journal of Advances in Modeling Earth Systems*, **6**, 59–74, doi:10.1002/2013MS000269.

Wodzicki, K. R. and A. D. Rapp, 2022: More Intense, Organized Deep Convection With Shrinking Tropical Ascent Regions. *Geophys. Res. Lett.*, **49**, e2022GL098615, doi:https://doi.org/10.1029/2022GL098615.

Wong, T., B. A. Wielicki, R. B. Lee, G. L. Smith, K. A. Bush, and J. K. Willis, 2006: Reexamination of the Observed Decadal Variability of the Earth Radiation Budget Using Altitude-Corrected ERBE/ERBS Nonscanner WFOV Data. *J. Clim.*, **19**, 4028–4040, doi:https://doi.org/10.1175/JCLI3838.1.

Xu, K.-M., Y. Hu, and T. Wong, 2019: Convective Aggregation and Indices Examined from CERES Cloud Object Data. *J. Geophys. Res. Atmos.*, **124**, 13604–13624, doi:10.1029/2019JD030816.

Xu, K.-M., T. Wong, S. Dong, F. Chen, S. Kato, and P. C. Taylor, 2016: Cloud Object Analysis of CERES Aqua Observations of Tropical and Subtropical Cloud Regimes: Four-Year Climatology. *J. Clim.*, **29**, 1617–1638, doi:10.1175/JCLI-D-14-00836.1.

Xu, K.-M., T. Wong, B. Wielicki, L. Parker, and Z. Eitzen, 2005: Statistical Analyses of Satellite Cloud Object Data from CERES. Part I: Methodology and Preliminary Results of the 1998 El Niño/2000 La Niña. *J. Clim. - J Clim.*, **18**, 2497–2514, doi:10.1175/JCLI3418.1.

Xu, W. and E. J. Zipser, 2011: Diurnal variations of precipitation, deep convection, and lightning over and east of the eastern tibetan plateau. *Journal of Climate*, **24**, 448 – 465, doi:10.1175/2010JCLI3719.1.

Yanai, M., S. K. Esbensen, and J.-H. Chu, 1973: Determination of bulk properties of tropical cloud clusters from large-scale heat and moisture budgets. *Journal of the Atmospheric Sciences*, **30**, 611–627.

Yang, G.-Y. and J. Slingo, 2001: The diurnal cycle in the tropics. *Monthly Weather Review*, **129**, 784 – 801, doi:https://doi.org/10.1175/1520-0493(2001)129<0784:TDCITT>2.0.CO;2.

Yang, J., Z. Wang, A. J. Heymsfield, and J. R. French, 2016: Characteristics of vertical air motion in isolated convective clouds. *Atmos. Chem. Phys.*, **16**, 10159–10173, doi:10.5194/acp-16-10159-2016.

Yuan, J. and R. A. Houze, 2010: Global variability of mesoscale convective system anvil structure from A-train satellite data. *J. Clim.*, **23**, 5864–5888, doi:10.1175/2010JCLI3671.1.

— 2013: Deep convective systems observed by a-train in the tropical indo-pacific region affected by the MJO. *J. Atmos. Sci.*, **70**, 465–486, doi:10.1175/JAS-D-12-057.1.

Yuan, J., R. A. Houze, and A. J. Heymsfield, 2011: Vertical Structures of Anvil Clouds of Tropical Mesoscale Convective Systems Observed by CloudSat. *Journal Of The Atmospheric Sciences*, **68**, 1653–1674, doi:10.1175/2011JAS3687.1.

Zelinka, M. D. and D. L. Hartmann, 2009: Response of humidity and clouds to tropical deep convection. *Journal of Climate*, **22**, 2389–2404, doi:10.1175/2008JCLI2452.1.

— 2010: Why is longwave cloud feedback positive? *J. Geophys. Res. Atmos.*, **115**, doi:https://doi.org/10.1029/2010JD013817.

Zhang, A. and Y. Fu, 2018: Life Cycle Effects on the Vertical Structure of Precipitation in East China Measured by Himawari-8 and GPM DPR. *Mon. Weather Rev.*, **146**, 2183–2199, doi:10.1175/MWR-D-18-0085.1.

Zhang, Y. C., W. B. Rossow, and A. A. Lacis, 1995: Calculation of surface and top of atmosphere radiative fluxes from physical quantities based on isccp data sets. 1:

Method and sensitivity to input data uncertainties. *Journal of Geophysical Research*, **100**, doi:10.1029/94JD02747.

Zheng, J., D. Liu, Z. Wang, and Y. Wang, 2018: Differences among three types of tropical deep convective clusters observed from A-Train satellites. *J. Quant. Spectrosc. Radiat. Transf.*, **217**, 253–261, doi:10.1016/j.jqsrt.2018.05.006.

Zipser, E. J., 1969: The role of organized unsaturated convective downdrafts in the structure and rapid decay of an equatorial disturbance. *Journal of Applied Meteorology and Climatology*, **8**, 799 – 814, doi:https://doi.org/10.1175/1520-0450(1969)008<0799:TROOUC>2.0.CO;2.

— 2003: *Some Views On "Hot Towers" after 50 Years of Tropical Field Programs and Two Years of TRMM Data*, American Meteorological Society, Boston, MA. 49–58.

Zipser, E. J., D. J. Cecil, C. Liu, S. W. Nesbitt, and D. P. Yorty, 2006: Where are the most: Intense thunderstorms on Earth? *Bulletin of the American Meteorological Society*, **87**, 1057–1071, doi:10.1175/BAMS-87-8-1057.

Zipser, E. J. and M. A. LeMone, 1980: Cumulonimbus vertical velocity events in gate. part ii: Synthesis and model core structure. *Journal of Atmospheric Sciences*, **37**, 2458 – 2469, doi:https://doi.org/10.1175/1520-0469(1980)037<2458:CVVEIG>2.0.CO;2.